CB NOTE 320 January 16, 1998

$\omega \rightarrow \eta\gamma$ Analysis, part II

Technical Report Mark Lakata

Abstract

We report on an analysis of the branching ratio of the rare $\eta(\omega \to \eta\gamma)$ radiative decay, observed in $p\overline{p} \to \eta\omega$ annihilations, and determine it to be $(2.1 \pm 1.3) \times 10^{-4}$.

Chapter 1

One Page Summary

The analysis of BR($\omega \to \eta\gamma$) has been significantly improved in kinematic fitting and histogram fitting over the previous analysis done at Berkeley, and stands in disagreement with the Zurich analysis. 20 million all-neutral events were scanned for 5 gamma events and 4-momentum conservation. They were submitted to a kinematic fit for three hypotheses, $\eta\eta\gamma$, $\pi^0\eta\gamma$ and $\pi^0\pi^0\gamma$. Only unambiguous events with CL>10% were kept. Each hypothesis group was binned into a Dalitz plot and fitted against the sum of theoretical distributions for the signal channel and the background channels. The theoretical distributions were derived from weighted Monte Carlo simulations. The signal channels were $\eta(\omega \to \eta\gamma)$, $\eta(\omega \to \pi^0\gamma)$, and $\pi^0(\omega \to \pi^0\gamma)$, for the three groups respectively. The main background channel for $\eta\eta\gamma$ is $\pi^0\eta\eta$, for $\pi^0\eta\gamma$ is $\pi^0\pi^0\eta$ and for $\pi^0\pi^0\gamma$ is $\pi^0\pi^0\pi^0$, where one soft photon (from a π^0) is lost. Other minor backgrounds were included also (see text). We also allow for the existence of 3 undiscovered channels, $p\overline{p} \to \eta\eta\gamma$, $\pi^0\eta\gamma$ and $\pi^0\pi^0\gamma$, which do not proceed through a resonant intermediate state.

The latter two signals, $\eta(\omega \to \pi^0\gamma)$ and $\pi^0(\omega \to \pi^0\gamma)$, were used as reference measurements to the rare signal $\eta(\omega \to \eta\gamma)$. The results for the reference signals agreed perfectly with expectations derived from tabulated branching ratios and the trigger efficiency. We then derived the branching ratio for the rare signal to be

$$BR(\omega \to \eta\gamma) = (2.1 \pm 1.3) \times 10^{-4}$$

We find that this measurement disagrees with the previous Crystal Barrel measurement [27] of BR($\omega \to \eta\gamma$) $= (6.6 \pm 1.7) \times 10^{-4}$. In a separate paper [32], we attempt to redo the previous analysis. The reason for the great difference is that the previous analysis did not take into account the possibility of the $\eta\eta\gamma$ background. By including the $\eta\eta\gamma$ in the method of the previous measurement, the result is reduced to 2.8×10^{-4}, in agreement with this current value of 2.1×10^{-4}.

It is our intention to supersede the result of the previous paper with the new result, on the grounds that it (1) has higher statistics, (2) does not rely on any pre-measured branching ratios for backgrounds, and (3) is self-consistent with a reanalysis using the previous method.

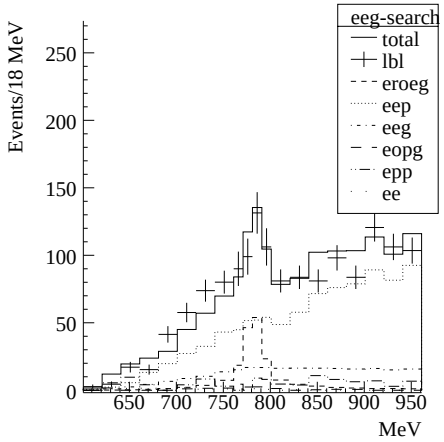

Chapter 2

Introduction

This technical report forms part of the thesis of Mark Lakata, and contains more information than probably necessary.

The radiative decays of mesons are a useful source in testing various theories of low energy physics, i.e. the quark model and the vector dominance model. For example, in both models, decays from and to nonet central states (i.e. η, η', ω, ϕ) are dependent on the pseudoscalar and vector mixing angles. For a review of radiative meson decays see [1]. All of the relevant low mass radiative meson decays have been observed, yet measurements of

$$\omega \rightarrow \eta\gamma \tag{2.1}$$

have been by far the poorest. In the neutral decay mode of the ω, the branching ratio of $\omega \rightarrow \eta\gamma$ is nearly three orders of magnitude less than $\omega \rightarrow \pi^0\gamma$. This large factor is due nearly equally to both phase space and matrix element factors.

The all-neutral sources of ω production in $p\overline{p}$ annihilations are given in table 2.1. In this paper, the branching ratio of the decay of reaction 2.1 was measured using ω mesons from the two-body reaction

$$p\overline{p} \rightarrow \eta\omega \tag{2.2}$$

measured with the Crystal Barrel spectrometer[2] (PS197) at CERN. This proton-antiproton annihilation channel was the choice for analysis because, as a source for ω's, it has one of the highest branching ratios, has low combinatorics and is all neutral. The Crystal Barrel is especially suited for high precision gamma measurements. The channel $\eta\omega$ was chosen over $\pi^0\omega$ for two reasons. First, the former channel contains no π^0's at all, π^0's being produced by the potential feed-through reaction $\omega \rightarrow \pi^0\gamma$. Second, the potential ρ^0 backgrounds are a relative factor 9 times less in $\eta\omega/\eta\rho^0$ than in $\pi^0\omega/\pi^0\rho^0$.

The $p\overline{p} \rightarrow \pi^+\pi^-\omega$ annihilation channel was not used, even though it has a high branching ratio, because of additional spurious EM showers created by charged particles. Because this analysis is looking for a rare decay into a single photon, the background from these so-called hadronic "split-offs" was unacceptable.

Channel	BR	Ref	Comment
$p\overline{p} \rightarrow \gamma\omega$	$(6.8 \pm 1.9) \times 10^{-5}$	[4]	Too small
$p\overline{p} \rightarrow \pi^0\omega$	$(5.73 \pm 0.47) \times 10^{-3}$	[8]	Large $\pi^0\pi^0\eta$ background
$p\overline{p} \rightarrow \eta\omega$	$(1.51 \pm 0.12) \times 10^{-2}$	[8]	*Desired channel*
$p\overline{p} \rightarrow \omega\omega$	$(3.32 \pm 0.34) \times 10^{-2}$	[8]	Extra ω decay lowers efficiency
$p\overline{p} \rightarrow \eta'\omega$	$(7.8 \pm 0.8) \times 10^{-3}$	[8]	η' hard to tag
$d\overline{p} \rightarrow \omega$ n	$(2.28 \pm 0.41) \times 10^{-5}$	[9]	Too small
$p\overline{p} \rightarrow \pi^0\pi^0\omega$	$(2.57 \pm 0.17) \times 10^{-2}$	[26]	Many combinatorics
$p\overline{p} \rightarrow \pi^0\eta\omega$	$(6.8 \pm 0.5) \times 10^{-3}$	[10]	Many combinatorics
$p\overline{p} \rightarrow \rho^0\eta$	$(3.9 \pm 0.3) \times 10^{-3}$	[24]*	ρ^0 background.
$p\overline{p} \rightarrow \rho^0\pi^0$	$(1.7 \pm 0.1) \times 10^{-2}$	[12]*	ρ^0 background.
$p\overline{p} \rightarrow \pi^+\pi^-\omega$	$(6.6 \pm 0.6) \times 10^{-2}$	[11]	Charged split-offs

Table 2.1: Branching ratios of channels containing ω's or ρ^0's. * Indicates averages of many measurements.

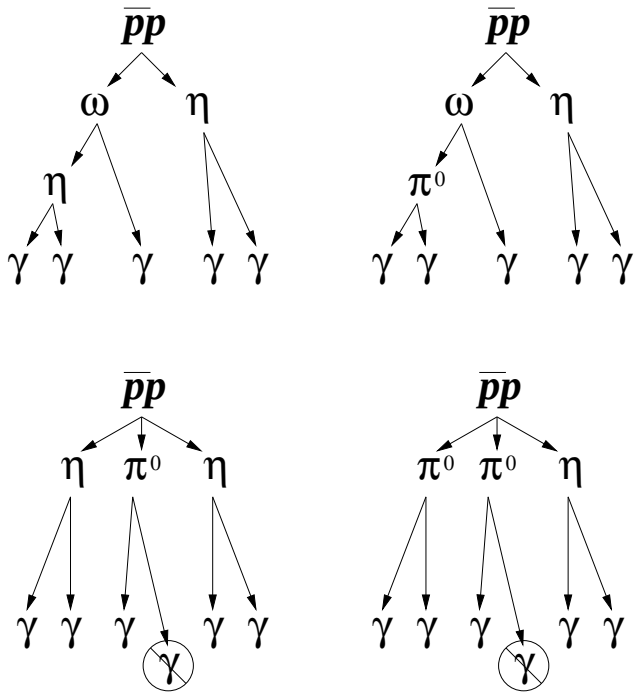

Figure 2.1: Decay chain of four most important channels, the two signal channels $\eta(\omega\to\eta\gamma)$ (above left) and $\eta(\omega\to\pi^0\gamma)$ (above right), and the two background channels $\pi^0\eta\eta$ (below left) and $\pi^0\pi^0\eta$ (below right)

The ratio of rates of $\omega\to\eta\gamma$ to $\omega\to\pi^0\gamma$ was measured to cancel many common systematics, such as the overall $p\overline{p}$ annihilation rate.

In the analysis, the gammas were combined pairwise to search for η's and π^0's. Once the π^0's and η's were identified, they were combined with the remaining unpaired gamma to form ω candidates. Figure 2.1 shows the decay chain graphically for the signals and the backgrounds.

Because the $\omega\to\eta\gamma$ is very rare, it is nearly lost to background. Thus great effort was taken to minimize this background as much as possible, while not totally killing the signal.

2.1 Report Outline

1. We provide a beginners introduction to the theory of radiative meson decays,
2. We continue with a description of the Crystal Barrel detector, collection of the data and the software reconstruction algorithms (chapter 4).
3. We then describe the Monte Carlo calculations done to simulate the important physics channels and their special properties (chapter 5).
4. We continue with the two data reduction passes on the data (chapters 6 and 7).
5. Finally, we summarize the last cuts (chapter 8) and the fits to the data versus the Monte Carlo simulations (chapter 9).
6. The Appendix contains information on algorithms for kinematic fitting and the fitting of real data to a linear sum of MC data, as well as a calculation of angular distributions and a summary of the 0-prong DLTs.

Chapter 3

Theory

3.1 Introduction

Rates of radiative decays of mesons are a useful observable for testing low energy models of non-perturbative QCD. The particular family of decays between low mass vector and pseudoscalar mesons is given in table 3.1.

To first order in the fine structure constant ($\alpha \equiv 1/137$), the general decay rate is written as

$$\Gamma(V \to P\gamma) = \frac{4}{3}\alpha k^3 |g_{VP\gamma}|^2$$

where k is the momentum of the radiated γ and

$$g_{VP\gamma} = g(\theta_P, \theta_V, \text{model}) \text{ MeV}^{-1}$$

is the theory dependent matrix element. The convention for SU(3) octet/singlet mixing between $I = 0$ states is as follows.

$$\begin{pmatrix} \eta \\ \eta' \end{pmatrix} = \begin{pmatrix} \cos\theta_P & -\sin\theta_P \\ \sin\theta_P & \sin\theta_P \end{pmatrix} \begin{pmatrix} \eta_8 \\ \eta_1 \end{pmatrix}$$
$$\begin{pmatrix} \phi \\ \omega \end{pmatrix} = \begin{pmatrix} \cos\theta_V & -\sin\theta_V \\ \sin\theta_V & \sin\theta_V \end{pmatrix} \begin{pmatrix} \omega_8 \\ \omega_1 \end{pmatrix} \approx \begin{pmatrix} s\bar{s} \\ u\bar{u} + d\bar{d} \end{pmatrix}$$

The deviation from ideal mixing is by convention defined as $\alpha \equiv \theta - \arctan(1/\sqrt{2})$. Mixing in the vector nonet is nearly ideal, that is the value of α for the vector nonet $\alpha \approx -0.3°$. Mixing in the pseudoscalar nonet is not ideal, with $\theta_P \approx -20°$.

3.2 Vector Meson Dominance

The theory of vector meson dominance (VMD) states that electro-magnetic reactions between hadronic states proceed through vector meson intermediate states, (i.e. $\rho \to \gamma$). Because the photon is not an isospin eigenstate, the three vector mesons (ρ^0, ω and ϕ) can contribute.

Decay	Γ [KeV]	Decay	Γ [KeV]
$\eta' \to \rho^0 \gamma$	60.7± 4%	$\eta' \to \omega\gamma$	6.07±10%
$K^{*\pm} \to K^{\pm}\gamma$	50.3± 9%	$K^{*0} \to K^0\gamma$	116.± 9%
$\phi \to \pi^0\gamma$	5.80±10%	$\phi \to \eta\gamma$	56.7± 5%
$\omega \to \pi^0\gamma$	717.± 6%	$\omega \to \eta\gamma$	7.0 ±25%
$\rho^{\pm} \to \pi^{\pm}\gamma$	68. ±22%	$\rho^0 \to \pi^0\gamma$	119.±25%
$\rho^0 \to \eta\gamma$	57.5±28%		±

Table 3.1: The eleven radiative meson decays and their rates. (See reference [14])

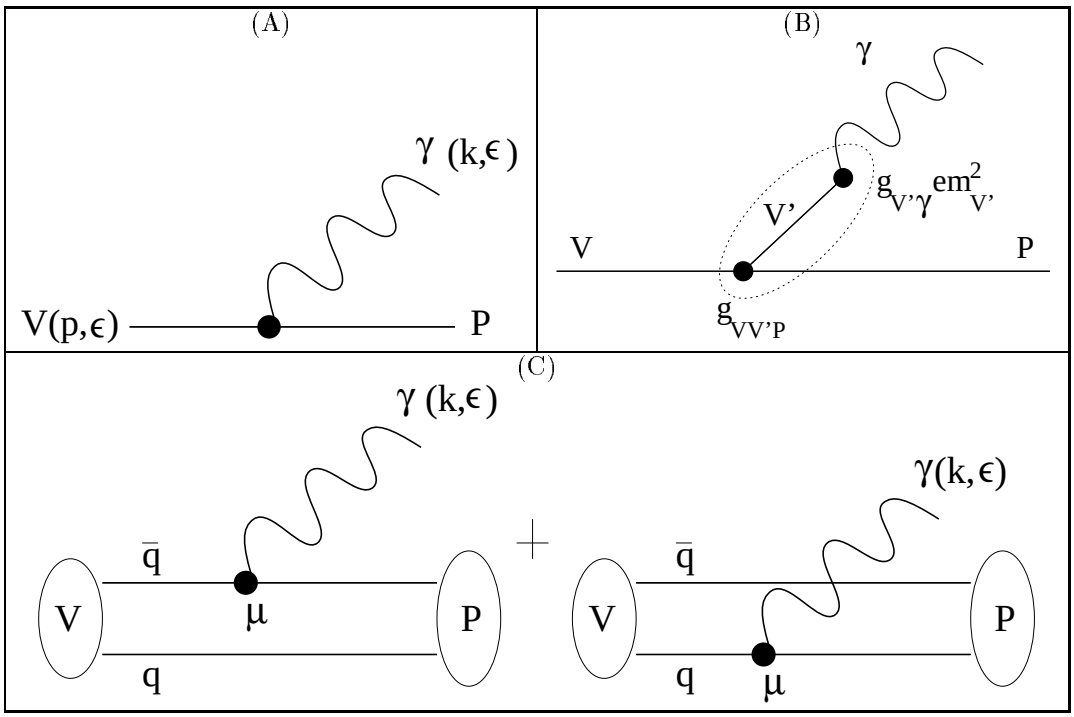

Figure 3.1: Decay mechanisms. (A) α process (B) Vector Meson Dominance (C) Quark model

$V \triangleright V' \otimes P$	coupling
$\mathbf{8} \triangleright \mathbf{8} \otimes \mathbf{8}$	$g_{V_i V'_j P_k} \sim g_{88} d_{ijk}$ (SU(3) structure)
$\mathbf{8} \triangleright \mathbf{8} \otimes \mathbf{1}$	$g_{V_i V'_j P} \sim g_{81} \delta_{ij}$
$\mathbf{8} \triangleright \mathbf{1} \otimes \mathbf{8}$	$g_{V_i V' P_j} \sim g_{81} \delta_{ij}$
$\mathbf{1} \triangleright \mathbf{8} \otimes \mathbf{8}$	$g_{V V'_i P_k} \sim g_{18} \delta_{ij}$
$\mathbf{1} \triangleright \mathbf{1} \otimes \mathbf{1}$	$g_{VV'P} \sim g_{11}$ ($= 0$ if $\gamma \neq \mathbf{1}$)

Table 3.2: The strong coupling constants are written in octet and singlet terms

$$g_{VP\gamma} = \sum_{V'} \left(em^2_{V'} g_{V'\gamma}\right) \left(g_{VV'P}\right)$$

Thus decay is reduced to a SU(3) interaction followed by transmutation of the intermediate vector into a photon. Assuming that the strong force symmetry is only broken between octet and singlet states and also that the photon is not a SU(3) singlet state, the unique coupling constants are at most three in number, as shown in table 3.2.

We can then write the measured coupling constants in terms of these octet/singlet constants and the nonet mixing angles,

$$\begin{aligned} g_{\omega\pi^0\gamma} &= \frac{\sqrt{2}}{3} \sin\alpha_V (g_{88} - g_{18}) + \\ &\quad \frac{1}{3} \cos\alpha_V (g_{88} + 2g_{18}) \\ g_{\omega\eta\gamma} &= \frac{1}{9} \cos\alpha_V \sin\alpha_P (g_{88} - 2g_{81} - 2g_{18}) + \\ &\quad \frac{2}{9} \sin\alpha_V \cos\alpha_P (-g_{88} - g_{81} - g_{18}) + \end{aligned}$$

$$\frac{\sqrt{2}}{9}\sin\alpha_V \sin\alpha_P(g_{88} - 2g_{81} + g_{18}) +$$
$$\frac{\sqrt{2}}{9}\cos\alpha_V \cos\alpha_P(-g_{88} - g_{81} + 2g_{18}).$$

In a recent paper [16], 11 measured radiative decays are fitted to these constraints. The authors find that full nonet symmetry holds to an extent by noting that the fitted g values are nearly all equal.

coupling g_{VP}	All free GeV^{-1}	Two free ($g_{88} = g_{18}$) GeV^{-1}
g_{88}	0.74 ± 0.02	0.70 ± 0.02
g_{18}	0.67 ± 0.02	0.70 ± 0.02
g_{81}	0.64 ± 0.06	0.61 ± 0.03

3.3 Static quark model

In the static quark model, the interaction that leads to decay is a simple M1 magnetic dipole interaction with matrix element,

$$(H = \vec{\mu} \cdot \vec{B})$$
$$M = \mu_q \vec{\sigma}_q \cdot (\vec{k} \times \vec{\epsilon})$$

For example, here is a sketch of the calculation of the g constants for $\omega \rightarrow \pi^0\gamma$.

$$g_{\omega\pi^0\gamma} = \langle\omega|\hat{\mu}\hat{\vec{\sigma}} \cdot \vec{\epsilon}|\pi^0\gamma\rangle \tag{3.1}$$
$$\hat{\vec{\sigma}} \cdot \vec{\epsilon}|\gamma\rangle = \hat{\sigma}_+|\gamma\rangle \tag{3.2}$$
$$|\omega\rangle = |\left(\cos\alpha_V \frac{(u\bar{u} + d\bar{d})}{\sqrt{2}} - \sin\alpha_V(s\bar{s})\right)(\uparrow\uparrow)\rangle \tag{3.3}$$
$$|\pi^0\rangle = |\left(\frac{(u\bar{u} - d\bar{d})}{\sqrt{2}}\right)\left(\frac{(\uparrow\downarrow - \downarrow\uparrow)}{\sqrt{2}}\right)\rangle \tag{3.4}$$
$$g_{\omega\pi^0\gamma} = \left(\frac{2}{3}\mu_u + \frac{1}{3}\mu_d\right)\cos\alpha_V \tag{3.5}$$
$$g_{\omega\eta\gamma} = -\frac{1}{3}(2\mu_u - \mu_d)\cos\alpha_V \sin\alpha_P - \frac{2}{3}\mu_s \sin\alpha_V \cos\alpha_P \tag{3.6}$$

3.4 Exact SU(3) Symmetry and Nonet Symmetry

If we impose exact SU(3) symmetry or exact nonet symmetry, that is

$$\mu_u = \mu_d = \mu_s$$

or

$$g_{88} = g_{18} = g_{81}$$

and assume the mixing is $\alpha_V = 0$ and $\alpha_P = -45°$, then the Vector Dominance Model and Static Quark Model give same result, and agree reasonably well with the experimental data.

Table 3.3 shows the prediction from such an assumption and the measured rates. We see good agreement within two sigmas for all measurements except for the decay $\phi \rightarrow \pi^0\gamma$ which is prohibited by exact SU(3) symmetry. Note that the absolute rates are not predicted by theory, only the relative rates.

Decay	Rel. $\lvert M\rvert^2$	Phase Space	Rel. Ratio	PDG (keV)
$\omega \to \pi^0\gamma$	1	0.0549	720	720 ± 40
$\omega \to \eta\gamma$	$\frac{1}{18}$	0.0079	5	7 ± 2
$\rho \to \pi^0\gamma$	$\frac{1}{9}$	0.0527	80	120 ± 30
$\rho \to \eta\gamma$	$\frac{1}{2}$	0.0073	470	570 ± 110
$\phi \to \pi^0\gamma$	0	0.1258	0	5.8 ± 0.6
$\phi \to \eta\gamma$	$\frac{4}{18}$	0.0474	52	57 ± 3

Table 3.3: Exact SU(3) predictions for selected decays

Reference	*Model or ω source*	BR($\omega \to \eta\gamma$) [10^{-4}]	BR($\rho^0 \to \eta\gamma$) [10^{-4}]
Zhong[15] **	Exact SU(3)	10.1	
Zhong[15] **	Broken SU(3)	5.2	
Benayoun[16]	Fractional Quark Chrg	6.14 ± 0.58	
	Integral Quark Chrg	3.27 ± 0.44	
Barik[17]	Set "1"	6.5	
	Set "2"	6.76	
	Static	5.8	
Singer[18]	Cloudy Bag	2.7	
Zhong[15]	M1 Cloudy Bag	3.1 – 3.3	
Bramon[19]	Broken SU(3)	6.1 ± 0.7	
Dolinksy[20]	$e^+e^- \to \omega$	$6.4^{+7.0}_{-4.7}$	4.0 ± 1.1 (+)
Alde[21]	$\pi^- p \to \omega n$	8.3 ± 2.1	–
CB[27]	$p\overline{p} \to \omega\eta$	6.6 ± 1.7	–
This measurement	$p\overline{p} \to \omega\eta$	$(2.1 \pm 1.3) \times 10^{-4}$	N/A

Table 3.4: Various theories on radiative meson decays and their predictions for BR($\omega \to \eta\gamma$)

3.5 Other theories

Agreement with data can be improved by breaking symmetry by different methods, including adding quark mass effects, direct strange quark symmetry breaking, and/or octet vs. singlet differences. Relativistic corrections can be included as well.

The Chanowitz Equations also allow an interesting modification to the quark model by setting its parameter $\xi = 2$, which gives the quarks integral charges rather than fractional charges[16].

The Cloudy Bag Model uses a Lagrangian which seems to be a mixture of QCD and ChPT at the same time, i.e. quark fields and meson fields, and the matrix element takes 2 pages to write down [18], [15].

However, the current data in general is not precise enough to really separate any of the models, as seen in table 3.4. Also, some of these models only provide constraints to the relative branching ratios and can arrive at predictions based on fits to a complete set of data. Thus the theoretical value is not unbiased towards the measurements.

Chapter 4

The detector

4.1 Overview

The CERN Crystal Barrel detector's main physics program is meson spectroscopy through antiproton-nucleon annihilations. The detector receives cooled antiprotons from the Low Energy Antiproton Ring, which annihilate on a fixed target, producing charged and neutral particles which are measured with high precision and nearly full solid angle coverage. Within the volume of the annihilation region, very short lived intermediate state mesons are formed and decay; these are the states in which we are interested. In other analyses, we search for "exotic" meson states that do not fit the standard quark-antiquark meson model, such as glueballs or hybrids. In this analysis, we study the decay rate a particular well-known meson, the ω.

4.2 Low Energy Antiproton Ring (LEAR)

The study of $p\overline{p}$ annihilations at rest requires two things, a source of $\bar{p}$ and a way to slow them down. The CERN Proton-Synchrotron Complex contains the system for these two requirements. Protons are initially accelerated to several GeV in the Proton-Synchrotron. They are extracted in bunches of 10^{13} and are directed to an iridium target. The interaction with the target produces 10^7 antiprotons that are collected and cooled by the Antiproton Accumulator complex. When a sufficient number are accumulated, a packet of 10^{10} is sent to the Low Energy Antiproton Ring at 600 MeV for further cooling. Electron cooling is used to cool the antiprotons to 200 MeV. This works by injecting a parallel beam of transversely cold electrons into a straight section of the antiproton beam. The electrons absorb the transverse momentum of the antiprotons and then are scattered out of the beam. The antiprotons are then very slowly extracted at a rate of 10-100 kHz by means of an electrostatic foil that slices off the edge of the beam profile. See figure 4.1 for a diagram of the PS Complex.

The Crystal Barrel nominally receives antiprotons at 20 kHz, over a spill run that nominally lasts a half hour. Between spills, the detector is calibrated.

4.3 The Crystal Barrel Experiment

The Crystal Barrel Experiment was designed as a high resolution detector for gamma rays, as well as having charged particle tracking. The antiprotons from the LEAR annihilate on nucleons, protons in the case of a hydrogen target or protons and neutrons in the case of a deuterium target. Because the annihilation spin state is a function of the density, a liquid or gaseous target can be used. However, in this analysis only data taken with the liquid hydrogen target was used. See figure 4.2.

The main trigger for this analysis is called the "0-prong" or "all neutral trigger". The lowest part of the trigger requires a hit in the upstream counter and no corresponding veto hit in the downstream counter, indicating that the incoming antiproton annihilated on the target and did not escape. Surrounding the target are two layers of proportional wire chambers (PWC1 and PWC2). The 0-prong trigger requires no hits in either chamber, thus vetoing events that contain charge particles. A jet drift chamber (JDC) surrounds the PWC, but for this analysis it was not used in its usual momentum measuring mode for there are no charged particles. It was used only as an additional off-line veto.

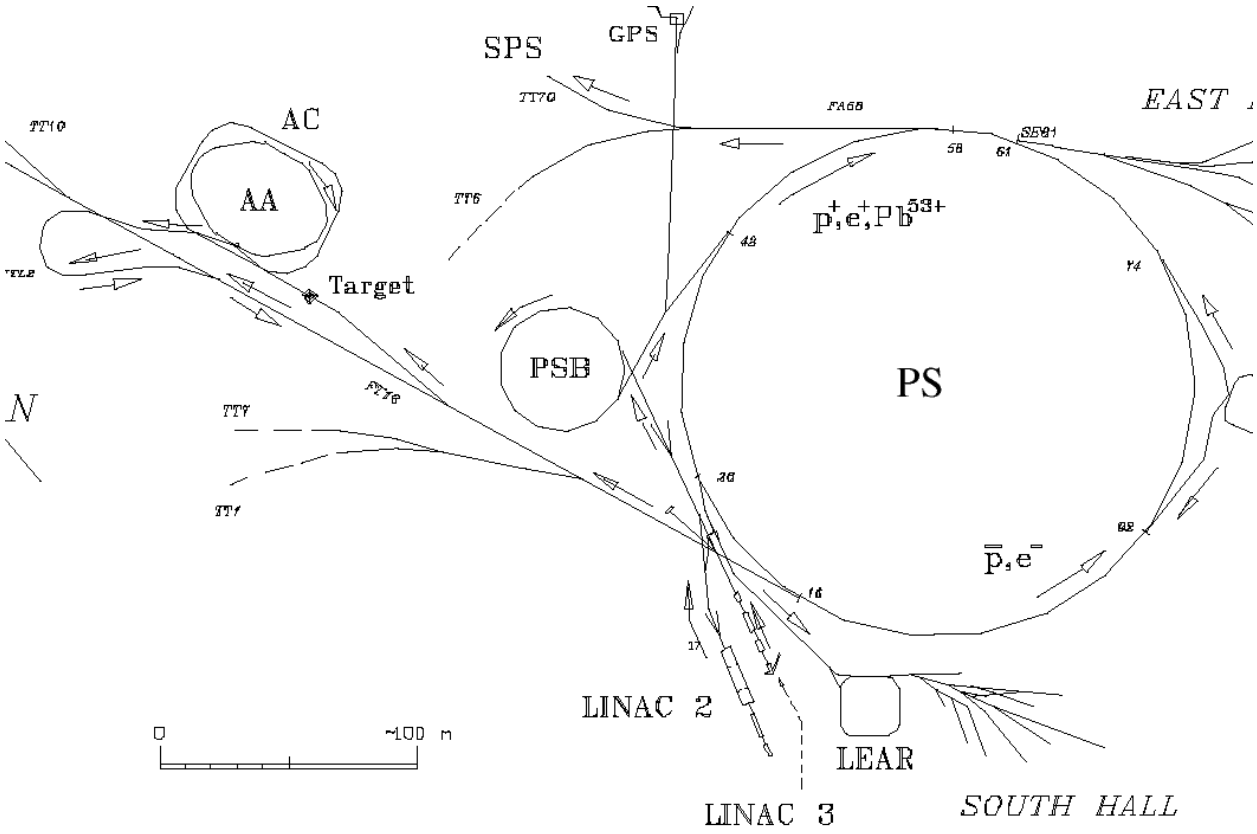

Figure 4.1: The PS complex. Protons produced in the Linac 2 are accelerated to several GeV in the PSB and PS. They impact on a target and a small fraction produces antiprotons, which are accumulated in the AA and then transfered to LEAR. After final cooling, the antiprotons are slowly extracted to the experiments in the switch-yard.

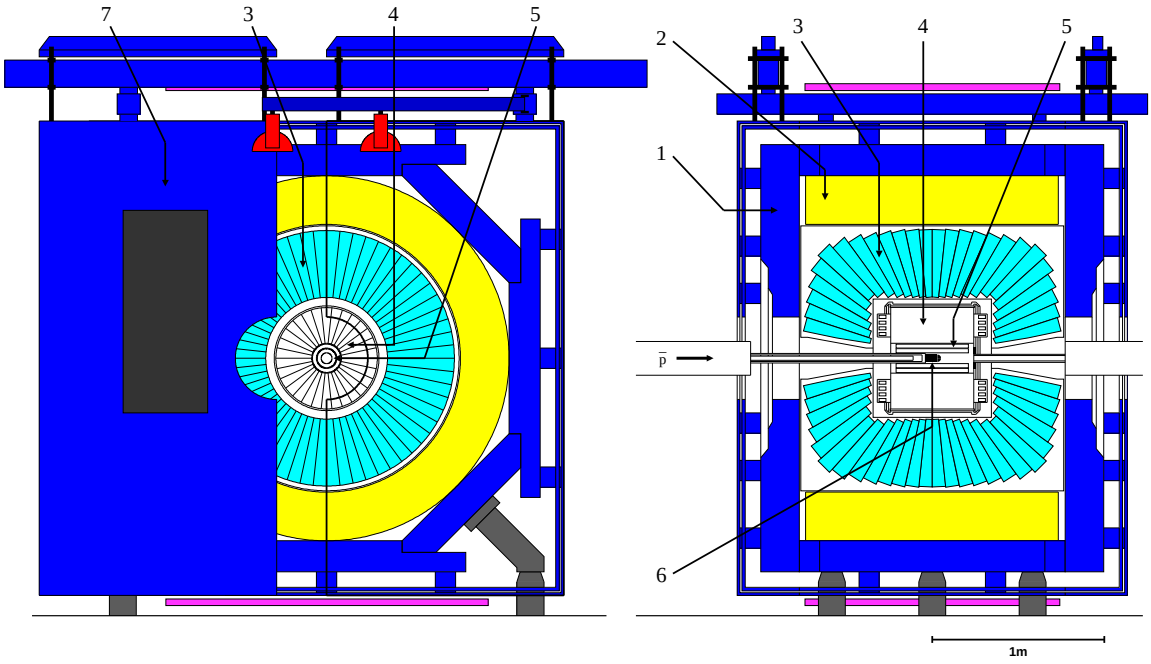

Figure 4.2: Overall layout of the Crystal Barrel detector showing (1) magnet yoke, (2) magnet coils, (3) CsI barrel, (4) jet drift chamber, (5) proportional chamber, (6) liquid hydrogen target, (7) one half of the end-plate. (left) view as seen by incoming antiproton (right) side view.

When the main trigger fires, all crystals values are digitized, pedestal subtracted, zero suppressed, and gathered into an event, and eventually written to magnetic tape. Over the period 1989 to 1994, over 20 million 0-prong events in liquid hydrogen were collected on tape.

4.4 Crystal Calorimeters

The gamma rays are detected by 1380 Cesium-Iodide crystal scintillators, arranged in a projective geometry that covers 95% of the total solid angle. The crystals are 16 radiation lengths long (30 cm). The scintillation light is read out on the back-end via a wavelength-shifting plastic coupled to a photodiode. The photodiode is digitally sampled with two independent ADC's, the 2282's and the FERA's, to increase the dynamic range, and for internal integrity checks. The crystals are arranged in a $6° \times 6°$ array, and provide an angular resolution of $1.5°$ when the center of gravity of a cluster of crystals is considered. The energy resolution is $2.5\%/\sqrt[4]{E(\mathrm{GeV})}$, resulting in $\sigma(m_{\pi^0}) = 8MeV$ and $\sigma(m_\eta) = 17MeV$.

In between antiproton spills from LEAR, the readout electronics are calibrated with a Xenon flash lamp whose output is channeled to each crystal by a fiber optic. Also, the no-signal pedestals are measured and applied for the next spill.

4.5 Reconstruction Algorithm

All particles can trigger a shower in the crystals. Every localized shower (whether electro-magnetic or hadronic) is called a Particle Energy Deposition (PED). Hadronic showers can not be well measured in the crystals. If the hadron was charged, these PEDs can be removed by connecting them with the appropriate track. Other PEDs are most likely to be the result of γ ray photons. The reconstruction algorithm attempts to accurately identify all of the PEDs in an event, with the goal of making a one to one mapping of "good" PED to photon.

The electro-magnetic shower of a gamma ray interaction covers many contiguous crystals. Thus the reconstruction software first identifies contiguous clusters of crystals. The criteria for starting a cluster is that a seed crystal have an energy above a certain threshold called the cluster crystal threshold. All contiguous neighbor crystals above 1 MeV are added to the cluster. Because the cluster may be the result of more than one photon, secondary local maxima are searched for in the cluster. The energy of the secondary local maxima must be above the secondary-PED crystal threshold.

Finally, one can apply an absolute energy cut on the total reconstructed PED. The previous two thresholds are crystal thresholds rather than PEDs thresholds.

After the γ's are reconstructed, their resolutions can be improved by means of a fit to certain constraints. Because the final strong annihilation occurs at rest, the total four-momentum is known to be (0,0,0; 1876) MeV. This provides four constraints to the fit. Additionally, if the γ's are the result of decays from narrow resonances, such as $\pi^0 \rightarrow \gamma\gamma$ or $\eta \rightarrow \gamma\gamma$, the invariant masses of those γ's can be additional constraints. For this analysis, the final states are $\eta\eta\gamma$, $\eta\pi^0\gamma$ and $\pi^0\pi^0\gamma$, so the final kinematic fits have six constraints. The results of the fit are two-fold. First, it returns slightly modified momenta of each γ, which more accurately describe the true momenta. Second, it returns a probabilistic confidence level that the given event satisfied the applied decay hypothesis. This can be used to select the desired channels and reject background channels. The fit is described in more detail in appendix 10.1.

Chapter 5

Monte Carlo Simulation

5.1 Introduction

CBGEANT, version 5.05.04 was used to generate over a million MC events for this analysis. Over 97% of these events were simulations of backgrounds which have a small efficiency of being detected in the wrong final state but which are still large compared to the data; the remaining 3% of events are simulations of the signal channel ($\eta((\omega/\rho^0)\to\eta\gamma)$).

The two main background types are due to (a) mismatching $\gamma\gamma$ to fake η's or fake π^0's (in 5 γ states) and (b) 6 γ states that lose one γ and appear as 5 γ states. There are also 5 γ non-resonant backgrounds, as well as backgrounds from 4 γ final states that acquire a spurious split-off.

These methods for reducing these backgrounds are discussed in chapter 8.

5.2 List of Monte Carlo data sets

Short name	Events	Description
`lbl`	20,318,391	real data (from "LBLxxx" tapes)
`eoeg`	9,965	$p\overline{p}\to\eta\omega$, $\omega\to\eta\gamma$, $\eta\to\gamma\gamma$
`eopg`	568,928	$p\overline{p}\to\eta\omega$, $\omega\to\eta\gamma$, $\eta\to\gamma\gamma$, $\pi^0\to\gamma\gamma$
`popg`	99,963	$p\overline{p}\to\pi^0\omega$, $\omega\to\pi^0\gamma$, $\pi^0\to\gamma\gamma$
`eep`	1,104,150	$p\overline{p}\to\pi^0\eta\eta$, $\eta\to\gamma\gamma$, $\pi^0\to\gamma\gamma$
`epp`	788,911	$p\overline{p}\to\pi^0\pi^0\eta$, $\eta\to\gamma\gamma$, $\pi^0\to\gamma\gamma$
`ppp`	600,000	$p\overline{p}\to\pi^0\pi^0\pi^0$, $\pi^0\to\gamma\gamma$
`epg`	50,000	$p\overline{p}\to\pi^0\eta\gamma$, $\eta\to\gamma\gamma$, $\pi^0\to\gamma\gamma$
`eeg`	150,000	$p\overline{p}\to\eta\eta\gamma$, $\eta\to\gamma\gamma$
`ppg`	50,000	$p\overline{p}\to\pi^0\pi^0\gamma$, $\pi^0\to\gamma\gamma$
`ee`	100,000	$p\overline{p}\to\eta\eta$, $\eta\to\gamma\gamma$
`pp`	100,000	$p\overline{p}\to\pi^0\pi^0$, $\pi^0\to\gamma\gamma$

5.3 GEANT software

The CERN code package GEANT, version 3.21, is used to simulate the propagation of the initial annihilation particles through the detector, applying energy losses, and interactions with the active detector elements. Although not critical for this analysis because there are no direct hadrons interacting with the detector (only γ's), the GHEISHA package was used for tracking spurious hadrons. The events were generated using a hit/miss algorithm that results in the events being flat in phase space, that is each event has an inherent weight of unity. Resonances with a sufficiently wide width are generated with a non-relativistic Breit-Wigner distribution in mass. Because some events generated with this Breit-Wigner lie outside phase space, a very small fraction of events are rejected in the generation phase (for example 0.00036 in $\pi^0(\omega\to\pi^0\gamma)$). Post-reconstruction weighting was done via a variety of methods for the different channels.

5.4 Angular dependence of ω decay

Because the ω does not decay isotropically in its rest-frame (because it is polarized by annihilation selection rules), the Monte Carlo must be weighted to reflect this. See appendix 10.2 for a theoretical description of the angular distributions. The angular distribution is of the form

$$f(\theta) = (1 + b\cos^2\theta)/(1 + b/3),$$

where b was measured to be $b = 1.04 \pm 0.03$. This value was determined by fitting the angular distribution of the data for the channel $\eta(\omega \to \pi^0\gamma)$, after subtracting the expected background from $\pi^0\pi^0\eta$ and dividing by the efficiency for $\eta(\omega \to \pi^0\gamma)$. The allowed physical range for b is $b \leq 1$, so the value of b is fixed to 1, and the error is increased to 0.04. This value is consistent with annihilation from ${}^3S_1$. The function is normalized to average one from $\theta = 0 \to \pi$.

5.5 Dalitz plot weighting of 3 pseudoscalar channels

The background channels, $\pi^0\eta\eta$, $\pi^0\pi^0\eta$ and $\pi^0\pi^0\pi^0$, are rich in Dalitz plot structure, specifically, f and a scalar resonances. The Crystal Barrel has published analyses of all three channels, and the acceptance corrected Dalitz plots were used to weight these channels so that they reflect the resonance structure. Each Monte Carlo event is mapped to a bin in the Dalitz plot, using the initially generated momenta of the three mesons. The weights are normalized to average unity over the Dalitz plot. Edge bins which do not lie entirely in allowed phase-space are not corrected, but because of the small bin size, the net result is not significant, and because the effect is only on the edge, it is not correlated to the measurement of interest along the omega bands.

5.6 Weighting the ρ^0/ω interference channel

Because isospin is not the decay, the decay $\omega \to \eta\gamma$ can interfere coherently with the decay $\rho^0 \to \eta\gamma$. In addition, there is direct mixing between ω and ρ^0 states by off-diagonal components of the mass matrix in the isospin eigenstate basis.

We write the net amplitude with the phenomenological model,

$$S = (A_{\rho^0{}_I} A_{\omega_I}) \left(m - \begin{bmatrix} m^*_{\rho^0{}_I} & -\delta \\ -\delta & m^*_{\omega_I} \end{bmatrix} \right)^{-1} \begin{pmatrix} T_{\rho^0{}_I} \\ T_{\omega_I} \end{pmatrix}$$

where A_x are the complex production amplitudes, T_x are the complex decay amplitudes, m is the $\eta\gamma$ or $\pi^0\gamma$ mass, m^*_x are the complex masses ($= m + i\Gamma/2$), and δ is the mass mixing term, measured to be $\delta = 2.5$ MeV from many experiments[29], [23]. The I subscripts indicate that these are isospin eigenstates, not the physical vector mesons. We can expand this equation to first order in δ/m_ω.

$$S = \frac{A_{\rho^0{}_I} T_{\rho^0{}_I}}{m - m^*_{\rho^0{}_I}} + \frac{A_{\omega_I} T_{\omega_I}}{m - m^*_{\omega_I}} + \frac{\delta(A_{\rho^0{}_I} T_{\omega_I} + A_{\omega_I} T_{\rho^0{}_I})}{(m - m^*_{\rho^0{}_I})(m - m^*_{\omega_I})}$$

or equivalently,

$$S = \frac{A_{\rho^0{}_I} T_{\rho^0{}_I}}{m - m^*_{\rho^0{}_I}} \left(1 + \frac{T_{\omega_I}\delta}{T_{\rho^0{}_I}(m - m^*_{\omega_I})} \right) + \frac{A_{\omega_I} T_{\omega_I}}{m - m^*_{\omega_I}} \left(1 + \frac{T_{\rho^0{}_I}\delta}{T_{\omega_I}(m - m^*_{\rho^0{}_I})} \right)$$

Most of the work in this area has concerned the not-so-rare decays into $\pi^+\pi^-$, rather than the rare decays into $\eta\gamma$.

In the absence of isospin breaking, the third term vanishes. In the approximation that $A_{\rho^0} \sim A_\omega$ and $T_{\rho^0} \sim T_\omega$, but $\Gamma_{\rho^0}/\Gamma_{\omega m} = 20$, the third term is roughly a factor of 30 smaller than the second term at the omega mass. When the total amplitude is squared, this isospin term becomes smaller.

The complex phase of $\alpha = \arg(A_{\rho^0}/A_\omega)$ for the productions in $p\overline{p}\to\rho^0\eta$ and $p\overline{p}\to\omega\eta$ has been measured to be $\alpha = -5.4 \pm 4.3°$ [24]. This supports the quark model of $p\overline{p}$ annihilation, which predicts the phase to be zero. We fix $\alpha = 0$ in this analysis. We note in passing that this production phase in other processes ($e^+e^-\to\pi^+\pi^-$, $\pi^+p\to\pi^+\pi^-\Delta^{++}$, $\pi^-p\to\pi^+\pi^-n$) is always $0,\pm\pi/2$ or π [30]. The low statistics do not allow a definitive determination of this phase, although some preliminary tests showed that $\alpha = 0$ was favored over $\alpha = \pi$.

The complex phase of $\phi = \arg(T_{\rho^0}/T_\omega)$ for the decays $V\to P\gamma$ (V=ρ^0 or ω, P=η or π^0) is either 0 or π, because the decay amplitudes are real in the quark model (the dipole spin-flip operator results in real magnetic moments). Using typical values for the pseudoscalar and vector mixing angles, the phase is zero. We fix this phase to zero also because we believe the quark model.

The production of ρ^0 and ω is believed to be totally coherent in the case where the particles are created and decay in strong reactions [24]. We call this theory type I, which is strictly used in a previous paper by the Crystal Barrel[27] for $\eta((\omega/\rho^0)\to\eta\gamma)$.

However, the decay into $\pi^+\pi^-$ is very different from the decay into $\eta\gamma$. The former decay is a strong decay which occurs very near the original $p\overline{p}$ annihilation. Because ω is forbidden to decay into $\pi^+\pi^-$ by isospin conservation, it can only decay if it mixes into a ρ^0. However, the decay $\eta\gamma$ is electro-magnetic and does not need to conserve isospin in the decay. Also because the radiative decay happens far from the initial $p\overline{p}$ annihilation, the amount of interference between ρ^0 and ω is limited to the relatively small amount of eigenstate mixing between the two. If there is no isospin mixing of eigenstates, then the two channels of $\omega\to\eta\gamma$ and $\rho^0\to\eta\gamma$ may proceed totally incoherently. Thus the slight correction for interference only happens for the small fraction of mixed state. We label this intensity type II.

For comparison and to show that the intrinsic isospin mixing is small, a third assumption is created where there is no interference and no mixing between ρ^0 and ω is labeled type III. Fits to these three types (I,II and III) are given in chapter 9.

We generate the decay particles flat in phase space (i.e. $\eta\eta\gamma$ and $\eta\pi^0\gamma$). We then calculate the intensity for each event using the following amplitudes,

$$|S|^2(I) = |S_{\omega'} + S_{\rho'}|^2 \tag{5.1}$$

$$|S|^2(II) = |S_{\omega'}|^2 + |S_{\rho'}|^2 \tag{5.2}$$

$$|S|^2(III) = |S_\omega|^2 + |S_\rho|^2 \tag{5.3}$$

$$S_x = \frac{\alpha_x}{\sqrt{2\pi}} \frac{|A_x||T_x|}{m - m_x + i\Gamma_x/2} \tag{5.4}$$

$$S_{x'} = S_x \times \left(1 - \frac{|A_y|}{|A_x|} \frac{\delta e^{\pm\phi}}{m - m_x + i\Gamma_x/2}\right) \tag{5.5}$$

$$|A_x| = \sqrt{\beta_x BR(p\overline{p}\to x\eta)} \tag{5.6}$$

$$|T_x| = \sqrt{BR(x\to\eta\gamma)\Gamma_x} \tag{5.7}$$

where x (y) is $\omega(\rho^0)$ or $\rho^0(\omega)$ and the prime denotes corrections for direct ρ^0/ω isospin mixing. The mixing parameter is $\delta = 2.5$ MeV[22]. The α_x is a normalization factor, such that the integral over the Dalitz plot of the $|S_x|^2$ with $\delta = 0$ and $\Gamma\to 0$ is simply the net branching ratio, that is

$$\alpha_x \int\int_{dalitz} dLIPS|S - x|^2 = \beta_x \mathrm{BR}(pbarp\to X\eta\to\eta\eta\gamma)$$

When $\Gamma \neq 0$, the Monte Carlo efficiency automatically takes care of the phase space correction, so no additional correction is needed. The β_x is a correction coefficient to tabulated production branching ratios. Crystal Barrel production branching ratios are the integrated intensity over all of phase space of the resonance (ω or ρ^0 in this case), and thus have an inherent phase-space correction that must be removed in order to get the correct amplitude. The correction is calculated by comparing the integrated infinite-phase-space Breit-Wigner to the integrated Dalitz-limited-phase-space Breit-Wigner.

$$\beta_x = \frac{\int_{-\infty}^{\infty} |\mathrm{BW}_x(m)|^2 p(m_x) dm}{\int_{-\infty}^{\infty} |\mathrm{BW}_x(m)|^2 p(m) dm} \tag{5.8}$$

where $p(m)$ is the momentum of the $(\eta\gamma)$ system in the $p\overline{p}$ restframe as a function of mass $m(\eta\gamma)$, and $p(m_x)$ is evaluated at the mass of x. We define the decay branching ratio of a broad resonance x at the

process	BR (10^{-3})	Ref	process	BR (10^{-3})	Ref
$p\overline{p}\to\eta\omega$	15.1 ± 1.2	[8]	$p\overline{p}\to\eta\rho^0$	3.9 ± 0.3	[24]
$p\overline{p}\to\pi^0\omega$	5.7 ± 0.3	[8]	$p\overline{p}\to\pi^0\rho^0$	17 ± 3	[12]
$\omega\to\eta\gamma$	0.83 ± 0.21	[14]	$\rho^0\to\eta\gamma$	0.38 ± 0.07	[14]
$\eta\to\gamma\gamma$	392.5	[14]			
Parameter	value	Ref	Parameter	value	Ref
Γ_ω	8.43 MeV	[14]	Γ_{ρ^0}	150.7 MeV	[14]
$\alpha_{\eta\omega}$	771.7 MeV		$\alpha_{\eta\rho^0}$	804.0 MeV	
$\alpha_{\pi^0\omega}$	1423.0 MeV		$\alpha_{\pi^0\rho^0}$	1487.9 MeV	
$\beta_{\eta\omega}$	1.002		$\beta_{\eta\rho^0}$	1.039	
$\beta_{\pi^0\omega}$	1.001		$\beta_{\pi^0\rho^0}$	1.023	

Table 5.1: BW parameters

standard mean mass of the resonance m_x, and allow the phase-space corrections to be calculated directly by the Monte Carlo, so no additional corrections are needed for the amplitude or for a mass dependent width; these are included in the Monte Carlo efficiency. These corrections, of course, apply mostly to the ρ^0 whose width significantly exceeds the limits of 3-body phase space.

On top of this intensity weighting, the events are also weighted according to their decay angle distribution, as in section 5.4.

5.7 The flat 3-body channels, $p\overline{p}\to\eta\eta\gamma$, $\pi^0\eta\gamma$ and $\pi^0\pi^0\gamma$

The non-resonant channels, $p\overline{p}\to\eta\eta\gamma$, $\pi^0\eta\gamma$ and $\pi^0\pi^0\gamma$, have not been previously measured because they are predicted to be rare and also impossible to measure in bubble chamber experiments.

The rate of $p\overline{p}\to\eta\eta\gamma$ can be estimated by invoking vector dominance, which relates EM rates to QCD rates with a factor of the fine structure constant. In this case, we would want to know the rates of $p\overline{p}\to\eta\eta\omega$ and $p\overline{p}\to\eta\eta\rho^0$, then use the couplings of ω or ρ^0 to γ, which is

$$g_{\rho\gamma} = 3g_{\omega\gamma} = 3.03 \times 10^{-3}$$

and then multiply by phase space corrections. The measurements of the ρ^0 channels are not available, but we can guess that they are approximately the same, since the rate for $p\overline{p}\to\omega\pi^+\pi^-$ and the rate for $p\overline{p}\to\rho^0\pi^+\pi^-$ are approximately the same. If they are indeed the same, then the coupling factor is simply $g^2_{\rho\gamma}$ because $g^2_{\omega\gamma}$ is an order of magnitude smaller. The phase space ratios are approximatel LIPS($\pi^0\pi^0\gamma$)/LIPS($\pi^0\pi^0\rho^0$) ≈ 2 and LIPS($\pi^0\eta\gamma$)/LIPS($\pi^0\eta\rho^0$) ≈ 4.

[branching ratios from [8]]

Reaction $p\overline{p}\to$	BR (10^{-3}) X = ρ^0	PS(X=γ)/PS(X=ρ^0) factor	BR (10^{-5}) X=γ
$\pi^0\pi^0$X	20.0	2	12
$\pi^0\eta$X	6.8	4	8

The reaction $p\overline{p}\to\eta\eta\omega$ has not been measured because it has nearly no available phase space. We can only relate $p\overline{p}\to\eta\eta\gamma$ to the other radiative annihilations via phase space ratios. (The phase space for $\eta\eta\gamma$ is much, much greater (perhaps 3-4 orders of magnitude) than $\eta\eta\omega$. It is curious to note that m(η) +m(η) + m(ω) = 1876.84, while m($p\overline{p}$) = 1876.54!)

Using LIPS($\eta\eta\gamma$)/LIPS($\pi^0\pi^0\gamma$) = 0.2 and LIPS($\eta\eta\gamma$)/LIPS($\pi^0\eta\gamma$) = 0.5, we get BR($\eta\eta\gamma$) = $(2-4)\times10^{-5}$.

We compare our naive calculations to the values derived in chapter 9.

Reaction	BR (10^{-5}) prediction	seen
$p\overline{p}\to\pi^0\pi^0\gamma$	12	$8.8^{+6.2}_{-8.8}$
$p\overline{p}\to\pi^0\eta\gamma$	8	$25.0^{+5.0}_{-25.0}$
$p\overline{p}\to\eta\eta\gamma$	2 - 4	$1.9^{+1.6}_{-1.9}$

The agreement is ok for two cases, but poor for the third. However, we have neglected phase space factors and have been lazy in using the ρ^0 VMD constant instead of ω, so all of these numbers are just order of magnitude calculations.

The $\eta\eta\gamma$ background was included in the fits to improve their results. The χ^2 fell significantly (see table 9.2) and the dependence on the confidence level for the background $\pi^0\eta\eta$ vanished when the $\eta\eta\gamma$ background was included. The dependence vanished because of the difference in the confidence levels of $\pi^0\eta\eta$ vs. $\eta\eta\gamma$. Because $\pi^0\eta\eta$ is missing a photon, it is biased to have too low an energy and thus a bad confidence level distribution that falls with increasing confidence level. On the other hand, $\eta\eta\gamma$ is a perfect match for the kinematic fit and thus has a perfectly flat confidence level. By describing the background as a sum of $\pi^0\eta\eta$(with a falling CL) and $\eta\eta\gamma$(with a flat CL), the fit values were constant regardless of what CL was used. Without the $\eta\eta\gamma$ background, the fit value for $\pi^0\eta\eta$ rose significantly as the CL cut was increased.

Because the measurement of these backgrounds is highly correlated to the 3-pseudoscalar backgrounds and it is possible that the Monte Carlo simulation of the 3-pseudoscalar backgrounds could be inaccurate, we do not wish to claim discovery of these channels, but we do claim that the data supports their existence at the given intensities. We assign the largest portion of the systematic error later in this paper to our ignorance of whether or not these channels really exist, which amounts to an error of 20% because the shape of the background under the ω peak is slightly different.

The existence of the $\eta\eta\gamma$ background plays an enormous role in the alternate analysis by the Crystal Barrel [27], where the measured value of BR($\omega\rightarrow\eta\gamma$) changes by a factor of two if this background is included in the background subtraction. We note that the two analyses agree well if the $\eta\eta\gamma$ channel is included, but disagree if not. See the separate report [32] for a detailed comparison between the two analyses.

Chapter 6

First Skimming Pass

6.1 Introduction

The data cuts are summarized in table 6.3, and described briefly below. Antiprotons from the 200 MeV LEAR beam are captured in liquid hydrogen and annihilate at rest. Events with no charged tracks detected in the two layer proportional wire chamber (PWC) are written to tape, resulting in nearly 20 million events accumulated over 9 run periods spanning four years.

Unwanted events with charged tracks that passed through the trigger are removed first, with a track defined as 3 or more hits on a helix.

Photons are reconstructed as follows. The gamma reconstruction algorithm forms contiguous clusters of fired crystals, with a minimum of 20 MeV for the most energetic crystal of the cluster and a minimum of 1 MeV for all other crystals. Then local maxima within the clusters are identified as distinct gammas, provided the maximum energy crystal of the local maxima also has 20 MeV. The threshold of 20 MeV suppresses the presence of *split-offs*, which are a result of one gamma forming two or more clusters because of shower fluctuations or other crystal inefficiencies. These split-offs artificially raise the total gamma multiplicity and thus reduce the efficiency.

All PEDs are assumed to be zero mass gamma ray photons. PEDs that are the result of K_L interaction with the barrel will be removed by total energy and momentum conservation.

Events with total energy and momentum consistent with annihilation at rest ($p_{\mathrm{tot}} = (0, 0, 0; 1876)$ MeV) are kept, if the difference for each component is less than 200 MeV. A tighter selection is done later. Events with exactly five gammas are retained. The number of final events in the skimming pass are given in table 6.3.

6.2 Software

The analysis program was Cboff-LBL++, a C++ class library that encapsulates the Fortran Crystal Barrel libraries of CCBCDB, GTRACK, BCTRAK and LOCATER, replacing the CBOFF library. It relies heavily on the CLHEP-0.15 class library. CLHEP is still in the development stage.

DSPT 0 gives 20/20 MeV cuts on gamma reconstruction; see table 6.2 for all the reconstruction cards. Also FFUZ was used for tracking (the default).

Package	Version	Package	Version
cboff:	1.30/10	locater:	2.01/11
bctrak:	2.04/03	gtrack:	1.37/01
ccdbcb:	2.05/01	cbkfit:	3.09/00
cbdrop:	1.11/03	cbgeant:	5.05/04

Table 6.1: CBOFF software versions used

```
cboff steering cards:
CHAM 'TRAK' 'RAWS' 'GPWC' 'PATT' 'CIRC' 'HELX'
XTAL 'TRAK' 'DECF' 'DECL' 'ALCE' 'CLST' 'PEDS' 'PDRG'
GLOB 'TRAK' 'MTCH'
BANK 'GLOB'
DSTP 0
```

Table 6.2: The steering cards used for cboff

cut	LBL	$\pi^0\eta\eta$	$\pi^0\pi^0\eta$	$\pi^0\pi^0\pi^0$	$\eta(\omega\to\eta\gamma)$	$\eta(\omega\to\pi^0\gamma)$
Event in	20298446	1104150	788911	600000	9965	568928
0 tracks	18223703	1006509	719152	530391	9398	523279
$\|\vec{p}\| < 200$ MeV	13525910	852225	616544	456845	8045	446242
$\|E - 1876\| < 200$ MeV	11699206	822935	596600	441654	7815	433559
5 gammas	1154964	109198	99961	87248	6754	355258
cut	$\pi^0(\omega\to\pi^0\gamma)$	$\pi^0\pi^0$	$\eta\eta$	$\pi^0\pi^0\gamma$	$\eta\eta\gamma$	$\eta\pi^0\gamma$
Event in	99963	100000	100000	50000	150000	50000
0 tracks	90487	91932	93541	45268	138277	45789
$\|\vec{p}\| < 200$ MeV	77306	82323	79987	38954	116359	38904
$\|E - 1876\| < 200$ MeV	75177	79180	77875	37885	113012	37793
5 gammas	59555	4264	5885	29392	97205	30827

Table 6.3: Cut results for various data sets in "skim" pass

6.3 Data quality

There are two types of runs that are to be rejected.

1. "Wrong" runs are runs that used a trigger that might not have been a real 0-prong trigger, based on the run database.

```
 5809 GH3012 LB0010 ------   4231  2H6  1-May-91 BJ-PST-                IA
 5810 GH3012 LB0010 ------   6016  2H6  1-May-91 BJ-PST-                IA
 7015 GH3605 LB0010 ------   2041  2H9 12-Jun-91 B--PST-             4+Lprng
 7996 GH3963 LB0011 ------  20391  2H6 12-Aug-91 BJ-PST-             minbias
 8001 GH3966 LB0011 ------    269  2H6 12-Aug-91 BJ-PST-             minbias
16084 -???32 LB0011 ------     -1 ---- --------- -------             unknown
16146 -???43 LB0011 ------   1217 ---- --------- -------             unknown
16172 -???44 LB0011 ------     -1 ---- --------- -------             unknown
16173 -???44 LB0011 ------     -1 ---- --------- -------             unknown
16177 -???44 LB0011 ------     -1 ---- --------- -------             unknown
20352 GH7546 LB0011 ------   1735  2xx 30-Oct-93 BJ-PST-    minbias;nigelflag
20353 GH7546 LB0011 ------  11503  2xx 30-Oct-93 BJ-PST-      minbias;default
20358 GH7--- LB0011 ------     -1  2Hx  x-Oct-93 -------              noinfo
 3636 GH1938 LB0012 ------   9304  2H6  9-Oct-90 -------             unknown
 3848 GH2060 LB0012 ------   6143  2H9 12-Oct-90 BJ-PS--             minbias
 4049 GH2190 LB0012 ------     -1  2E6 15-Oct-90 BJ-PS--               0prng
 4050 GH2190 LB0012 ------   2607  2E6 15-Oct-90 BJ-PS--               0prng
 1272 GH0795 LB0012 ------   5795  2H9 16-Dec-89 B------            pedestal
 1277 GH0799 LB0012 ------   6017  2H9 16-Dec-89 B------            pedestal
 1288 GH0804 LB0012 ------   4812  2H0 17-Dec-89 BJ--S--               0prng
 1288 GH0804 LB0012 ------   4812  2H0 17-Dec-89 BJ--S--               0prng
 1289 GH0804 LB0012 ------   4374  2H0 17-Dec-89 BJ--S--               0prng
 1365 GH0836 LB0012 ------      0  2H9 19-Dec-89 B------            pedestal
 1384 GH0844 LB0012 ------   5822  2H9 19-Dec-89 B------            pedestal
 1411 GH1992 LB0012 ------  16775  2H0 20-Dec-89 B------            pedestal
 1411 GH1992 LB0012 ------  16775  2H0 20-Dec-89 B------            pedestal
 4199 GH2221 LB0013 ------    366  2H6  9-Nov-90 BJ-PS--             minbias
```

Description	FORTRAN cut
Momentum/Energy Conservation efficiency	`en200/event.lt.0.4`
5 Gamma efficiency	`gamma5/event.lt.0.02`
Average gamma multiplicity	`ngamma.lt.6.or.ngamma.gt.10`
Average track multiplicity	`ntracks.lt.0.0001.or.ntracks.gt.0.5`
Average PED θ position	`abs(pedtheta).gt.0.1.and.pedtheta<20.0`

2079	2100	2131	2132	2160	2161	2165	2169	2170	2898
2932	2974	3271	3272	3273	3274	3275	3276	3277	3278
3279	3280	3281	3285	3286	3290	3299	3300	3301	3523
3524	3529	3531	3543	3614	3615	3618	3620	3624	3821
3848	4050	4133	4134	4136	4137	4199	4516	4523	4526
4988	5228	5241	5350	5351	5354	5355	6618	6672	16143
16147	16195	16197	20209	20352	20353	21344	21345	21348	21349
21351	21354	21355	21356						

Table 6.4: The cuts at the top of the table were used to identify the bad runs which are listed at the bottom of the table.

```
5252 GH2756 LB0014 ------      1  2H6 25-Nov-90 BJ-PS--             minbias
1399 GH0854 LB0017 ------   7346  2H9 20-Dec-89 BJ--S--          genericdata
```

2. "Bad" runs were identified by looking at run averages of certain parameters, and requiring them to have some some sane values. (See figure 97/05/23 00:24. in the folder).

   The cuts and the resultant bad runs are listed in table 6.3.

   The number of bad events in data runs was estimated to be about 740,000 events out of 20.4 million total data events, or 3.6% of the data. The bad runs are assumed to be very bad, in other words the data is assumed to be so corrupt that they appear as random noise, and most would probably would not pass any Kinematic Fit. At worst, they would have formed a flat background to the data. The total number of events is corrected by subtracting 3.6%.

Chapter 7

Second Kinematic Fit Pass

7.1 Description

The purpose of the first pass on the data, described in the previous chapter, was to select out 5 γ events with good 4-momentum. The purpose of the second pass, described in this chapter, is to reduce background due to channels with lost γ's and to classify the 5γ events by kinematically fit to three hypotheses.

The gamma reconstruction algorithm is rerun, this time with PED thresholds selected to maximize the value of

$$\frac{\sigma(s)}{s} = \frac{\sqrt{s+b}}{s}$$

where s is the number of signal events and b is the number of background events underneath the signal. The PED thresholds are defined as the two BCTRAK values, ECLUBC and EPEDBC, and a final energy cut on all γ's, such that γ's below this energy were not used in counting the event multiplicity. Each was varied as to maximize the value above.

The result was:

1. `ECLUBC` = 10 MeV
2. `EPEDBC` = 18 MeV
3. Gamma Energy threshold = 11 MeV

(In previous tests, we used `ECLUBC` = 3 MeV, `EPEDBC` = 3 MeV and Soft/Hard Gamma threshold = 20 MeV. PEDs between 3 and 20 MeV were classified as "soft" and treated specially. However, the results of measuring the signal and background channels did not match well with MC expectations (off by 10-20%). We believe this is because the MC does not accurately model very soft PEDs well. We include this effect in our systematic error estimate.)

Erratum We have discovered two small problems in our final data set after the analysis was completed. Neither problem has a significant impact on the final value. The problems appear to be a result of changing the PED reconstruction thresholds. A discussion appears at the end of this chapter in section 7.4.

From the hard gamma set, a kinematic fit (see appendix 10.1) is done to a phase space hypothesis,

$$p\overline{p} \rightarrow 5\gamma$$

and then three resonant hypotheses if the first fit succeeds,

$$p\overline{p} \rightarrow \pi^0\pi^0\gamma,$$

$$p\overline{p} \rightarrow \pi^0\eta\gamma,$$

$$p\overline{p} \rightarrow \eta\eta\gamma.$$

Events are accepted if and only if they pass the phase space hypothesis and exactly one of the three resonant hypotheses. The success of a fit is defined by a maximum allowed reduced $\chi^2/N_{dof} < 5$. At a slight cost of efficiency, there are no ambiguous events.

The $\pi^0\pi^0\gamma$, $\eta\pi^0\gamma$ and $\eta\eta\gamma$ events are written to HBOOK ntuples, along with some important cut variables discussed in the next chapter. The results of this pass are shown in table 7.2.

7.2 Scaling of errors for kinematic fit

The default database (cbdata.base_feb14) contains the standard calibration constants. However, these calibration constants were obtained for an unknown final states, and do not give perfect results in the kinematic fitter. There are 3 types of parameters that can be varied to give better results.

1. The neutral decay vertex is typically at $(0, 0, 0)$, but the actual position is not well known because the liquid hydrogen target does not always sit in the exact same spot. Based on the asymmetry of the pull distributions (see the section on kinematic fitter) for the θ of the reconstructed γ's, the vertex position can move a few millimeters forward or backward relative to the database values.

2. The absolute calibration coefficient for the energy of the γ's needs to be adjusted in most cases, in order to best satisfy the three constraints,

   (a) The $\pi^0 \rightarrow \gamma\gamma$ mass, 134.9764 MeV.

   (b) The $\eta \rightarrow \gamma\gamma$ mass, 547.45 MeV.

   (c) The $p\overline{p} \rightarrow 5\gamma$ total energy, 1876.543 MeV

3. The estimated $1-\sigma$ errors of the γ parameters are usually not quite right, and need to be adjusted in order for

   (a) the pull distributions of each of these parameters to be a unit Gaussian, and

   (b) the confidence level of the entire phase space fit to be flat.

In order to fix these 3 types of parameters, the following algorithm was used. The final values are given in table 7.2. [1]

1. The θ pull distribution was fitted with a Gaussian, and the mean value gives a handle on the neutral vertex position. For a fixed point on the crystal surface, as the neutral vertex moves to positive z, the θ angle increases. It is found empirically that a $+0.15$ pull offset from zero needs roughly a $+1.0$ mm correction in the vertex z position.

   This process was iterated twice until all the means were within ± 0.015, the statistical error. This included scaling00 and scaling01.

2. The total energy, $\gamma\gamma$ mass at the π^0 and the $\gamma\gamma$ mass at the η were fitted with a Gaussian plus linear background near the relative peak. Because the widths of the peaks differ, a scaling factor f was chosen that minimized the following function,

$$\chi^2 = \sum_{totalE, \pi^0, \eta \ peaks} \left(\frac{x_{\rm PDG} - f x_{\rm seen}}{\overline{\sigma}_{\rm seen}} \right)^2$$

   where the following values were used,

	$x_{\rm PDG}$	$\overline{\sigma}_{\rm seen}$
total E	1876.54	36
π^0	134.96	8.4
η	547.45	19

   and the $x_{\rm seen}$ were measured for each run period. The values of f varied from run to run, but ranged from 0.994 to 1.013. See table 7.2 for a list.

3. The scalings of the errors is the hardest part and requires a certain art. The desired outcome is to have a flat confidence level and to have normal Gaussian pulls, i.e. with mean zero and width one. This is usually impossible to achieve in practice. The flatness of the confidence level is given first priority, and having equally wide pull distributions is second priority. With a few iterations, the confidence level

[1] `scale/scaling.txt` for a history and all the actual scaling values used.

Run Period	E Scale	$\sigma(\phi)$ Scale	$\sigma(\theta)$ Scale	$\sigma(\sqrt{E})$ Scale	Neutral Vertex (cm)
M.C.	1.0080	1.05	1.05	1.05	(0.0,0.0,0.0)
dec89	1.0008	1.02	1.17	1.02	(0.0,0.0,-0.13)
jun90	0.9940	1.01	1.13	1.05	(0.0,0.0,0.050)
jul90	0.9962	0.95	1.20	1.07	(0.0,0.0,0.131)
oct90	1.0102	1.00	1.03	1.00	(0.0,-0.4,-0.21)
nov90	1.0102	0.96	1.06	1.01	(0.0,-0.4,-0.30)
may91	1.0102	0.98	1.18	1.03	(0.0,0.0,-0.79)
jun91	1.0112	0.86	0.91	0.86	(0.0,0.0,0.29)
aug91	1.0122	0.94	1.78	0.98	(0.0,0.0,-0.77)
oct93	1.0120	1.02	1.09	1.02	(0.0,0.0,0.18)
jun94	1.0128	1.01	1.10	1.00	(0.0,0.0,0.20)

Table 7.1: The scalings used for the different run periods and Monte Carlo data sets.

cut	LBL	$\pi^0\eta\eta$	$\pi^0\pi^0\eta$	$\pi^0\pi^0\pi^0$	$\eta(\omega\to\eta\gamma)$	$\eta(\omega\to\pi^0\gamma)$	$\pi^0(\omega\to\pi^0\gamma)$	$\pi^0\pi^0$	$\eta\eta$	$\pi^0\pi^0\gamma$	$\eta\eta\gamma$	$\eta\pi^0\gamma$
Event in	1128570	109198	99961	87248	6754	355233	99963	4264	5885	29392	97205	30827
$5\gamma \ni E_\gamma > 20$	748441	71735	57461	47438	5482	315308	65543	3864	5249	26432	86458	27533
KF(5γ)	616155	50863	41378	35604	4911	287805	53098	3638	4779	24478	78190	25252
KF($\eta\eta\gamma$)	113546	28947	10017	3791	4755	91924	7080	94	3345	2824	75160	7880
KF($\eta\pi^0\gamma$)	369689	15986	33994	14765	1440	279531	23374	387	2707	10968	21672	24531
KF($\pi^0\pi^0\gamma$)	380479	1779	7117	34528	87	25930	51645	3450	124	23893	1559	2300
no fit	32119	13827	4280	905	134	7029	1144	170	1234	452	2436	615
ambig.	237934	9150	12943	15093	1424	108903	23820	395	2546	11129	21283	9402
Only $\eta\eta\gamma$	5763	20430	389	31	3334	644	15	8	806	10	53912	50
Only $\eta\pi^0\gamma$	136042	6893	21129	133	18	170639	268	7	162	112	532	15130
Only $\pi^0\pi^0\gamma$	204297	563	2637	19442	1	590	27851	3058	31	12775	27	55

Table 7.2: The event counts during the second pass on the data(kinematic fit)

can be made very flat above 0.2 and the Gaussian widths are typically 1.0 to 1.05 for the ϕ and $\sqrt{E}$ and 1.15 for the θ pull.

It is very difficult to modify the widths of certain pulls, rather than all three of them. However, in an attempt to compensate this, the θ errors were scaled higher (typically 10%) than the other errors.

The final tuning of the overage scaling was done by selecting "real" 5-gamma events, rather than all 5-gamma events which include background from 6-gamma events. Because the relative background is lowest along the ω bands in the corresponding Dalitz plots, "real" events were those along the bands, from 760 MeV to 800 MeV for all three event groups ($\eta\eta\gamma$,$\eta\pi^0\gamma$,$\pi^0\pi^0\gamma$). The $\eta\pi^0\gamma$ and $\pi^0\pi^0\gamma$ event groups totally dominate the "real"event sample, because of the strength of the $\omega\to\pi^0\gamma$ decay. The 4C confidence level was histogrammed in 8 bins from 0.20 to 1.00, and fitted with a linear function $y = a + bx$. The total error scaling was modified until $b = 0$ (within 0.25 sigma).

This was repeated for all ten data runs, and for the "real" Monte-Carlo sets, $\eta(\omega\to\eta\gamma)$, $\eta(\omega\to\pi^0\gamma)$, $\pi^0(\omega\to\pi^0\gamma)$, and $\eta((\omega/\rho^0)\to\eta\gamma)$.

It is more important that the Monte Carlo match the data in the confidence level and pulls than to have absolutely perfect pulls in all cases, and hopefully the former has been accomplished.

7.3 Software

Along with the software mention in the skim chapter, the totally new KinFit class was written and used for the kinematic fitting. Please see the KinFit chapter later in this document for a description.

The efficiency of the Kinematic Fit is shown in figure 7.4 as a function of run number. The efficiency is defined as the number of events accepted by the kinematic fit divided by the total events accepted by the first skim pass. The stability of the data is shown across 9 run periods from 1989 to 1994.

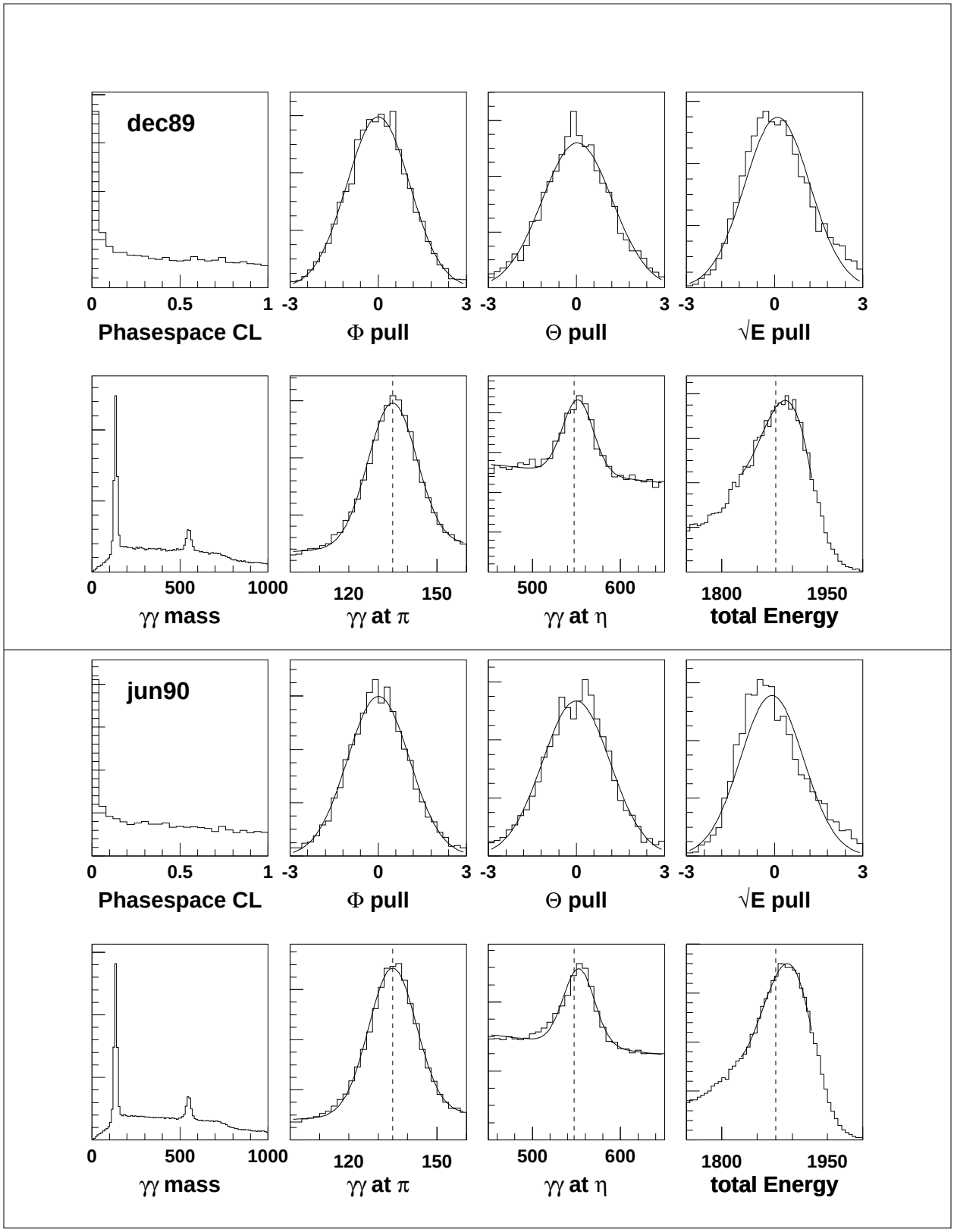

Figure 7.1: The pulls and calibration peaks for various run periods (this page and the following 5 pages).

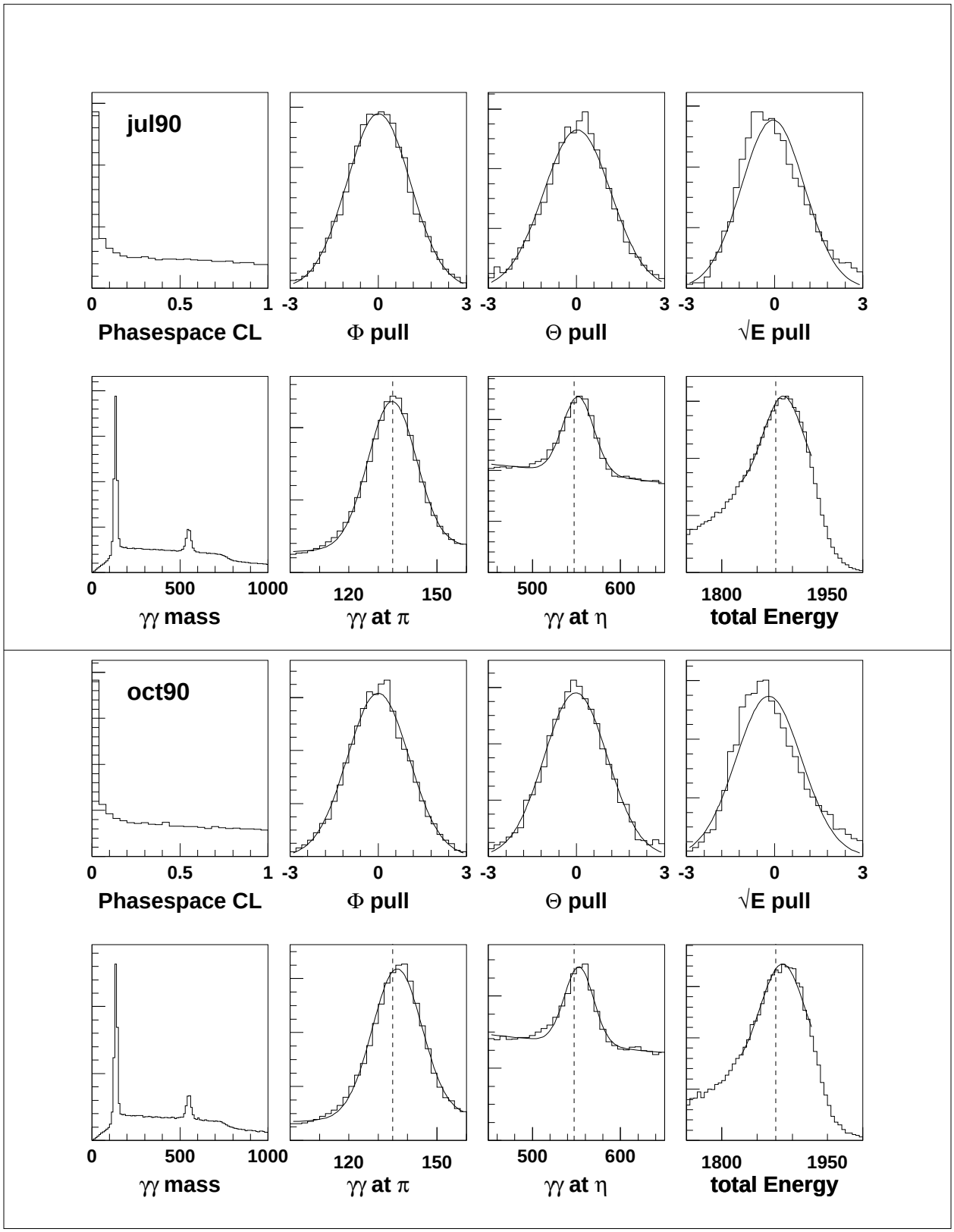
jul90
0
0.5
1
Phasespace CL
-3
0
3
Φ pull
-3
0
3
Θ pull
-3
0
3
√E pull
0
500
1000
γγ mass
120
150
γγ at π
500
600
γγ at η
1800
1950
total Energy
oct90
0
0.5
1
Phasespace CL
-3
0
3
Φ pull
-3
0
3
Θ pull
-3
0
3
√E pull
0
500
1000
γγ mass
120
150
γγ at π
500
600
γγ at η
1800
1950
total Energy

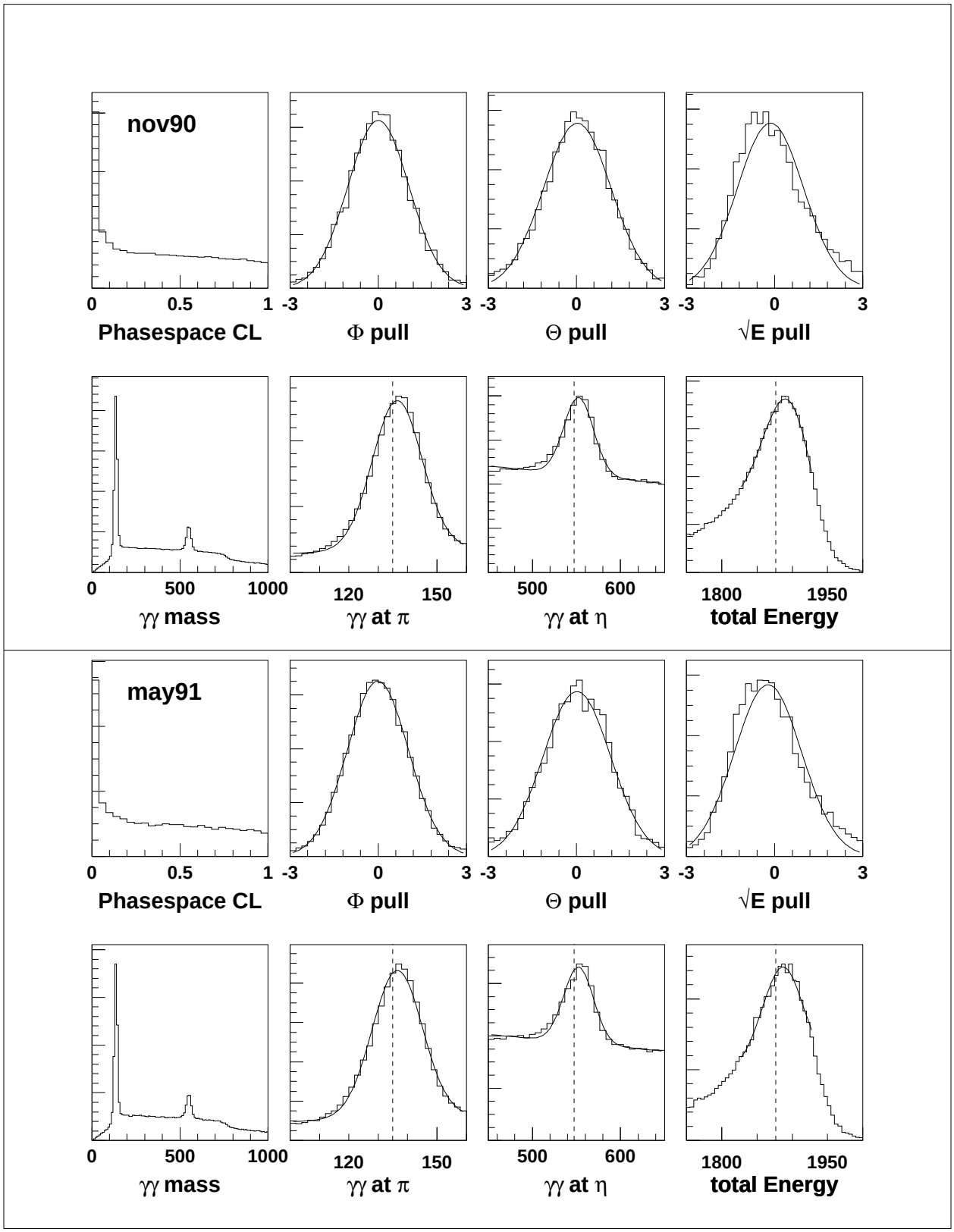
nov90
0
0.5
1
Phasespace CL
-3
0
3
Φ pull
-3
0
3
Θ pull
-3
0
3
√E pull
0
500
1000
γγ mass
120
150
γγ at π
500
600
γγ at η
1800
1950
total Energy
may91
0
0.5
1
Phasespace CL
-3
0
3
Φ pull
-3
0
3
Θ pull
-3
0
3
√E pull
0
500
1000
γγ mass
120
150
γγ at π
500
600
γγ at η
1800
1950
total Energy

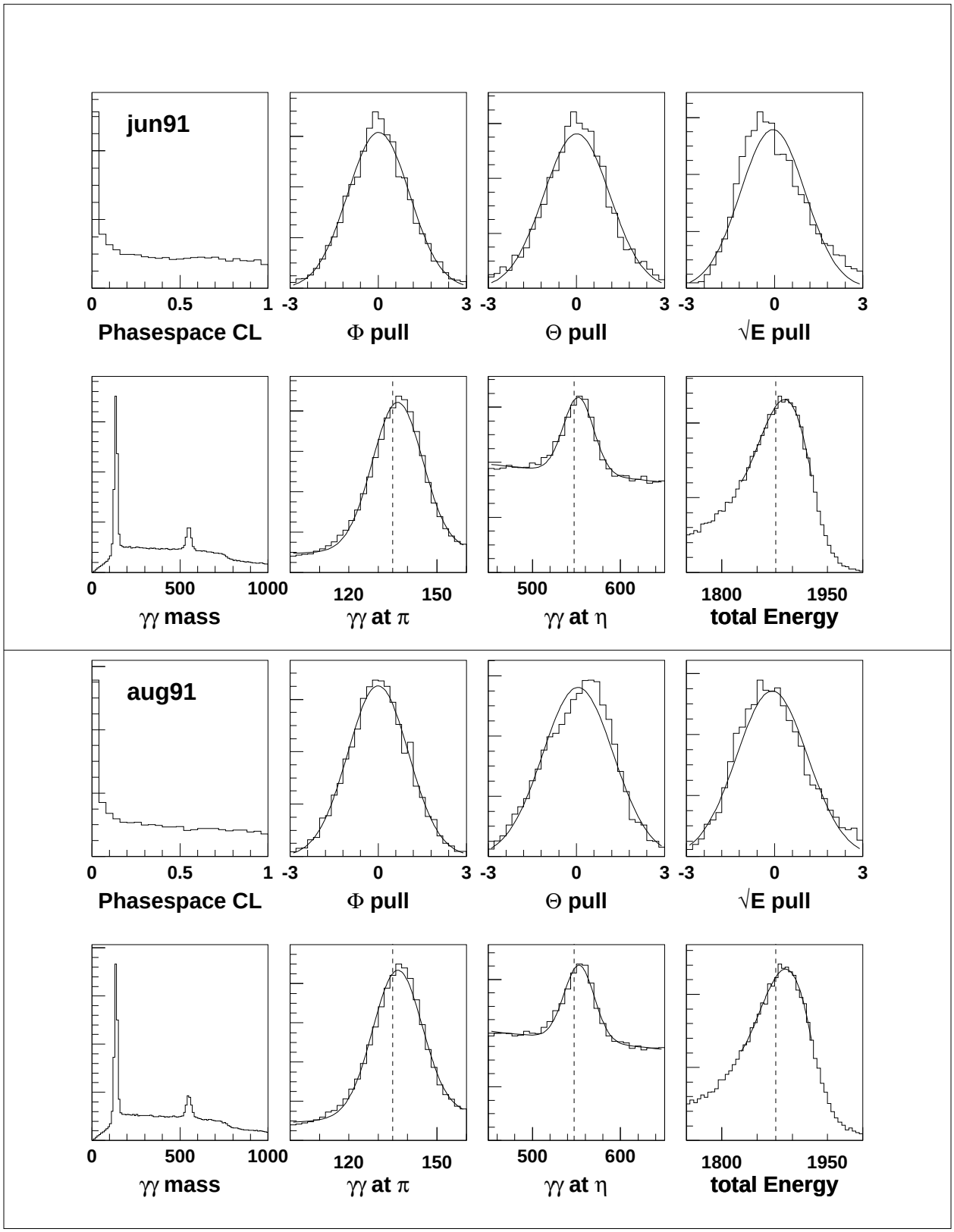
jun91
0
0.5
1
Phasespace CL
-3
0
3
Φ pull
-3
0
3
Θ pull
-3
0
3
√E pull
0
500
1000
γγ mass
120
150
γγ at π
500
600
γγ at η
1800
1950
total Energy
aug91
0
0.5
1
Phasespace CL
-3
0
3
Φ pull
-3
0
3
Θ pull
-3
0
3
√E pull
0
500
1000
γγ mass
120
150
γγ at π
500
600
γγ at η
1800
1950
total Energy

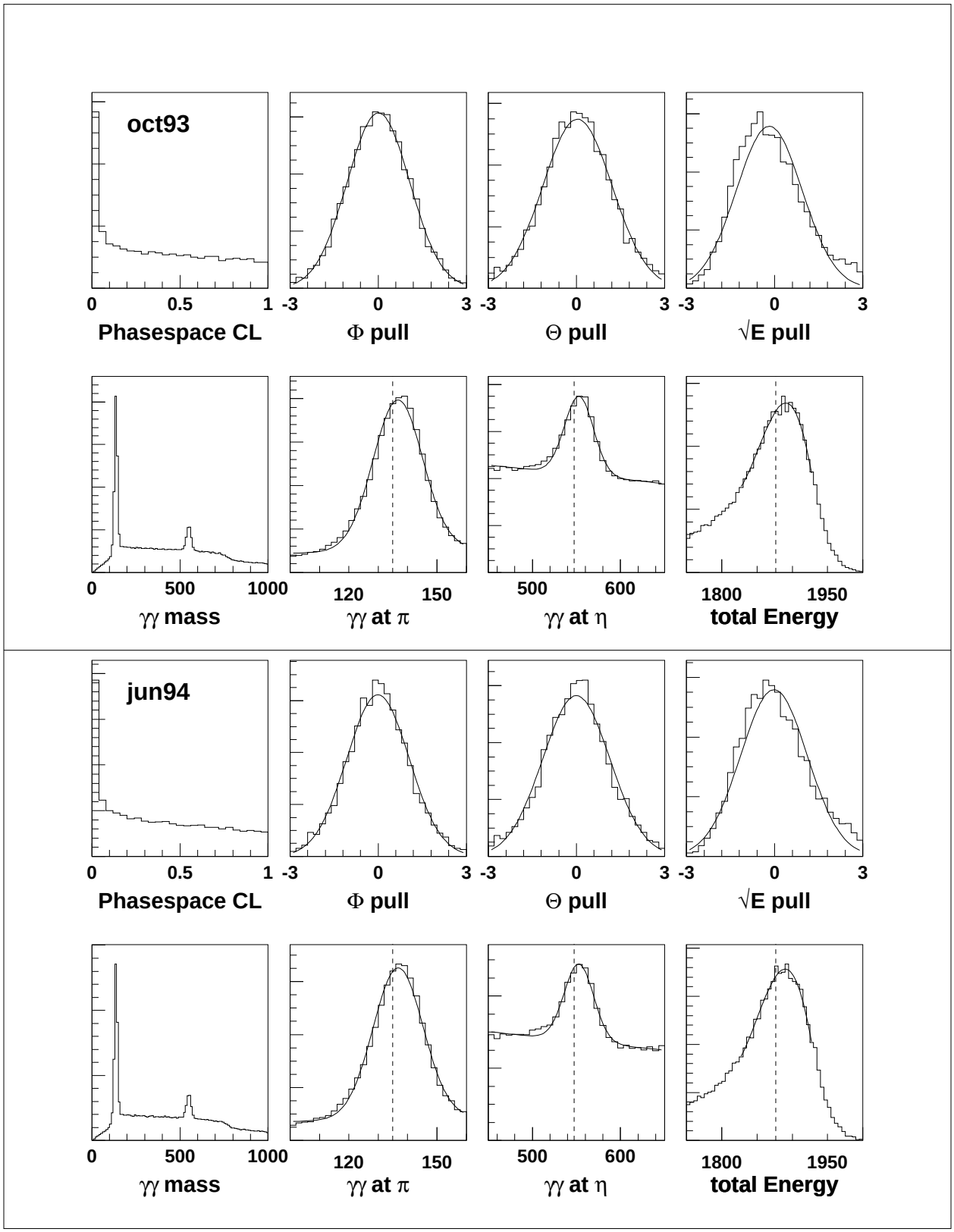
oct93
0
0.5
1
Phasespace CL
-3
0
3
Φ pull
-3
0
3
Θ pull
-3
0
3
√E pull
0
500
1000
γγ mass
120
150
γγ at π
500
600
γγ at η
1800
1950
total Energy
jun94
0
0.5
1
Phasespace CL
-3
0
3
Φ pull
-3
0
3
Θ pull
-3
0
3
√E pull
0
500
1000
γγ mass
120
150
γγ at π
500
600
γγ at η
1800
1950
total Energy

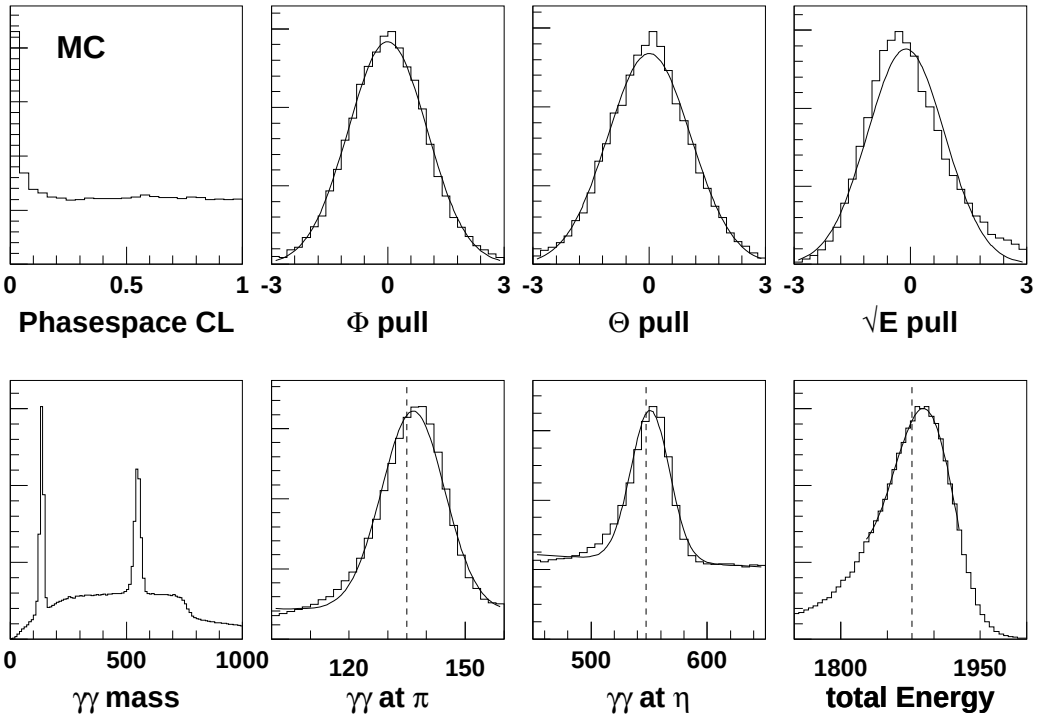
MC
0
0.5
1
Phasespace CL
-3
0
3
Φ pull
-3
0
3
Θ pull
-3
0
3
√E pull
0
500
1000
γγ mass
120
150
γγ at π
500
600
γγ at η
1800
1950
total Energy

7.4 Erratum

We have discovered two small problems in our final data set after the analysis was completed. Neither problem has a significant impact on the final value. The problems appear to be a result of changing the PED reconstruction thresholds, since neither problem existed before. These problems were not discovered until this technical report was written and new figures produced. Because the problems are minor, it was decided that a reanalysis was not necessary.

The first problem is that the Dec89 run period has drop-outs in the kinematic fit efficiency, where the average acceptance drops from roughly 60% to 20% for several runs (see figure 7.4). The total number of events in these low efficiency runs is 38178 out 1127570, or 3.4%. Because the final answer is expressed as a ratio of rare branching ratio to reference branching ratio, this small effect is cancelled out, resulting in no change to the final answer.

The second problem is that all of the calibration peaks have shifted slightly upward on the order of 1-2% (see figure 7.1). Before the change in thresholds, all of the peaks were well centered on the desired π^0 mass, η mass and $p\overline{p}$ mass. However again, this problem is doubly cancelled in the final result. First, the energy shift appears equally in both the data and the Monte Carlo, so it is cancelled out by the efficiency calculation. Second, the final answer is a ratio of two measurements, so it is cancelled out again.

Because the final measurement is quoted with 40% errors, these problems are not significant.

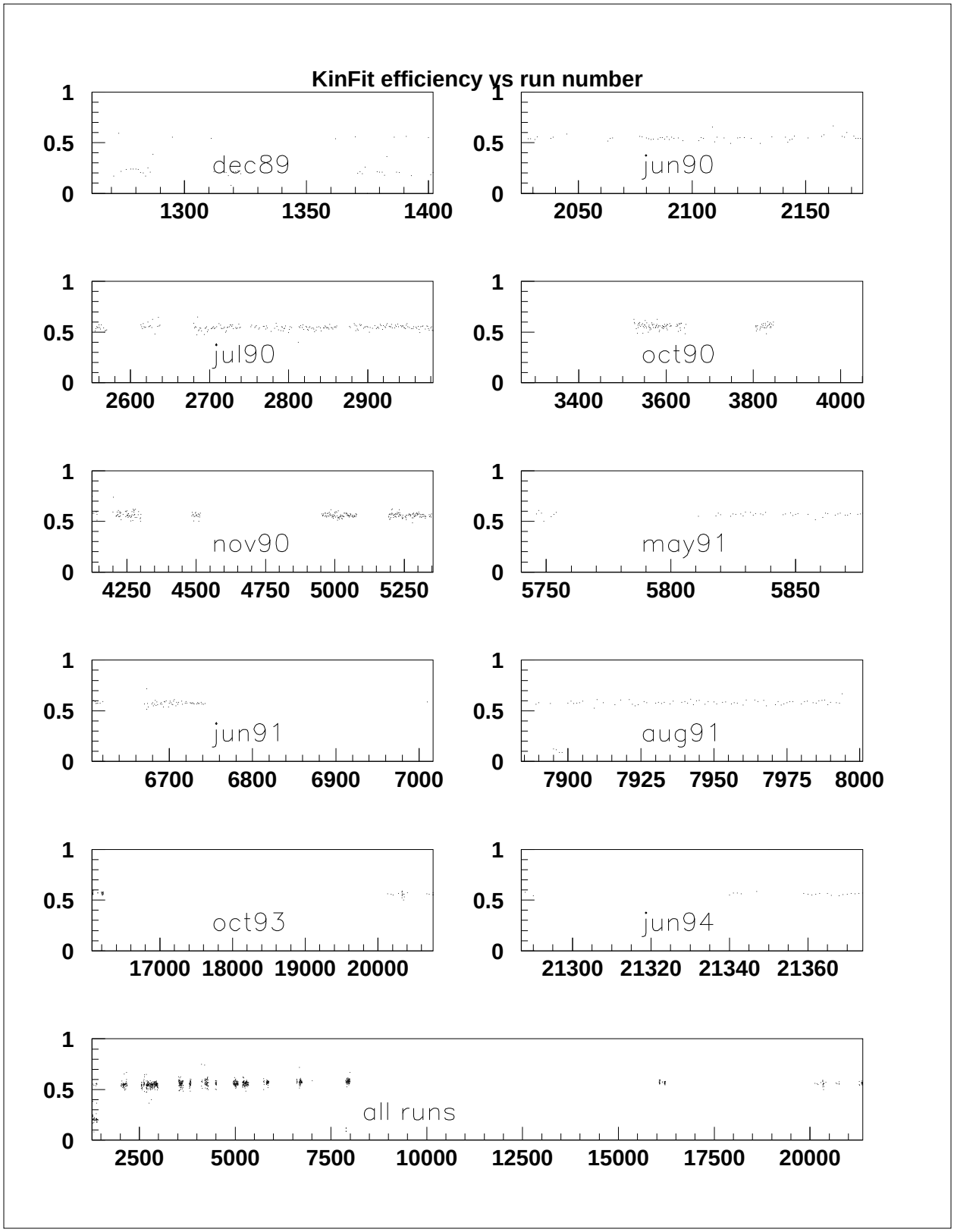

Figure 7.2: Efficiency of the KinFit as a function of run period. Efficiency is defined as the ratio of KinFit passing phase space events divided by the number of 5-γ events.

Chapter 8

Final cuts

The cuts given in previous chapters were chosen to select out the desired signal. In this chapter, we describe the cuts that were used to remove the remaining background.

8.1 Confidence level of KinFit to $\eta\eta\gamma$ Hypothesis

The confidence level is calculated as the probability that the kinematic fit could be "better" by having a smaller χ^2, or

$$\mathrm{CL}(\chi^2) = \int_{\chi^2}^{\infty} f(z;n)dz$$

$$f(z;n) = \frac{z^{n/2-1}e^{-z/2}}{2^{n/2}\Gamma(n/2)}$$

where $f(z;n)$ is a probability density function for a χ^2 distribution for n degrees of freedom. For events that are distributed around the hypothetical perfect value in a normal distribution (real signal events), the confidence level is flat from 0 to 100%. For events with a random or flat χ^2, the confidence level will not be flat, and will be bunched up near 0.

We require all three groups to have a confidence level above the 10 th percentile. By definition, this should only discard 10% of the signal, but a much larger fraction of the background. Note that this assumption depends on the confidence level being flat. If it is not flat because of some wrong assumptions about error estimates, a cut at the 10 th percentile will not leave one with exactly 90%, but a substantially different amount.

In figure 8.1 are the confidence levels for the important channels (data and MC) for the three groups, $\eta\eta\gamma$, $\eta\pi^0\gamma$ and $\pi^0\pi^0\gamma$. The signal channels are reasonably flat, while the backgrounds fall quickly with increasing confidence level.

8.2 Removal of "cross" π^0's

In all three groups, there is a probability that the kinematic fit selects the wrong assignment of γ's to intermediate particles because the best fit was from an incorrect assignment with an accidentally lower χ^2. This can happen within a particular group's assignment, or between two groups. For instance, the $\pi^0(\omega\rightarrow\pi^0\gamma)$ decay could be assigned to the $\pi^0\pi^0\gamma$ group, but the individual assignments of the γ's to the π^0's could be wrong. This case is not particularly troublesome. However, the $\eta(\omega\rightarrow\pi^0\gamma)$ decay could be assigned to the $\eta\eta\gamma$ group with disastrous results, if it fails the $\pi^0\eta\gamma$ fit and it contains an accidental fake η within the $\omega\rightarrow 3\gamma$. The reason this is a problem is because the $\eta(\omega\rightarrow\pi^0\gamma)$ channel is two orders of magnitude more intense than the $\eta(\omega\rightarrow\eta\gamma)$ channel, and the fake η appears to come from an ω decay, thus faking the desired signal, unlike other non-resonant backgrounds.

To remove this second type of accidental assignment, it is critical to check pairwise combinations of particles after the kinematic fit. The most likely wrongly assigned γ is the unpaired "radiated" γ. Thus we pair the radiated γ with each of the other four γ's, and take the pair whose invariant mass is closest to 135 MeV. This pair is called the "cross-π^0" or XPI for short. Normally, the measured invariant mass of a π^0

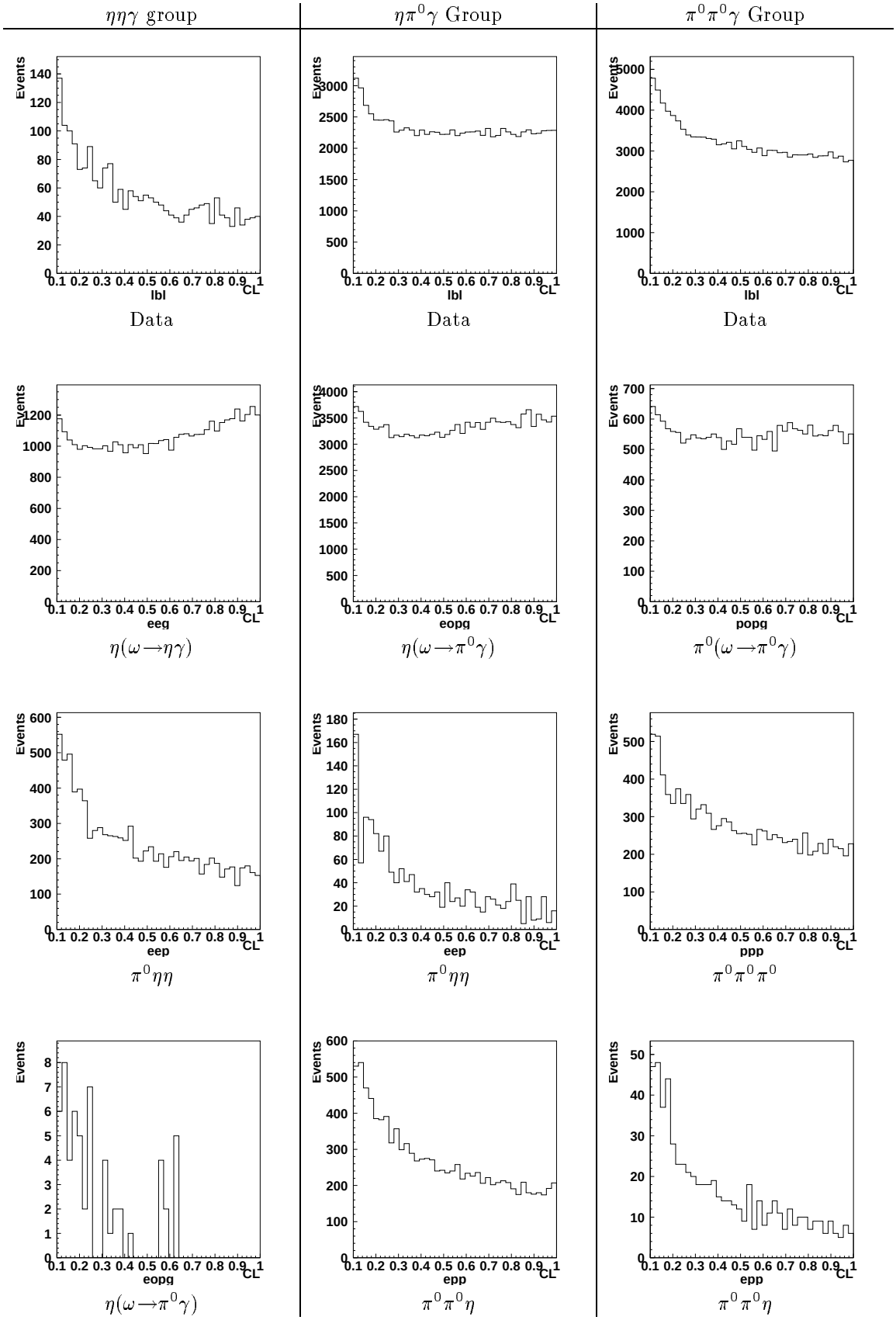

Figure 8.1: Confidence levels for data and selected Monte Carlo sets, for each of the three groups, $\eta\eta\gamma$ (Left column), $\eta\pi^0\gamma$(center column) and $\pi^0\pi^0\gamma$(right column).

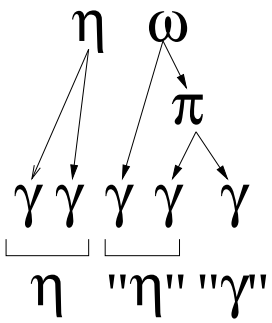

Figure 8.2: One way that the $\eta(\omega \to \pi^0\gamma)$ channel can slip into the $\eta\eta\gamma$ group. Note that the fake "η" and fake "γ" form a real ω, so this channel is particularly important to remove completely, lest it contribute to the desired signal's peak. This background can be removed with the XPI cut.

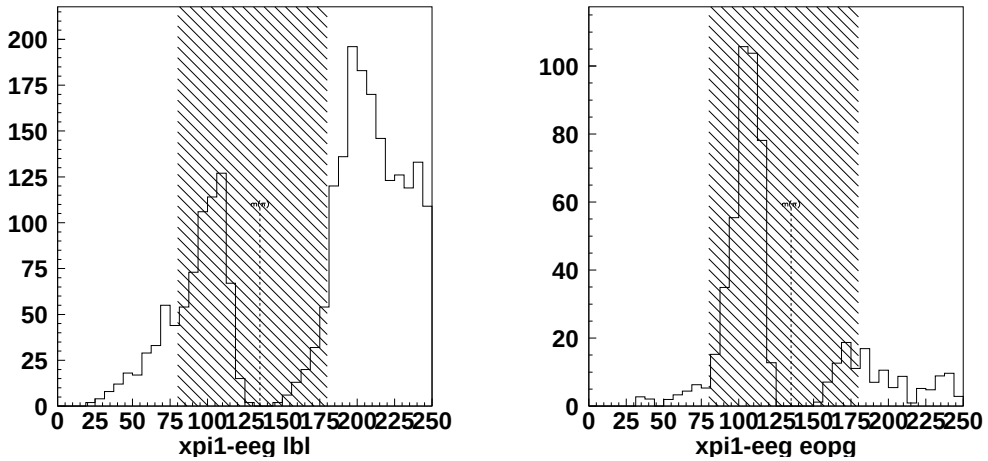

Figure 8.3: The XPI distribution for data (left) and $\eta(\omega \to \pi^0\gamma)$ MC (right). Events within the gray region are discarded.

does not vary more than 10 MeV from 135 MeV. However, the tails of the mass distribution can extend to 50 MeV and beyond because of detector systematics. Such a poorly measured π^0 will fail a kinematic fit, and thus not be identified as a π^0. To remove this type of event, we cut all events with an XPI mass between 85 and 195 MeV. See figure 8.3.

$$85 < \texttt{xpi1} < 185 \text{ MeV}.$$

8.3 Unused cuts

We experimented with other cut variables. One technique looked at subthreshold γ's as potential real γ's and calculated an invariant mass between each soft γ and the radiated γ. This technique showed promise, but unfortunately was too dependent on the low energy details of the Monte Carlo to be reliable for calculating correct efficiencies. Also, the slight SNR gain from this cut was essentially balanced by slight decrease in signal statistics, resulting in no net gain in overall precision.

Another technique was used to look for "merged" γ's, that is two γ's from two different mesons merging because they accidentally hit the same cluster of crystals in the calorimeter. Given three "γ's", we hypothesis that one is a merged γ, and break it into two pieces, with fractional energy x and $1-x$. We then solve for x such that the four γ's came from $\pi^0 \rightarrow \gamma\gamma$and $\pi^0 \rightarrow \gamma\gamma$. It was expected that there would be some identifying signature in a distribution of x or $xE\gamma$, but no clear structure was observed.

The final histograms used in the fit are shown in figure 8.4.

Cut set	$\eta((\omega/\rho^0)\to\eta\gamma)$	$\pi^0\pi^0\eta$	$\pi^0\eta\eta$	$\eta(\omega\to\pi^0\gamma)$	data	$\eta(\omega\to\eta\gamma)$	$\eta\eta\gamma$	$\eta\eta$
1	53912	389	20430	644	5763	0	53912	806
2	42653	96	9788	59	2260	0	42653	241
3	51990	328	19346	244	5039	0	51990	493
5	41461	90	9542	32	2142	2695	41461	115
21	20676	282	13503	236	3725	0	20676	460
22	14249	23	3218	8	704	0	14249	19
23	17065	23	2625	0	610	0	17065	14
60	42653	96	9788	59	2260	0	42653	241
61	42651	95	9785	54	2255	0	42651	231
62	41961	92	9650	35	2183	0	41961	129
63	38879	76	9000	25	1988	0	38879	56
64	34957	53	8023	21	1765	0	34957	18

```
ASSIGN XCL  (chisq<10.66)
ASSIGN XPI1 ((xpi1<80)||(xpi1>180))
ASSIGN XPI2 (xpi2<100)

1    1
2    XCL
3    XPI1
5    XCL && XPI1

21                chisq>6.90 && XPI2 && XPI1
22   6.90>chisq && chisq>4.14 && XPI2 && XPI1
23   4.14>chisq               && XPI2 && XPI1

60   !(130<xpi1 && xpi1<140) && XCL && XPI2
61   !(110<xpi1 && xpi1<160) && XCL && XPI2
62   !( 90<xpi1 && xpi1<180) && XCL && XPI2
63   !( 70<xpi1 && xpi1<200) && XCL && XPI2
64   !( 50<xpi1 && xpi1<220) && XCL && XPI2
```

Table 8.1: Event counts for the $\eta\eta\gamma$ group, and the cut set definitions.

Cut set	$\pi^0((\omega/\rho^0)\to\eta\gamma)$	$\pi^0\pi^0\eta$	$\pi^0\eta\eta$	$\eta(\omega\to\pi^0\gamma)$	data	$\eta\pi^0\gamma$
1	15130	21129	6893	170649	136042	15130
2	11907	10889	1540	133871	93350	11907
3	12705	17142	6147	153338	117558	12705
4	13967	18175	6763	166248	127362	13967
5	10013	9044	1410	120861	82349	10013
6	11019	9780	1514	130677	88954	11019
7	12149	15392	6084	150096	112735	12149
8	9592	8379	1398	118396	79588	9592
21	4575	12418	5807	52560	55250	4575
22	2534	2918	458	28410	20760	2534
23	2578	2211	253	28742	20170	2578
24	2686	1931	215	30256	19928	2686
25	2757	1651	160	30681	19934	2757
32	2534	2918	458	28410	20760	2534
33	2578	2211	253	28742	20170	2578
34	2686	1931	215	30256	19928	2686
35	2757	1651	160	30681	19934	2757

```
ASSIGN XCL  (chisq<10.66)
ASSIGN CHISQ  (chisq)
ASSIGN XPI1 ((xpi1<80)||(xpi1>180))
ASSIGN XFPG (fpg>200)

1  1
2  XCL
3  XPI1
4  XFPG
5  XCL && XPI1
6  XCL && XFPG
7  XPI1 && XFPG
8  XPI1 && XCL && XFPG

21               CHISQ>8.55
22 8.55>CHISQ && CHISQ>6.21
23 6.21>CHISQ && CHISQ>4.56
24 4.56>CHISQ && CHISQ>3.06
25 3.06>CHISQ

32 8.55>CHISQ && CHISQ>6.21
33 6.21>CHISQ && CHISQ>4.56
34 4.56>CHISQ && CHISQ>3.06
35 3.06>CHISQ
```

Table 8.2: Event counts for the $\eta\pi^0\gamma$ group, and the cut set definitions

Cut set	$\pi^0\pi^0\eta$	$\pi^0\pi^0$	$\pi^0\eta\eta$	$\pi^0\pi^0\pi^0$	$\eta(\omega\rightarrow\pi^0\gamma)$	data	$\pi^0\pi^0\gamma$	$\pi^0(\omega\rightarrow\pi^0\gamma)$
1	2637	3058	563	19442	590	204297	12775	27851
2	640	2211	180	11213	128	128838	10165	22066
3	2130	1721	535	14792	523	155130	10481	22785
5	502	1301	173	8777	116	100369	8316	18104
21	2191	1177	415	10210	502	94767	3819	8487
22	182	535	63	2862	48	30470	2159	4783
23	110	496	25	2360	18	27777	2226	4747
24	91	450	29	2120	14	26061	2293	4957
25	63	400	31	1890	8	25222	2278	4877

```
ASSIGN XCL  (chisq<10.66)
ASSIGN XPI1 ((xpi1<80)||(xpi1>180))
ASSIGN XFPG (fpg>200)

1  1
2  XCL
3  XPI1
4  XFPG
5  XPI1 && XCL
6  XCL && XFPG
7  XPI1 && XFPG
8  XPI1 && XCL && XFPG

21               chisq>8.55
22 8.55>chisq && chisq>6.21
23 6.21>chisq && chisq>4.56
24 4.56>chisq && chisq>3.06
25 3.06>chisq
```

Table 8.3: Event counts for the $\pi^0\pi^0\gamma$ group

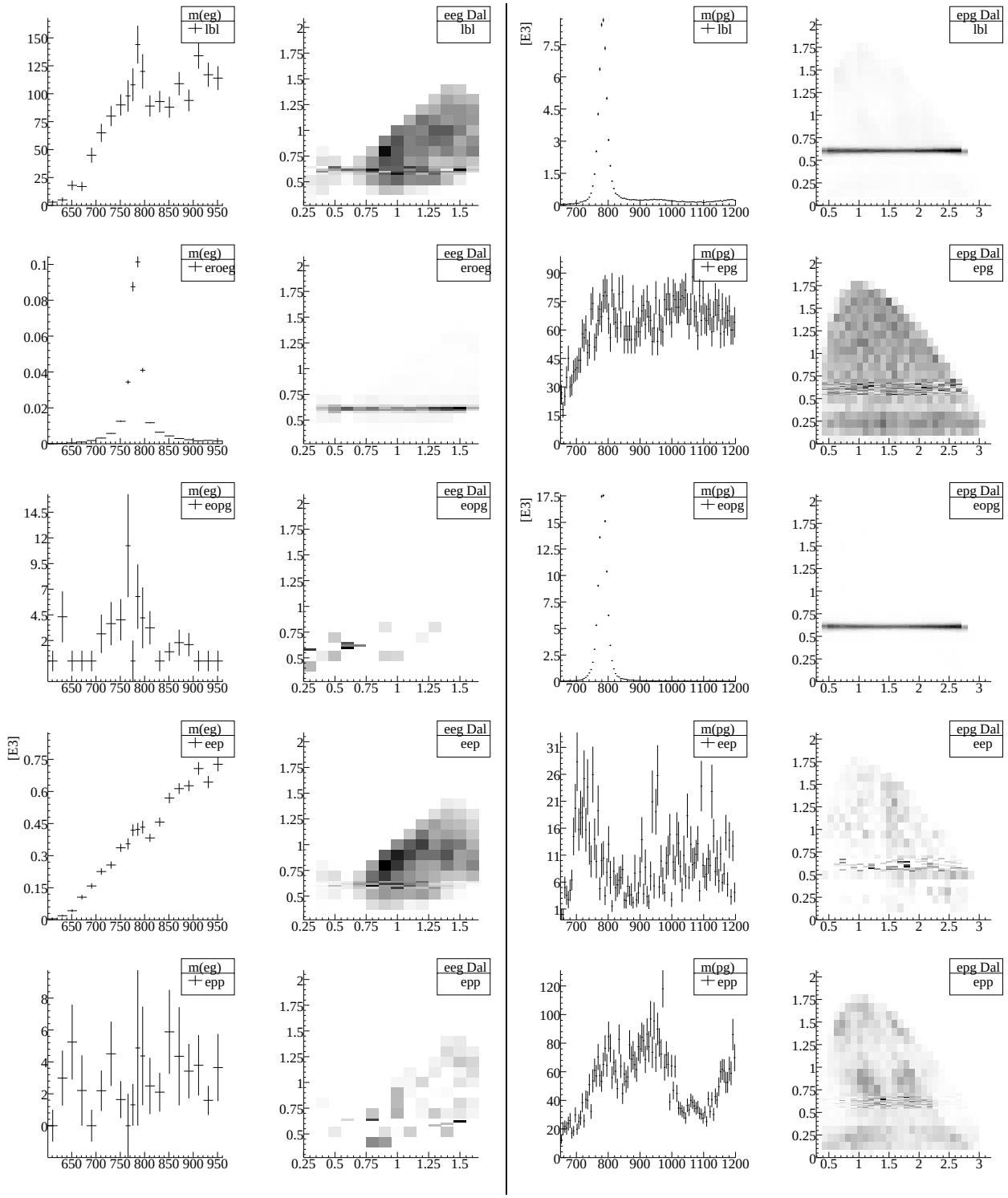

Figure 8.4: The left two columns are from the $\eta\eta\gamma$ group, while the right two columns are from the $\eta\pi^0\gamma$group. Each row represents a different MC set or data set. "lbl" refers to the real data, which is the first row. (The labels are described in table 5.2). The columns are either 1D projections or the full Dalitz plot. The 1D vertical scales are arbitrary in all cases except for the real data.

Chapter 9

Fits

9.1 Introduction

Because of the low statistics and high backgrounds involved, the details of fitting procedure is critical to the success of this measurement. Because available histogramming and fitting packages were not suitable for this task (e.g Paw), a custom histogramming package and a custom likelihood function were employed. Details of these packages are given in the appendix.

As well as depending on the fitting procedure, the results also depend on which backgrounds are included in the fit. All known backgrounds were included in the fits; however, there is evidence for other previously unmeasured backgrounds. Without further study, we fit the data with and without these additional unknown backgrounds and combine the two results. We also present the results of the fits with the unknown backgrounds as first measurements of these channels.

We use the term "χ^2" rather loosely throughout this chapter, when it would be more exact to say "twice the minus log-likelihood". The values given are twice the negative log-likelihood, which is equivalent to χ^2 for error estimation.

9.2 Generating the histograms

The final cuts were cut set "5", as defined in tables 8.1, 8.2 and 8.3. To summarize, cut "5" is a 10% confidence level cut and the XPI1 cut which removes events where the kinematic fit missed a π^0 combination. All of the scans in section 9.4 used these cuts.

The histograms used for the fits were two dimensional Dalitz plots, where the axes are the squared invariant masses of pairwise combinations of the final particles. For example, in the $\eta\eta\gamma$ group, the axes are $m^2(\eta_1\gamma)$ vs $m^2(\eta_2\gamma)$, where the subscripts denote an arbitrary assignment of the η's, and so each event can be entered twice. Because of this symmetry, we need only fit half of the data plot. The $\pi^0\pi^0\gamma$ group has the equivalent assignment. The $\eta\pi^0\gamma$ group, because of distinguishable particles, is plotted as $m^2(\pi^0\gamma)$ vs $m^2(\eta\gamma)$, and the whole Dalitz plot is fitted.

To save unnecessary computation and to keep the events per bin high, the binning size was chosen to be large in regions were only background was expected. In regions where an ω signal is expected the binning is much smaller.

Real data events are entered into the histograms with a weight of 1. Monte Carlo channels flat in phase space are also weighted with 1, including $\eta\eta$, $\pi^0\pi^0$ $\eta\eta\gamma$, $\eta\pi^0\gamma$ and $\eta\pi^0\gamma$. Monte Carlo channels with a decaying ω are weighted by a unity-normalized Jackson-Godfried decay angle distribution (see chapter 5). Monte Carlo channels of three pseudoscalars ($\pi^0\eta\eta$,$\pi^0\pi^0\eta$ and $\pi^0\pi^0\pi^0$) are weighted by a unity-normalized measured Dalitz plot. Monte Carlo channels of mixed ω/ρ^0 decays into $\eta\gamma$ are weighted by a special amplitude squared. This intensity is not normalized to unity, but is an absolute branching ratio.

9.3 Fitting the histograms

The data histogram is fitted against the linear sum of selected Monte Carlo histograms. The selection criteria was to include a certain MC channel if its expected contribution was at least 1% to the events in the group

Group	$\eta\eta\gamma$	$\eta\pi^0\gamma$	$\eta(\omega\to\pi^0\gamma)$	$\pi^0(\omega\to\pi^0\gamma)$	$\pi^0\eta\eta$	$\pi^0\pi^0\eta$	$\pi^0\pi^0\pi^0$	$\eta\eta$	$\pi^0\pi^0$
$\eta\eta\gamma$	*/1		BW A		Dal	Dal		1	
$\eta\pi^0\gamma$		*/1	BW A			Dal			
$\pi^0\pi^0\gamma$				BW A			Dal		1

Table 9.1: MC sets and their weightings. * = special ω/ρ^0 amplitude (described in the text), BW = ω Breit-Wigner, A = decay angle, Dal = Dalitz Plot, 1 = flat weight.

or if it was expected to affect the signal in a special way. The MC channels used (and their weighting mechanism) in each group are given in table9.1. Note that the $\eta\eta\gamma$ and $\eta\pi^0\gamma$ channels are doubly used, as an inherently flat phase channel in their own right and as the phase space for the ω/ρ^0 decay channels. In the former case the events are unweighted, while in the second they are weighted by the special intensity given in section 5.6. The channels are then summed incoherently.

The goodness of fit is determined by a special log-likelihood function that takes into account the Poisson nature of both the data and the Monte Carlo. The traditional log-likelihood for Poisson processes is not acceptable because it assumes that the theory is exact. See appendix 10.3 for a description of this special function.

Per bin i, the theoretical intensity is

$$N_i^{\text{theory}}{}_i = \sum_j \alpha_j w_{ij} N_{ij}$$

where N_{ij} stands for the number of actual Monte Carlo events in the ith bin due to the j^{th} Monte Carlo dataset. The w_{ij} is the weight described above. The α_j is the net branching ratio and efficiency calculated below. The fit uses the integral-valued counts of N_{ij} for Poisson statistics, rather than the expected event count after weighting, branching ratio and efficiency factors are applied.

The value of α_j is seeded using the expected value based on PDG and CB branching ratio values and the total number of events.

Value	=	Formula	Description
α_j^0	=	$T * BR(j)/N_{MC}(j)$	initial value
T	=	$N_{data} * (1 - 0.036)/BR(0\text{ prong})$	number of equivalent $p\overline{p}$ annihilations with bad runs thrown away
N_{data}	=	20×10^6	number of triggered events
$BR(0\text{ prong})$	=	0.039 ± 0.003	0-prong fraction of $p\overline{p}$
$BR(j)$	=	-	$p\overline{p}$ BR for j^{th} MC set.
$N_{MC}(j)$	=	-	Number of generated MC events in j^{th} set.

For the unknown backgrounds, $\eta\eta\gamma$, $\eta\pi^0\gamma$ and $\pi^0\pi^0\gamma$, a reasonable guess was made for the initial values, but this is not important to the final value.

Because of low statistics for some channels, leaving that channel's intensity free in the fit made the fit unstable. Because of this, some channels were not allowed to vary in the fit. However, because the small contribution of these channels to the background, and even less to the signal, this is not seen as a source of additional error for the fit result of the signal.

By dividing the final value of α_j with the initial values, a comparison to previously measured values is directly available; a value of 1 confirms the previous value.

Because of the additional computation time needed for calculating the special intensity of the mixed ω/ρ^0 decay to $\eta\gamma$, this channel was not a free parameter of the fit. Rather, the branching ratios of BR($\omega\to\eta\gamma$) and BR($\rho^0\to\eta\gamma$) were scanned over a suitable range, and 2-D χ^2 surface was produced. This allows a visual check of the appropriate 1-sigma error limits for both branching ratios.

The fitting of each channels contribution is performed by using MINUIT [25] to minimize the negative log-likelihood while varying the free parameters. The fit error estimates were done using the MINOS algorithm.

9.4 Determination of $\omega\to\eta\gamma$ and $\rho^0\to\eta\gamma$

The decays $\omega\to\eta\gamma$ and $\rho^0\to\eta\gamma$ (and mixtures of the two) occur in the $\eta\eta\gamma$ and $\eta\pi^0\gamma$ groups. Because the ρ^0 is wide, it is difficult to measure in either group, and in fact this analysis gives little information on

the intensity of the ρ^0 decay. Also, the background in $\eta\pi^0\gamma$ is much larger than in $\eta\eta\gamma$. This makes any measurement (ω or ρ^0) in the $\eta\pi^0\gamma$ very poor. The only hope for a good measurement is $\omega\rightarrow\eta\gamma$ in the $\eta\eta\gamma$ group.

9.4.1 The dependence on interference parameters

The phenomenon of ρ^0/ω interference in this channel has not been studied in detail before. The description of the interference in chapter 5 is believed to be correct, but the incoherence of the $\eta(\omega\rightarrow\eta\gamma)$ and $\eta(\rho^0\rightarrow\eta\gamma)$ channels may be underestimated. Also, the effect of the ρ^0-ω mixing is not clearly obvious in these channels, and may not occur for unknown reasons. We show that the result is not very dependent on the model of the ω/ρ^0 intensity characterization. We produce a contour plot of χ^2 for each of the following three models.

1. Coherent interference between the ω and ρ^0 amplitudes and correcting for isospin mixing (type I).
2. Incoherent adding of the ω and ρ^0 intensities, but correcting each for isospin mixing (type II).
3. Incoherent adding of the ω and ρ^0 intensities, without any corrections due to isospin mixing (type III).

As we see, the difference between the three models is small, and thus for simplicity we use the default value for the isospin mixing parameter of $\delta = 2.5$ MeV and and let $\phi = 0$ which is predicted by the quark model. The numeric values are given in table 9.3 and the χ^2 contours are shown in figure 9.1.

It is clear that the result for ρ^0 is largely unstrained by the data. Because there is a slight correlation between ω and ρ^0 branching ratios, we fix the ρ^0 branching ratio to tabulated values to get the best estimate of BR($\omega\rightarrow\eta\gamma$).

9.4.2 The dependence on a 1 or 2 Dimensional histogram fit

The 2-dimension histogram or Dalitz plot contains all the kinematics of an event, and thus is the best to fit the true behavior of each background, but requires more statistics than a 1-dimensional projection. We fitted the data using both a 1-Dimensional binning (with relatively high statistics, about 20-120 events per bin), and using a 2-Dimensional Dalitz binning (with relatively low statistics, about 1-20 events per bin). By averaging all 1-Dimensional fits and averaging all 2-Dimensional fits, we see a 12% deviation from the average of all fits.

To measure the very weak $\pi^0((\omega/\rho^0)\rightarrow\eta\gamma)$ decay, we fitted both the 1-dimensional projection histogram as well as the 2-dimensional Dalitz plot. The results for $\pi^0((\omega/\rho^0)\rightarrow\eta\gamma)$ do not agree very well, indicating that the "peak" in the 1-dimensional histogram is perhaps fake.

9.4.3 The dependence on backgrounds

The 3 pseudoscalar backgrounds ($\pi^0\eta\eta$ and $\pi^0\pi^0\eta$) are known to exist, and their contributions can be fitted to the data. However, the fitted contributions are significantly larger than expected, from 20 to 50% larger.

Annihilation of $p\overline{p}$ usually proceeds through a two meson intermediate state. However, it can happen that the annihilation proceeds directly to a three particle final state, with two mesons and one photon. The fits to all three channels, $\eta\eta\gamma$, $\eta\pi^0\gamma$ and $\pi^0\pi^0\gamma$, improve if we assume that there exists a flat background channel that does not proceed through any intermediate resonances.

The evidence for these channels is three-fold. First, the χ^2 of the fits is greatly lower and a visual inspection of the fit quality greatly favors these new channels. Secondly, the fit values for the backgrounds channels $\pi^0\eta\eta$, $\pi^0\pi^0\eta$, and $\pi^0\pi^0\pi^0$ are too high without these new channels; in the case of $\pi^0\pi^0\eta$, the fit value is 50% too high.

Thirdly, the fitted values of these known background channels is not flat with respect to confidence level. The fit values increase significantly when the confidence level cut is increased. This indicates the existence of a background which does not drop off in confidence level as quickly as the 3 pseudoscalar backgrounds do. Remember that the 3 pseudoscalar backgrounds have "lost" a photon and therefore should not have a flat confidence level. However, these new channels are exactly the kinematic fit hypothesis and will have a flat confidence level distribution.

We believe that these three pieces of evidence favor the existence of these new channels. The branching ratios for these channels is given in table 9.2. The errors are estimated by taking the absolute limits of all of the fits tried. We set the lower error bar to include zero, because there is still the possibility that these

New Channel	BR($p\overline{p}\rightarrow$)	Replaces PS Bknd	— without — – new bkgd –		———— with new bkgd ————				NDF
					PS bkgd fixed		PS bkgd free		
			PS scale	χ^2	PS scale	χ^2	PS scale	χ^2	
$\eta\eta\gamma$	$1.9^{+1.6}_{-1.9} \times 10^{-5}$	$(\pi^0\eta\eta)$	1.27 ± 0.03	165	1.0000	134	$0.83^{+0.04}_{-0.09}$	129	133
$\eta\pi^0\gamma$	$2.5^{+0.5}_{-2.5} \times 10^{-4}$	$(\pi^0\pi^0\eta)$	1.56 ± 0.01	2704	1.0000	2601	$0.87^{+0.04}_{-0.01}$	2592	799
$\pi^0\pi^0\gamma$	$8.8^{+6.2}_{-8.8} \times 10^{-5}$	$(\pi^0\pi^0\pi^0)$	1.17 ± 0.02	1181	1.0000	1055	0.98 ± 0.02	1054	423

Table 9.2: New direct three body annihilation channels. Errors are approximate. The scaling of the pseudoscalar backgrounds (PS) are given for the cases with and without the new flat backgrounds. In the case "with", the pseudoscalar background scaling is set to 1.0000 to show the dependence on χ^2.

channels could be faked by subtle inaccuracies in the Monte Carlo and may not exist at all. If the Monte Carlo is wildly inaccurate, then it is prudent to include these fake channels to make up for it.

If we average the six fits using just $\pi^0\eta\eta$(background type A) and the average the six fits using both $\pi^0\eta\eta$ and $\eta\eta\gamma$(background type B), we see that the two disagree by 20%. We assign this variation to the systematic error.

9.4.4 The results of the data fits

To fit these very weak decays, the intensities $\omega\rightarrow\eta\gamma$ and $\rho^0\rightarrow\eta\gamma$ were scanned over a range of values and entered into the fit as fixed parameters. (The generation of the histograms is described in section 9.2, using cut "5")

All other parameters were either allowed to be free or fixed if their contribution was small. The χ^2 surface plots for each fit is shown in figures 9.1 and 9.2 (note contour lines are at $\Delta\chi = 1$, or approximately 1-sigma intervals.) The minima are given in table 9.3.

Because most of the fit results for BR($\rho^0\rightarrow\eta\gamma$) (weakly) converged to values more than four times published values (but with very large errors), we constrained BR($\rho^0\rightarrow\eta\gamma$)/table=1.0 for those results, indicated by "–" in the table.

9.5 Stability and Consistency Checks

To check the stability of the fit and systematic effects of the cuts, especially on the reference decay $\omega\rightarrow\pi^0\gamma$ in the $\eta\pi^0\gamma$ and $\pi^0\pi^0\gamma$ groups, all combinations of cuts were tried and the results are given in tables 9.4, 9.5 and 9.6. The projections and the dalitz plots were fitted in separate trials, to verify the robustness of the fit.

Many different variations of the fits were done to check for systematic errors. The fit results of these variations are shown in figures 9.4, 9.5 and 9.6. The numerical values are in tables 9.4, 9.5 and 9.6. The description of the numbered variations is described below. The cut set definitions can be found in tables 8.1 8.2 and 8.3 .

9.5.1 Stability versus Confidence Level cut

Ideally, the fit values should be independent of the cut on the confidence level (above a reasonable threshold of typically 0.10).

The fits numbered from 21 to 25 reflect different slices of confidence level. For $\eta\eta\gamma$, slices 21 to 23 are respectively (0-33%), (33 -67%) and (67% to 100%). For $\eta\pi^0\gamma$ and $\pi^0\pi^0\gamma$, slices 21 to 25 are respectively (0-20%), (20-40%), (40-60%), (60-80%) and (80-100%).

Because of the very low statistics, the stability of the $\eta\eta\gamma$ channel for the desired signal is poor, but there is no systematic trend among the three slices. The background is stable across these slices.

For the $\eta\pi^0\gamma$ and $\pi^0\pi^0\gamma$ groups, all channels are stable across the upper four slices (22-25), with variations in fit 21, because this includes more junk events at 0% confidence level. Because there is no great systematic difference between the $\omega\rightarrow\pi^0\gamma$ and $\omega\rightarrow\eta\gamma$ decays (other than final particles of different mass), the stability of $\omega\rightarrow\pi^0\gamma$ indicates that in principle the fits of $\omega\rightarrow\eta\gamma$ should be independent of confidence level.

Group	Dim	Amp	Bkgrd	BR($\omega\to\eta\gamma$)/table	BR($\rho^0\to\eta\gamma$)/table
$\eta\eta\gamma$	1	I	A	0.30 ± 0.07	–
	1	I	B	0.22 ± 0.07	–
	2	I	A	0.25 ± 0.07	–
	2	I	B	$0.25^{+0.07}_{-0.20}$	$0.0^{+3.0}$
	1	II	A	0.36 ± 0.07	–
	1	II	B	0.28 ± 0.07	–
	2	II	A	0.35 ± 0.07	–
	2	II	B	$0.20^{+0.12}_{-0.12}$	$1.5^{+2.0}_{-1.5}$
	1	III	A	0.37 ± 0.07	–
	1	III	B	0.28 ± 0.07	–
	2	III	A	0.35 ± 0.07	–
	2	III	B	$0.26^{+0.10}_{-0.10}$	$0.0^{+2.5}$
$\eta\pi^0\gamma$	1	I	C	$1.4^{+0.7}_{-0.5}$	$0.6^{+0.7}_{-0.5}$
	1	I	D	$2.2^{+0.4}_{-0.8}$	$0.0^{+0.6}$
	2	I	D	$0.0^{+0.3}$	$0.0^{+0.1}$
	1	II	C	1.9 ± 0.6	$0.7^{+0.9}_{-0.7}$
	1	II	D	2.2 ± 0.5	$0.0^{+0.5}$
	2	II	D	$0.0^{+0.3}$	$0.0^{+0.1}$
	1	III	C	1.9 ± 0.5	1.0 ± 1.0
	1	III	D	2.2 ± 0.4	$0.0^{+1.0}$
	2	III	D	$0.0^{+0.3}$	$0.0^{+0.1}$

Key

Dim	Description
1	Fit of 1D mass($\eta\gamma$) projection, 650 to 1200 MeV
2	Fit of entire 2D Dalitz plot.

Amp	Descriptions
I	Coherent amplitudes with mixing between ρ^0 and ω
II	Incoherent amplitudes with mixing.
III	Incoherent amplitudes with no mixing.

Background	Description
A	$p\overline{p}\to\pi^0\eta\eta$ free, no $p\overline{p}\to\eta\eta\gamma$
B	$p\overline{p}\to\pi^0\eta\eta$ fixed to tabulated, $p\overline{p}\to\eta\eta\gamma$ free
C	$p\overline{p}\to\pi^0\pi^0\eta$ free, no $p\overline{p}\to\eta\pi^0\gamma$
D	$p\overline{p}\to\pi^0\pi^0\eta$ fixed to tabulated, $p\overline{p}\to\eta\pi^0\gamma$ free

Table 9.3: Results of $\eta\eta\gamma$ and $\eta\pi^0\gamma$ scans over BR($\omega\to\eta\gamma$) and BR($\rho^0\to\eta\gamma$) in units of tabulated values. "–" indicates that the fit converged to an unreasonable value, so this was fixed to 1.0.

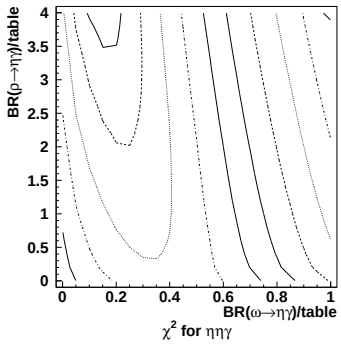

($\eta\eta\gamma$ 1-I-A)

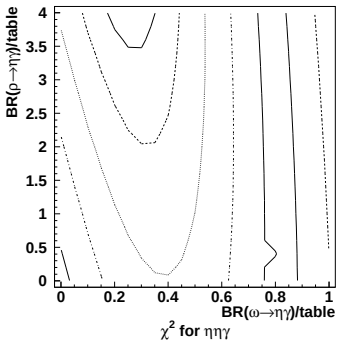

($\eta\eta\gamma$ 1-II-A)

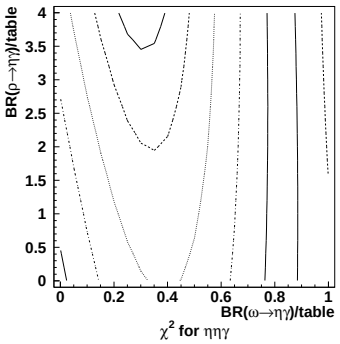

($\eta\eta\gamma$ 1-III-A)

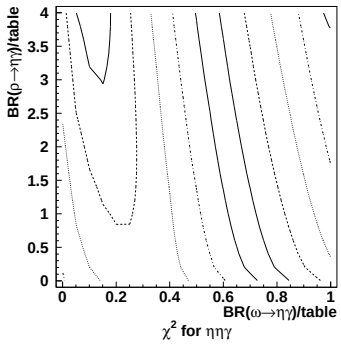

($\eta\eta\gamma$ 1-I-B)

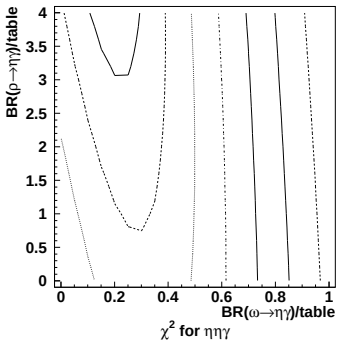

($\eta\eta\gamma$ 1-II-B)

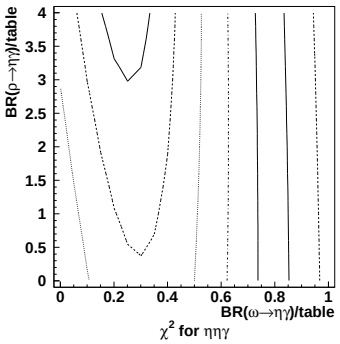

($\eta\eta\gamma$ 1-III-B)

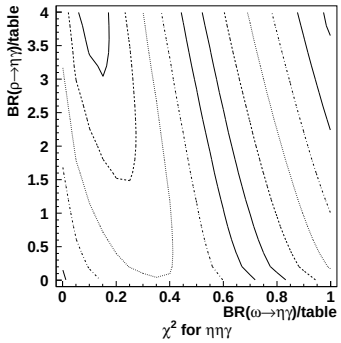

($\eta\eta\gamma$ 2-I-A)

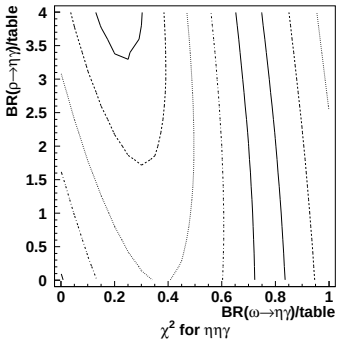

($\eta\eta\gamma$ 2-II-A)

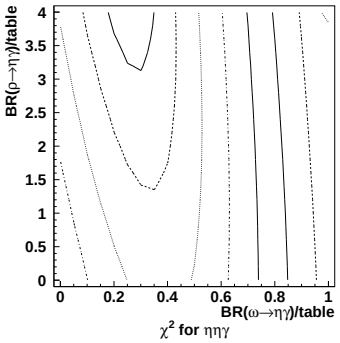

($\eta\eta\gamma$ 2-III-A)

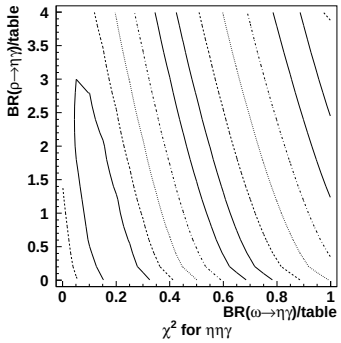

($\eta\eta\gamma$ 2-I-B)

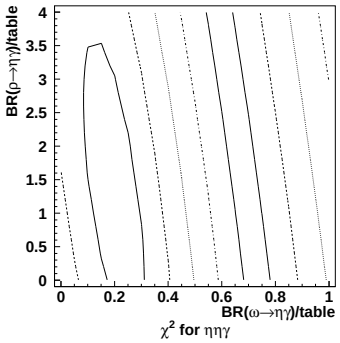

($\eta\eta\gamma$ 2-II-B)

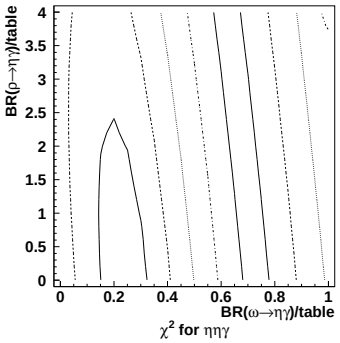

($\eta\eta\gamma$ 2-III-B)

Figure 9.1: $\Delta\chi = 1$ contour lines of the fit of the $\eta\eta\gamma$ group vs BR($\omega \rightarrow \eta\gamma$) and BR($\rho^0 \rightarrow \eta\gamma$) in units of tabulated values. See table 9.3 for a key to the labels.

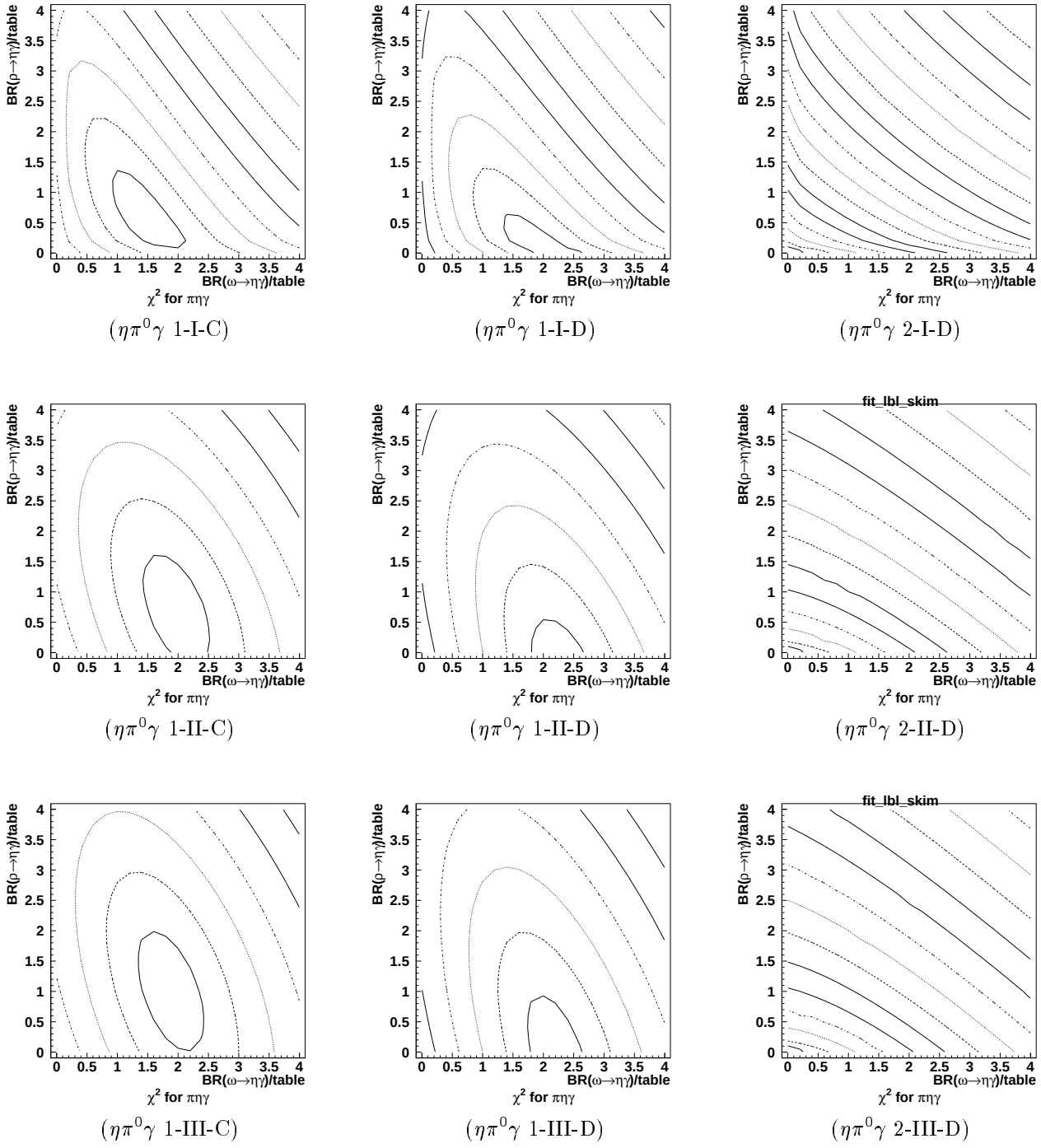

($\eta\pi^0\gamma$ 1-I-C) ($\eta\pi^0\gamma$ 1-I-D) ($\eta\pi^0\gamma$ 2-I-D)

($\eta\pi^0\gamma$ 1-II-C) ($\eta\pi^0\gamma$ 1-II-D) ($\eta\pi^0\gamma$ 2-II-D)

($\eta\pi^0\gamma$ 1-III-C) ($\eta\pi^0\gamma$ 1-III-D) ($\eta\pi^0\gamma$ 2-III-D)

Figure 9.2: $\Delta\chi = 1$ contour lines of the fit of the $\eta\pi^0\gamma$ group vs BR($\omega\rightarrow\eta\gamma$) and BR($\rho^0\rightarrow\eta\gamma$) in units of tabulated values. See table 9.3 for a key to the labels.

Table 9.4: The fit parameters for the $\eta\eta\gamma$ group for various fit attemps. Values shown without errors were fixed during the fit. Note that the 2D fits have each event entered twice, thus the actual number of events is half of the given value in parentheses.

fit no.	$\chi^2/d.o.f.$		$\eta((\omega/\rho^0)\to\eta\gamma)$		$\pi^0\pi^0\eta$		$\pi^0\eta\eta$		$\eta(\omega\to\pi^0\gamma)$		$\eta\eta\gamma$		$\eta\eta$	
	1D	2D	1D	2D	1D	2D	1D	2D	1D	2D	1D	2D	1D	2D
1	1.25	1.54	$1.13^{+0.34}_{-0.35}$	$1.01^{+0.31}_{-0.31}$	1.00	1.00	1.00	1.00	1.00	$1.48^{+0.17}_{-0.18}$	$0.52^{+0.06}_{-0.06}$	$0.60^{+0.04}_{-0.04}$	$2.14^{+0.37}_{-0.38}$	$0.97^{+0.27}_{-0.27}$
			(149)	(137)	(444)	(627)	(2109)	(2876)	(278)	(455)	(749)	(1246)	(202)	(98)
2	1.65	1.16	$1.02^{+0.29}_{-0.29}$	0.76 ± 0.00	1.00	1.00	1.00	1.00	1.00	1.06 ± 0.00	$0.24^{+0.05}_{-0.05}$	0.30 ± 0.00	$0.47^{+0.48}_{-0.49}$	$1.13^{+0.32}_{-0.37}$
			(104)	(81)	(113)	(146)	(969)	(1393)	(27)	(30)	(274)	(496)	(13)	(34)
3	0.92	1.58	$1.01^{+0.34}_{-0.35}$	1.02 ± 1.05	1.00	1.00	1.00	1.00	1.00	$0.00^{+0.00}_{-0.33}$	$0.45^{+0.06}_{-0.06}$	0.64 ± 0.07	$2.51^{+0.62}_{-0.65}$	$0.92^{+0.22}_{-0.23}$
			(125)	(129)	(349)	(523)	(1972)	(2729)	(77)	(0)	(620)	(1284)	(141)	(57)
5	1.64	1.04	$0.95^{+0.28}_{-0.28}$	0.75 ± 0.28	1.00	1.00	1.00	1.00	1.00	$0.00^{+0.00}_{-0.25}$	$0.22^{+0.05}_{-0.05}$	$0.30^{+0.03}_{-0.03}$	$1.51^{+1.24}_{-1.45}$	1.10 ± 0.79
			(93)	(76)	(105)	(137)	(937)	(1358)	(14)	(0)	(244)	(477)	(19)	(15)
21	0.98	1.63	$0.35^{+0.77}_{-0.78}$	0.66 ± 0.66	1.00	1.00	1.00	1.00	1.00	$0.00^{+0.00}_{-0.18}$	$0.94^{+0.14}_{-0.14}$	$1.26^{+0.09}_{-0.09}$	$2.32^{+0.59}_{-0.62}$	$0.84^{+0.21}_{-0.21}$
			(17)	(33)	(293)	(454)	(1417)	(1905)	(73)	(0)	(511)	(1005)	(121)	(48)
22	1.39	0.98	$0.92^{+0.44}_{-0.45}$	$0.00^{+0.00}_{-0.32}$	1.00	1.00	1.00	1.00	1.00	$0.00^{+0.00}_{-0.57}$	$0.18^{+0.08}_{-0.08}$	$0.30^{+0.05}_{-0.05}$	2.00 ± 0.01	$2.00^{+0.49}_{-0.00}$
			(32)	(0)	(26)	(29)	(320)	(465)	(3)	(0)	(66)	(163)	(4)	(4)
23	0.88	1.04	1.77 ± 0.40	1.15 ± 0.39	1.00	1.00	1.00	1.00	1.00	2.00 ± 0.05	$0.18^{+0.06}_{-0.06}$	$0.20^{+0.04}_{-0.04}$	$0.00^{+0.00}_{-1.83}$	$0.00^{+0.00}_{-0.36}$
			(69)	(46)	(29)	(39)	(233)	(358)	(0)	(0)	(81)	(130)	(0)	(0)
60	1.65	1.16	$1.02^{+0.29}_{-0.29}$	0.76 ± 0.00	1.00	1.00	1.00	1.00	1.00	1.06 ± 0.00	$0.24^{+0.05}_{-0.05}$	0.30 ± 0.00	$0.47^{+0.48}_{-0.49}$	$1.13^{+0.32}_{-0.37}$
			(104)	(81)	(113)	(146)	(969)	(1393)	(27)	(30)	(274)	(496)	(13)	(34)
61	1.66	1.15	$1.00^{+0.29}_{-0.29}$	$0.74^{+0.25}_{-0.26}$	1.00	1.00	1.00	1.00	1.00	1.17 ± 0.79	$0.24^{+0.05}_{-0.05}$	$0.30^{+0.03}_{-0.03}$	$0.50^{+0.51}_{-0.52}$	1.20 ± 0.38
			(103)	(79)	(113)	(145)	(969)	(1393)	(24)	(29)	(276)	(495)	(13)	(35)
62	1.68	1.04	$0.94^{+0.28}_{-0.29}$	$0.75^{+0.26}_{-0.26}$	1.00	1.00	1.00	1.00	1.00	$0.00^{+0.00}_{-0.35}$	$0.25^{+0.05}_{-0.04}$	0.30 ± 0.03	$0.00^{+0.03}_{-1.30}$	$1.11^{+0.38}_{-0.40}$
			(94)	(77)	(109)	(142)	(951)	(1374)	(16)	(0)	(279)	(491)	(0)	(18)
63	1.54	1.03	$1.05^{+0.29}_{-0.30}$	$0.80^{+0.26}_{-0.27}$	1.00	1.00	1.00	1.00	1.00	$0.00^{+0.00}_{-0.45}$	$0.22^{+0.05}_{-0.05}$	$0.30^{+0.03}_{-0.03}$	2.00 ± 0.00	0.52 ± 0.43
			(93)	(73)	(82)	(112)	(872)	(1273)	(10)	(0)	(221)	(450)	(12)	(3)
64	1.67	1.31	$1.03^{+0.27}_{-0.29}$	$0.93^{+0.28}_{-0.28}$	1.00	1.00	1.00	1.00	1.00	$0.00^{+0.01}_{-1.30}$	$0.26^{+0.05}_{-0.05}$	$0.31^{+0.04}_{-0.04}$	0.00 ± 0.00	$0.00^{+0.02}_{-1.59}$
			(80)	(75)	(52)	(80)	(755)	(1127)	(9)	(0)	(226)	(412)	(0)	(0)

fit no.	$\chi^2/d.o.f.$		$\pi^0((\omega/\rho^0)\to\eta\gamma)$		$\pi^0\pi^0\eta$		$\pi^0\eta\eta$		$\eta(\omega\to\pi^0\gamma)$		$\eta\pi^0\gamma$	
	1D	2D	1D	2D	1D	2D	1D	2D	1D	2D	1D	2D
1	3.23	3.95	2.00 ± 0.00	$0.09^{+0.12}_{-0.18}$	1.00	1.00	1.00	1.00	$1.05^{+0.01}_{-0.01}$	1.05 ± 0.01	$1.03^{+0.03}_{-0.04}$	$0.95^{+0.03}_{-0.03}$
			(173)	(14)	(20784)	(41896)	(738)	(915)	(76586)	(78812)	(9435)	(15406)
2	2.92	3.51	$0.52^{+5.28}_{-5.18}$	$0.16^{+0.17}_{-0.35}$	1.00	1.00	1.00	1.00	$1.04^{+0.01}_{-0.01}$	$1.04^{+0.01}_{-0.01}$	$0.94^{+0.06}_{-0.06}$	$0.82^{+0.02}_{-0.02}$
			(35)	(18)	(11590)	(22094)	(145)	(192)	(59239)	(60672)	(6815)	(10507)
3	3.13	3.58	$11.56^{+5.32}_{-5.27}$	$0.10^{+0.10}_{-0.16}$	1.00	1.00	1.00	1.00	$1.05^{+0.01}_{-0.01}$	$1.05^{+0.01}_{-0.01}$	$0.95^{+0.06}_{-0.06}$	$0.93^{+0.03}_{-0.03}$
			(915)	(12)	(19291)	(34184)	(671)	(817)	(69003)	(70685)	(8131)	(12727)
4	3.36	3.51	$16.88^{+5.22}_{-5.22}$	$0.12^{+0.18}_{-0.35}$	1.00	1.00	1.00	1.00	$1.05^{+0.01}_{-0.01}$	$1.05^{+0.01}_{-0.01}$	$0.89^{+0.06}_{-0.06}$	$0.94^{+0.03}_{-0.03}$
			(1409)	(11)	(20711)	(37567)	(735)	(902)	(74244)	(75934)	(8070)	(14029)
5	2.78	3.27	$-1.59^{+5.41}_{-5.31}$	$0.18^{+0.21}_{-0.33}$	1.00	1.00	1.00	1.00	$1.04^{+0.01}_{-0.01}$	$1.04^{+0.01}_{-0.01}$	$0.99^{+0.06}_{-0.06}$	0.84 ± 0.03
			(-102)	(16)	(10767)	(18389)	(137)	(176)	(53620)	(54631)	(6710)	(9071)
6	3.12	3.34	$3.37^{+5.18}_{-5.10}$	$0.40^{+0.71}_{-0.94}$	1.00	1.00	1.00	1.00	$1.03^{+0.01}_{-0.01}$	$1.04^{+0.01}_{-0.01}$	$0.91^{+0.06}_{-0.06}$	$0.83^{+0.03}_{-0.03}$
			(223)	(30)	(11555)	(20357)	(145)	(190)	(57502)	(58603)	(6559)	(9749)
7	3.31	3.39	$15.80^{+5.24}_{-5.21}$	$0.14^{+0.21}_{-0.37}$	1.00	1.00	1.00	1.00	$1.05^{+0.01}_{-0.01}$	1.05 ± 0.01	$0.91^{+0.06}_{-0.06}$	0.97 ± 0.03
			(1224)	(12)	(19239)	(31766)	(668)	(810)	(67138)	(68480)	(7719)	(12662)
8	2.97	3.17	$1.38^{+5.43}_{-5.18}$	$0.39^{+0.59}_{-0.85}$	1.00	1.00	1.00	1.00	1.04 ± 0.01	$1.04^{+0.01}_{-0.01}$	$0.96^{+0.06}_{-0.06}$	$0.86^{+0.03}_{-0.03}$
			(86)	(27)	(10743)	(17436)	(136)	(175)	(52197)	(53021)	(6454)	(8858)
21	1.56	1.92	$-5.00^{+7.41}_{-7.48}$	$0.30^{+0.24}_{-0.35}$	1.00	1.00	1.00	1.00	$1.08^{+0.01}_{-0.01}$	$1.04^{+0.01}_{-0.01}$	1.37 ± 0.11	$1.39^{+0.06}_{-0.06}$
			(-125)	(15)	(11375)	(24101)	(633)	(778)	(24127)	(24196)	(3816)	(6827)
22	*-1.00*	1.57	–	1.93 ± 1.59	–	1.00	–	1.00	–	0.97	–	0.83 ± 0.06
				(39)		(5937)		(54)		(12152)		(2263)
23	1.59	1.53	-3.43 ± 3.96	$0.41^{+0.38}_{-0.55}$	1.00	1.00	1.00	1.00	$1.06^{+0.01}_{-0.01}$	0.98 ± 0.02	1.05 ± 0.09	1.04 ± 0.07
			(-62)	(12)	(2383)	(4439)	(28)	(35)	(13001)	(12373)	(1630)	(2862)
24	1.49	1.41	-1.69 ± 5.68	$0.31^{+0.26}_{-0.37}$	1.00	1.00	1.00	1.00	$1.02^{+0.01}_{-0.01}$	$0.95^{+0.01}_{-0.01}$	$1.02^{+0.09}_{-0.09}$	$0.91^{+0.05}_{-0.05}$
			(-24)	(9)	(2217)	(4017)	(20)	(27)	(13140)	(12522)	(1651)	(2629)
25	1.92	1.57	$0.00^{+0.00}_{-1.29}$	0.32 ± 0.26	1.00	1.00	1.00	1.00	$1.05^{+0.01}_{-0.01}$	$0.97^{+0.01}_{-0.01}$	$0.99^{+0.07}_{-0.07}$	$0.91^{+0.05}_{-0.05}$
			(0)	(8)	(1843)	(3399)	(16)	(20)	(13653)	(12895)	(1648)	(2689)
32	1.55	1.97	0.00 ± 0.00	–	1.04	1.37 ± 0.04	1.04	1.00	$1.03^{+0.01}_{-0.01}$	$1.05^{+0.01}_{-0.01}$	$0.83^{+0.07}_{-0.07}$	–
			(0)		(3075)	(8120)	(40)	(54)	(12619)	(13080)	(1309)	
33	1.59	1.89	$-3.43^{+4.14}_{-4.04}$	–	1.04	1.65 ± 0.05	1.04	1.00	$1.06^{+0.01}_{-0.01}$	1.07 ± 0.01	1.00 ± 0.09	–
			(-62)		(2472)	(7329)	(29)	(35)	(12999)	(13459)	(1547)	
34	1.49	1.63	$-1.56^{+5.89}_{-5.70}$	–	1.04	$1.76^{+0.05}_{-0.05}$	1.04	1.00	$1.02^{+0.01}_{-0.01}$	1.03 ± 0.01	$0.98^{+0.09}_{-0.09}$	–
			(-22)		(2300)	(7076)	(21)	(27)	(13136)	(13551)	(1581)	
35	1.91	1.80	$0.00^{+0.00}_{-1.31}$	–	1.04	$1.95^{+0.06}_{-0.06}$	1.04	1.00	$1.04^{+0.01}_{-0.01}$	$1.04^{+0.01}_{-0.01}$	$0.96^{+0.07}_{-0.07}$	–
			(0)		(1912)	(6637)	(17)	(20)	(13650)	(13925)	(1589)	

Table 9.5: The fit parameters for the $\eta\pi^0\gamma$ group for various fit attemps. Values shown without errors were fixed during the fit.

Table 9.6: The fit parameters for the $\pi^0\pi^0\gamma$ group for various fit attemps. Values shown without errors were fixed during the fit. Note that the 2D fits have each event entered twice, thus the actual number of events is half of the given value in parentheses.

fit no.	$\chi^2/d.o.f.$		$\pi^0\pi^0\eta$		$\pi^0\pi^0$		$\pi^0\pi^0\pi^0$		$\eta(\omega\to\pi^0\gamma)$		$\pi^0\pi^0\gamma$		$\pi^0(\omega\to\pi^0\gamma)$	
	1D	2D	1D	2D	1D	2D	1D	2D	1D	2D	1D	2D	1D	2D
1	2.02	2.57	1.00	1.00	1.00	1.00	$1.20^{+0.02}_{-0.02}$	1.08 ± 0.01	1.00	1.00	$0.00^{+0.00}_{-0.01}$	$0.07^{+0.01}_{-0.01}$	$0.95^{+0.01}_{-0.01}$	0.98 ± 0.01
			(4044)	(5283)	(525)	(10643)	(62513)	(116666)	(197)	(291)	(0)	(6825)	(64227)	(66929)
2	1.64	2.57	1.00	1.00	1.00	1.00	$1.21^{+0.07}_{-0.02}$	1.04 ± 0.02	1.00	1.00	$0.00^{+0.00}_{-0.03}$	0.09 ± 0.01	$0.95^{+0.01}_{-0.01}$	$0.97^{+0.01}_{-0.01}$
			(780)	(1181)	(205)	(7695)	(36959)	(62206)	(40)	(62)	(0)	(7503)	(50968)	(52681)
3	1.75	2.55	1.00	1.00	1.00	1.00	$1.19^{+0.02}_{-0.02}$	1.04 ± 0.02	1.00	1.00	$0.00^{+0.00}_{-0.01}$	0.08 ± 0.01	$0.99^{+0.01}_{-0.01}$	1.02 ± 0.01
			(3401)	(4248)	(180)	(5989)	(51180)	(83665)	(182)	(252)	(0)	(7011)	(54117)	(55911)
5	1.64	2.51	1.00	1.00	1.00	1.00	$1.19^{+0.09}_{-0.04}$	$0.98^{+0.02}_{-0.02}$	1.00	1.00	$0.00^{+0.02}_{-0.04}$	$0.11^{+0.01}_{-0.01}$	$0.99^{+0.01}_{-0.01}$	$1.01^{+0.01}_{-0.01}$
			(655)	(920)	(104)	(4528)	(30809)	(45008)	(38)	(55)	(198)	(7355)	(43066)	(44297)
21	1.91	1.85	1.00	1.00	1.00	1.00	$1.18^{+0.07}_{-0.07}$	1.12 ± 0.02	1.00	1.00	$0.01^{+0.08}_{-0.08}$	0.01 ± 0.03	0.93 ± 0.02	$0.99^{+0.02}_{-0.02}$
			(3508)	(4494)	(375)	(4096)	(31614)	(65624)	(169)	(248)	(149)	(451)	(19077)	(20639)
22	0.98	1.51	1.00	1.00	1.00	1.00	$0.44^{+0.08}_{-0.08}$	0.96 ± 0.05	1.00	1.00	$0.45^{+0.05}_{-0.05}$	0.14 ± 0.02	$1.00^{+0.02}_{-0.02}$	0.98 ± 0.02
			(226)	(344)	(66)	(1862)	(3499)	(14777)	(14)	(23)	(4883)	(2426)	(11559)	(11626)
23	1.49	1.73	1.00	1.00	1.00	1.00	$0.00^{+0.00}_{-0.05}$	$0.97^{+0.03}_{-0.05}$	1.00	1.00	$0.66^{+0.03}_{-0.02}$	$0.14^{+0.02}_{-0.02}$	$1.04^{+0.02}_{-0.02}$	$1.01^{+0.02}_{-0.02}$
			(131)	(187)	(45)	(1726)	(0)	(12197)	(5)	(8)	(7359)	(2418)	(11856)	(11790)
24	*1.54*	1.76	1.00	1.00	1.00	1.00	0.38 ± 0.25	$1.04^{+0.05}_{-0.05}$	1.00	1.00	0.36 ± 0.05	$0.07^{+0.02}_{-0.02}$	0.99 ± 0.09	$0.99^{+0.02}_{-0.02}$
			(93)	(139)	(20)	(1566)	(2186)	(11615)	(6)	(6)	(4313)	(1209)	(11944)	(12132)
25	1.67	1.58	1.00	1.00	1.00	1.00	$0.39^{+0.13}_{-0.13}$	$0.98^{+0.05}_{-0.03}$	1.00	1.00	$0.39^{+0.05}_{-0.06}$	$0.14^{+0.00}_{-0.02}$	$1.00^{+0.02}_{-0.02}$	1.00 ± 0.02
			(83)	(116)	(17)	(1392)	(2064)	(9696)	(2)	(3)	(4460)	(2572)	(11816)	(11911)

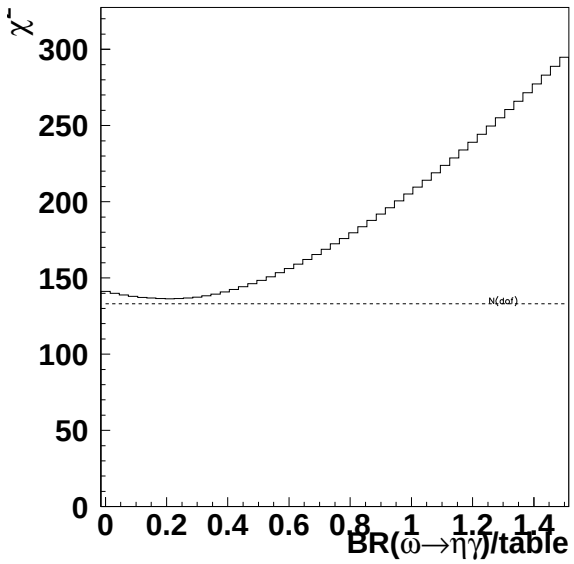

Figure 9.3: χ^2 versus BR($\omega \rightarrow \eta\gamma$) with BR($\rho^0 \rightarrow \eta\gamma$) = 1. The line is drawn at $\chi^2 = N(dof)$

9.5.2 Stability versus XPI1 cut in $\eta\eta\gamma$

We varied the XPI1 cut, which suppresses the feed-through from $\eta(\omega \rightarrow \pi^0\gamma)$, to see if the data is still sensitive to the cut boundaries, even when they are large. If there was contamination, the fitted value of $\eta(\omega \rightarrow \eta\gamma)$ would drop with a wider cut, but this is not seen. Cut sets 60 to 64 (see table 8.1 are variations of XPI1.

9.6 Summary of Errors

Source	Percent Contribution to	
	BR($\omega \rightarrow \eta\gamma$)	BR($\rho^0 \rightarrow \eta\gamma$)
Tabulated errors	6 %	–
Unexplained errors due to rev-a vs rev-b	8 %	–
Error because of decay angle	4 %	–
Existence of flat $\eta\eta\gamma$ or $\eta\pi^0\gamma$issue	20 %	>> 100%
1-D vs 2-D fit issue	12 %	–
Variation in confidence level	< 10%	–
Variation in xpi1 cut	< 10%	–
Total Systematic summed in quadrature	30 %	Too Big
Average Statistic Error	26 %	–

Because the fit result for BR($\rho^0 \rightarrow \eta\gamma$) changes so much based on the existence of the $\eta\pi^0\gamma$ background, we can not give any new information on the measurement of $\rho^0 \rightarrow \eta\gamma$. Our measurement is consistent with previous tabulated values.

The systematic errors for BR($\omega \rightarrow \eta\gamma$) (30%) compare to the statistical error (26%). Adding these two together, we get 40% error.

9.7 Final Result

For each amplitude theory (I,II,III), we average the four fits (1-A,1-B, 2-A and 2-B), and assign each an error of 40% based on the discussions in the last section. We repeat the definitions of the amplitude theories for combining ρ^0/ω here for convenience:

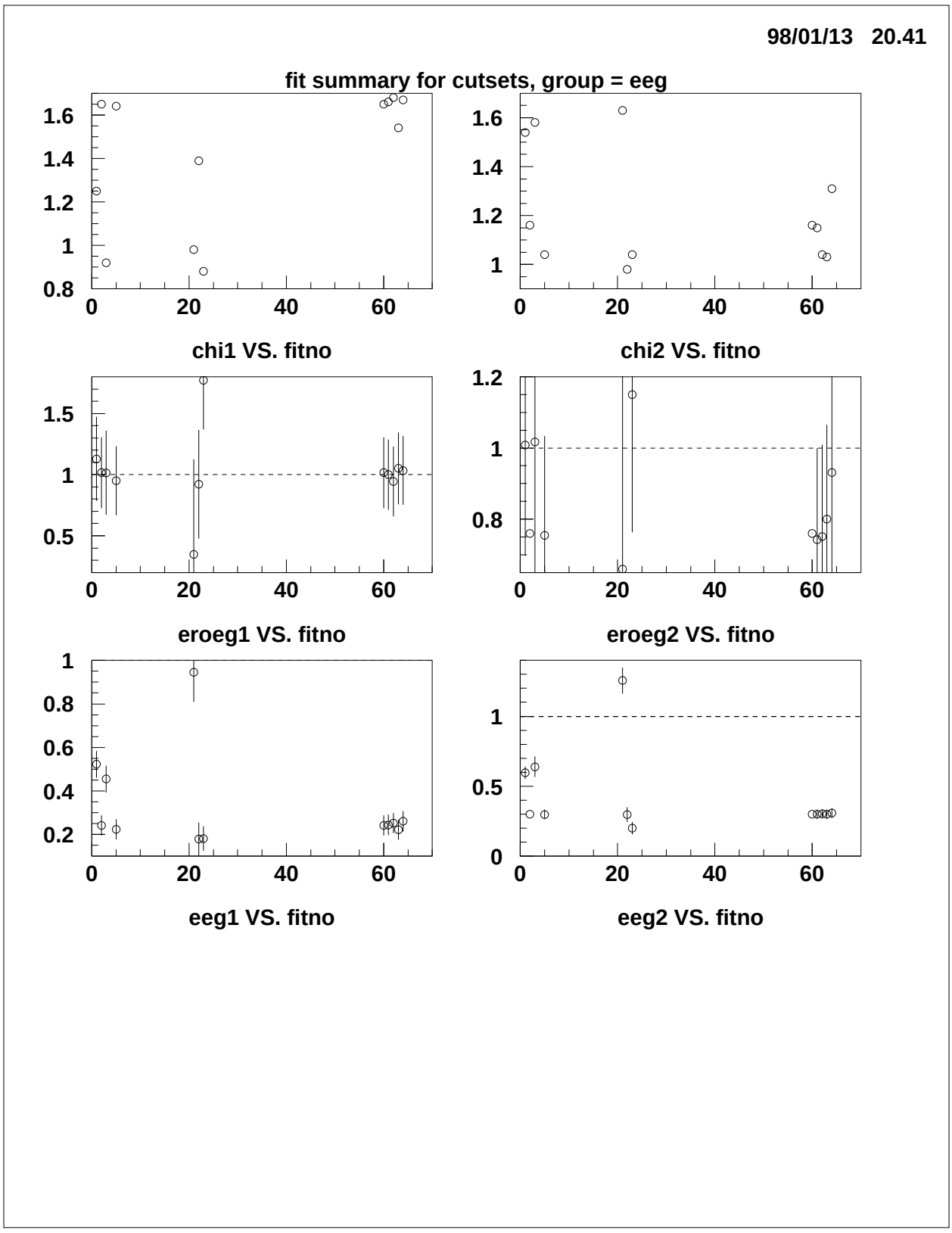

Figure 9.4: A graphical depiction of the important values of table 9.4. Note the scale of `eroeg` ($\eta((\omega/\rho^0)\rightarrow\eta\gamma)$) is not in reference to the PDG tabulated value (8.3×10^{-4}) but in reference to (2.5×10^{-4}). The scale of `eeg` is of course arbitrary.

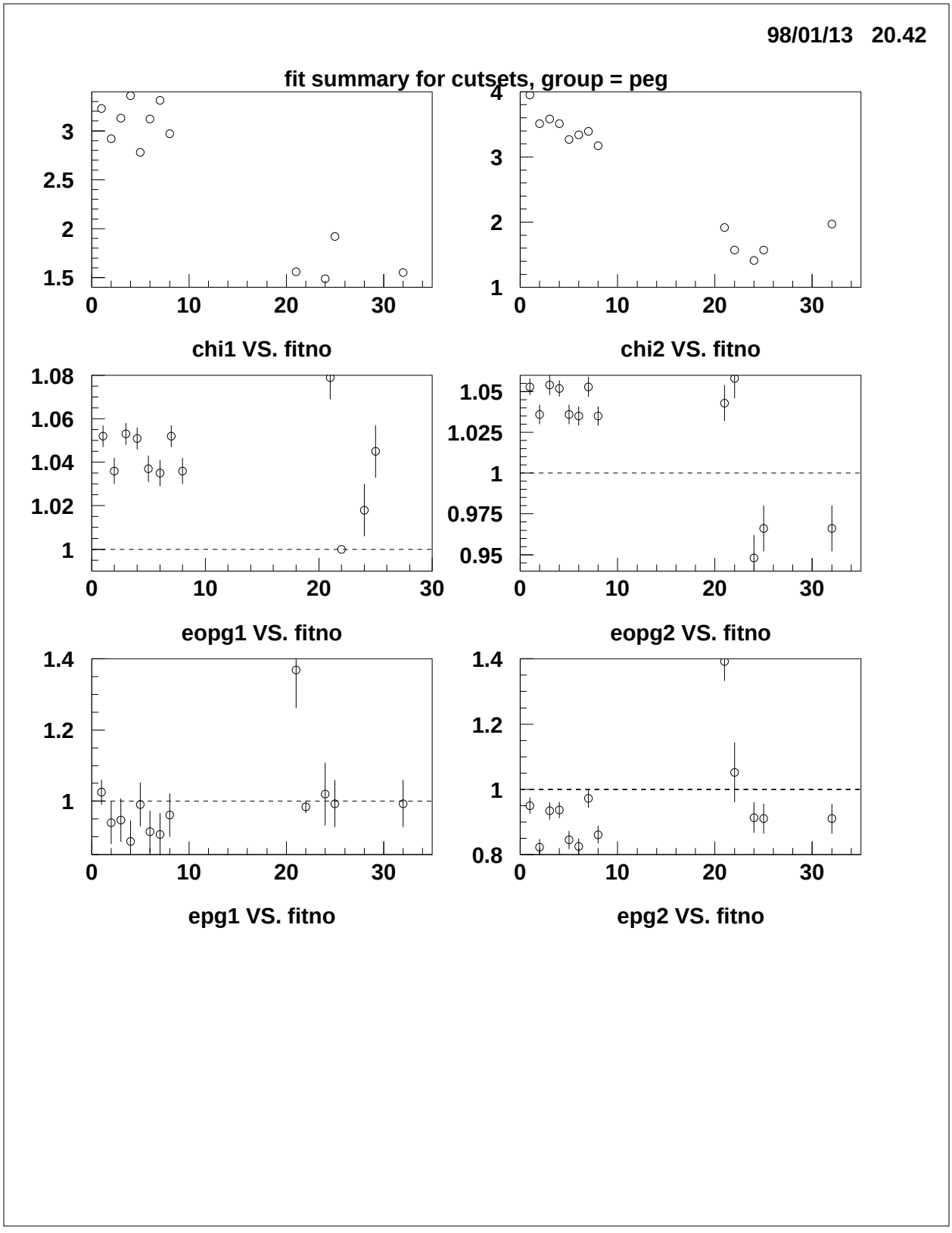

Figure 9.5: A graphical depiction of the important values of table 9.5. The scale of `epg` is of course arbitrary.

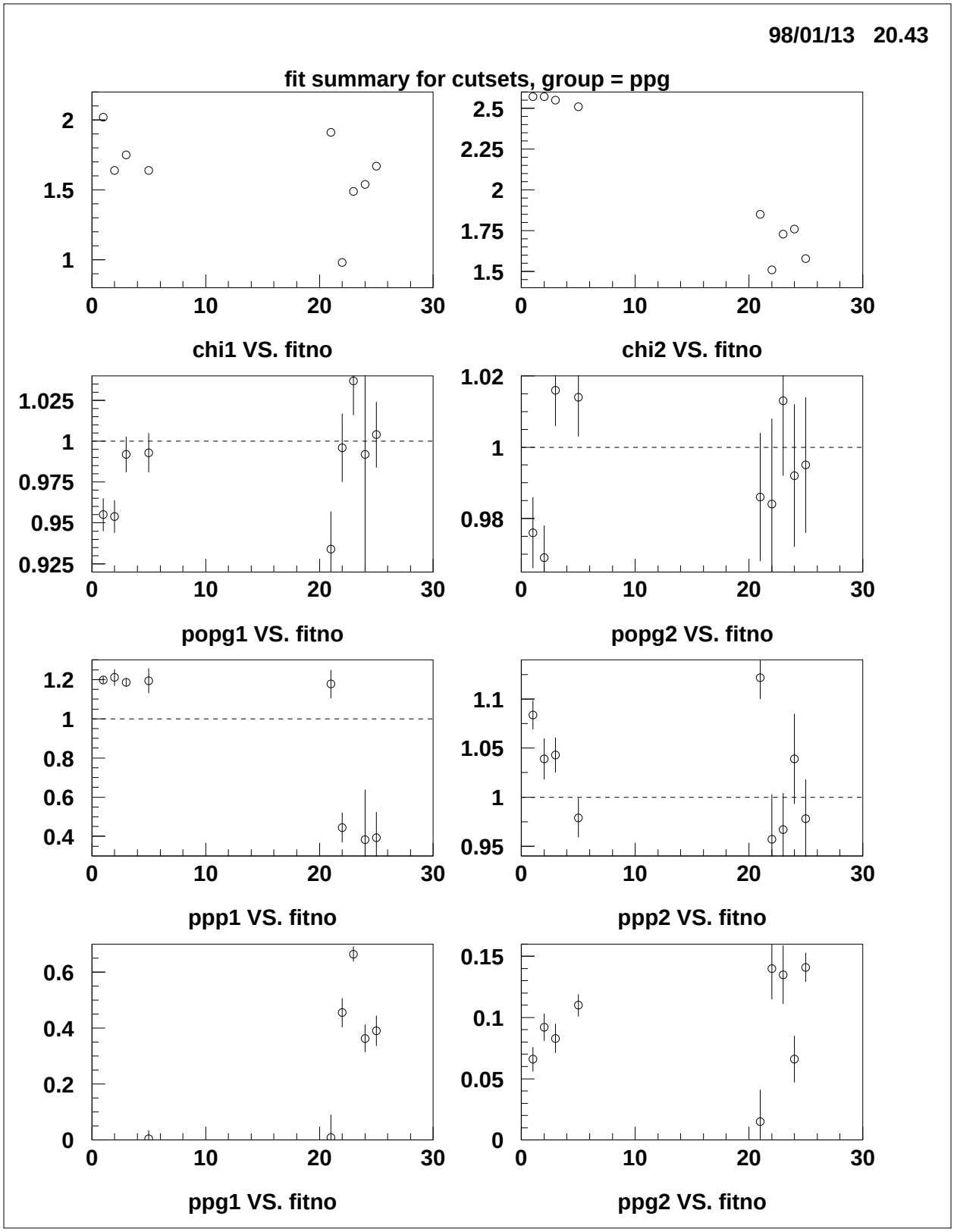

Figure 9.6: A graphical depiction of the important values of table 9.6. The scale of ppg is of course arbitrary.

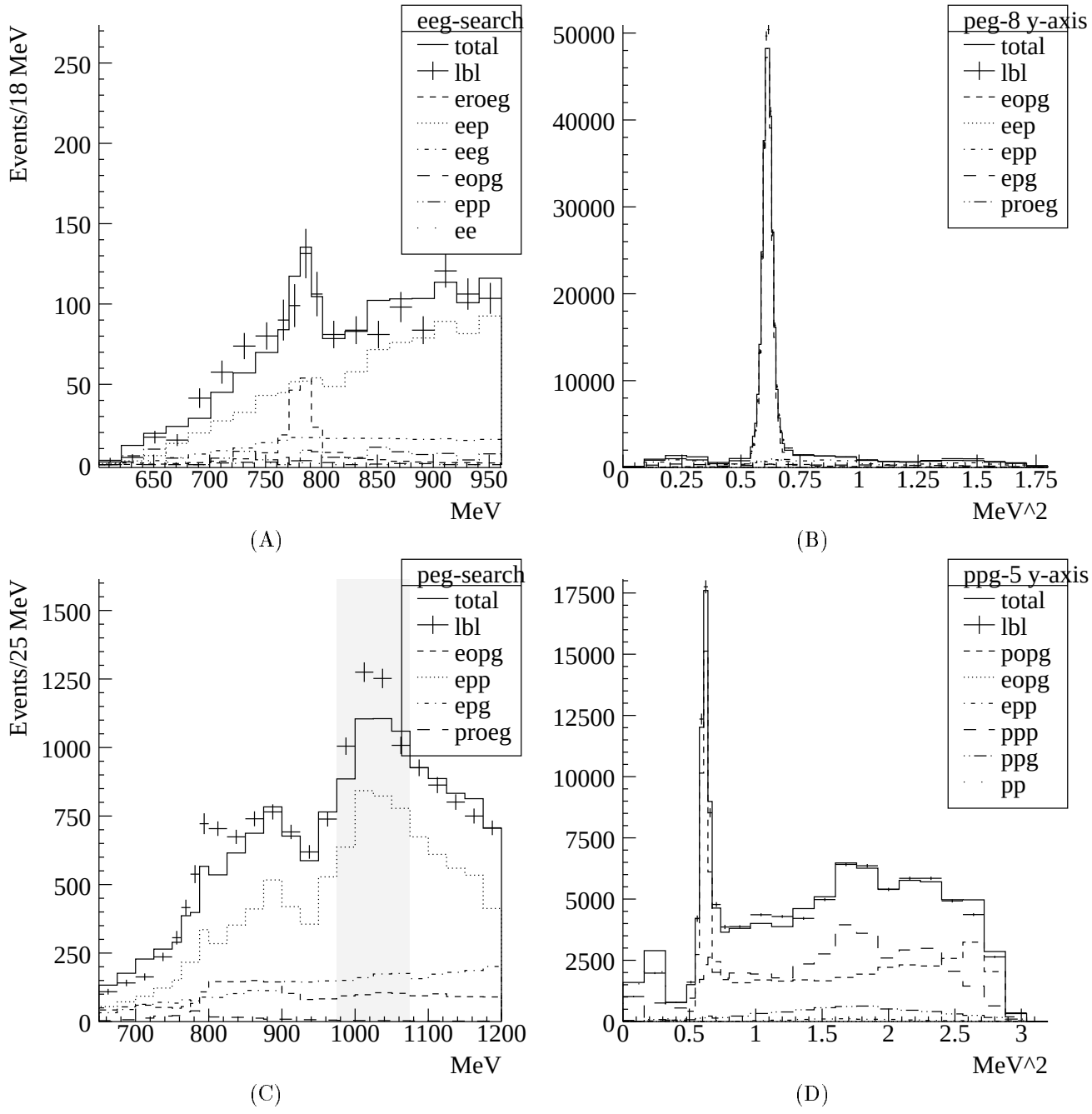

Figure 9.7: (a)The $m(\eta\gamma)$ projection of the $\eta\eta\gamma$ channel fit (1-I-B), (b) The $m^2(\pi^0\gamma)$ projection of the $\eta\pi^0\gamma$ channel fit. (c) the $m(\eta\gamma)$ fit of the $\eta\pi^0\gamma$ channel. The gray region is omitted from the fit because of the possibility of $\phi\rightarrow\eta\gamma$. (d) the $m^2(\pi^0\gamma)$ projection of the $\pi^0\pi^0\gamma$ channel fit.

I, Fully coherent and isospin mixed
II, Incoherent but isospin mixed
III, Incoherent and pure isospin

Because the measurements of the reference channels

$$BR(\omega\to\pi^0\gamma[p\overline{p}\to\omega\eta]) = 1.04\pm0.01 \quad (9.1)$$
$$BR(\omega\to\pi^0\gamma[p\overline{p}\to\omega\pi^0]) = 1.01\pm0.01 \quad (9.2)$$
$$(9.3)$$

agree well with each other and with prior expectations, we believe these to be correct.

The fitted value for BR($\omega\to\pi^0\gamma(p\overline{p}\to$œ)) is in good agreement with the tabulated value, which is 1.0±0.11 because of errors in the 0-prong enhancement factor and errors in BR($p\overline{p}\to$œ). To calculate a value for BR($\omega\to\eta\gamma$) explicitly and remove the uncertainty in the absolute measurement of $p\overline{p}\to$œ efficiency, we divide the fit value for $\omega\to\eta\gamma$ by the fit value for $\omega\to\pi^0\gamma$ and multiply by the tabulated value of BR($\omega\to\pi^0\gamma$).

Using the PDG values [14] of BR($\omega\to\pi^0\gamma$) and BR($\omega\to\eta\gamma$) as the references, we get

$$a(I,\eta(\omega\to\eta\gamma)) = 0.23\pm0.09 \quad (9.4)$$
$$a(II,\eta(\omega\to\eta\gamma)) = 0.30\pm0.12 \quad (9.5)$$
$$a(III,\eta(\omega\to\eta\gamma)) = 0.31\pm0.12 \quad (9.6)$$
$$a(\eta(\omega\to\pi^0\gamma)) = 1.04\pm0.01 \quad (9.7)$$
$$BR(\omega\to\eta\gamma) = \frac{a(\eta(\omega\to\eta\gamma))}{a(\eta(\omega\to\pi^0\gamma))}BR(\omega\to\eta\gamma)_{\rm PDG} \quad (9.8)$$

$$BR(I,\omega\to\eta\gamma) = (1.8\pm0.7)\times10^{-4} \quad (9.9)$$
$$BR(II,\omega\to\eta\gamma) = (2.4\pm1.0)\times10^{-4} \quad (9.10)$$
$$BR(III,\omega\to\eta\gamma) = (2.5\pm1.0)\times10^{-4} \quad (9.11)$$

The errors here includes both the statistical error and systematic error.

9.8 Discussion

If we choose to average theories I and II together and increase the errors to include them, we get

$$BR(\omega\to\eta\gamma) = (2.1^{+1.3}_{-1.0})\times10^{-4}$$

The χ^2/N_{dof} for the final fit (2-II-B) is 136/133 which has a confidence level of 41%. If we fix the BR($\omega\to\eta\gamma$) to the PDG tabulated value and run the fit, we get χ^2/N_{dof} = 203/133, which has a confidence level of 2×10^{-7}. The PDG tabulated value, being four times larger than the current result, is clearly inconsistent with the current data.

Chapter 10

Appendix

10.1 Kinematic Fitting

10.1.1 Introduction

A new kinematic fitter was written for the hypothesis, $p\overline{p} \rightarrow K^{\pm}\pi^{\mp}K_S$, because the standard Crystal Barrel software (CBKFIT) does not support this hypothesis. Because it worked very well and is easier to use than CBKFIT, we used it also on this analysis. The software is object-oriented, making it easy to add new constraints. Currently, the constraints are three-momentum conservation and mass conservation at the decay vertices. Any event with 6 or less final state particles can be fitted. (This restraint is imposed by CLHEP, but could be easier expanded if necessary).

There are many new C++ classes.

1. **KinFit** - This is the master class container of the hypotheses. It contains a list of hypotheses.
2. **KinFitHypothesis** - This contains the hypothesis and is a container for the permutations. The fit generates a list of good permutations for each hypothesis for each event. This list is sorted in order of χ^2.
3. **KinFitPermutation** - This contains the permutation of particles. After the fit is done, only valid permutations with valid χ^2 are kept.
4. **KinFitParticle** - A subclass of Particle, contain information about the pulls and also some mechanism for locking the particles when making combinations. These are made in KinFitHypothesis for use in KinFitPermutation. The final answer is in terms of these.

10.1.2 KinFitHypothesis

The Hypothesis class generates the permutations. The problem is to assign the n measured tracks/PEDs to the n final state particles in the predefined hypothesis.

The user initializes the hypothesis with a KinFitParticle, which is a description of the initial state and the immediate daughter particles. Each daughter particle can have further daughters, forming a hierarchy. For instance, the initial state is a $p\overline{p}$ pseudo-particle, with $K^{\pm}$, $\pi^{\mp}$, and K_S as the daughters. The K_S is defined with π^+,π^- as its two daughters.

First the given measured tracks/PEDs are assigned to 3 lists: charged "+", charged "-" and neutral. The final state particles in the hypothesis are symbolically linked to the corresponding lists. The next higher resonances are created using existing resonances; the new resonances are then added to the database to be used for the next iteration of resonance building. Resonances can require certain things about their daughters. For instance, a K_S can require that the two daughter pions came from the same vertex.

When all resonances are built (ending with the $p\overline{p}$ root particle), each instance in the root particle list is copied to a KinFitPermutation. Each permutation is then fitted, and those permutations that fail the fit are deleted. At the end, the remaining permutations are sorted in increasing χ^2.

10.1.3 KinFitPermutation, description of fitting algorithm

The user submits a selected hypothesis, and the software returns a list of possible permutations that minimally satisfy it. If the list is zero, then no permutation worked. The minimum condition of satisfaction is that the total $\chi^2/N < 5.0$. The list is ordered, so the user typically only examines the first element of the list. The user can then extract the new fitted values of 4-momenta and the pulls from the permutation.

There are three momentum constraints ($\vec{p}_{\rm tot} = 0$) and m mass constraints, which are explicitly

$$f_i^{\rm momentum} = \sum_{j=1}^{n} P_i^j \{i = x, y, z\} \tag{10.1}$$

$$f_k^{\rm mass} = \frac{\left(m({\rm theory})_k^2 - m({\rm exp})_k^2\right)}{m({\rm theory})} \{k = 1..m\} \tag{10.2}$$

This gives a total of

$$c = 3 + m$$

constraints. The nominal phase space fit contains only one resonance (one mass constraint), the initial state $(p\overline{p})$, so has $3 + 1 = 4$ constraints as expected.

The measured values of momenta are written as a vector

$$\eta = (p_x^1, p_y^1, p_z^1, p_x^2, p_y^2, p_z^2, \ldots, p_z^n)$$

And the $3n$ by $3n$ block-diagonal symmetric error matrix is written as,

$$\mathcal{G}_\eta^{-1} = \begin{pmatrix} S_1 & & & \\ & S_2 & & \\ & & \ddots & \\ & & & S_n \end{pmatrix}$$

where the individual tracks have error matrices,

$$S_i = \begin{pmatrix} \sigma_{xx} & \sigma_{xy} & \sigma_{xz} \\ \sigma_{yx} & \sigma_{yy} & \sigma_{yz} \\ \sigma_{zx} & \sigma_{zy} & \sigma_{zz} \end{pmatrix}.$$

We then calculate the derivative matrix,

$$\mathcal{B} = \begin{pmatrix} \frac{\partial f_1}{\partial \eta_1} & \cdots & \frac{\partial f_1}{\partial \eta_{3n}} \\ \vdots & \ddots & \vdots \\ \frac{\partial f_c}{\partial \eta_1} & \cdots & \frac{\partial f_c}{\partial \eta_{3n}} \end{pmatrix}.$$

In this case,

$$\mathcal{B} = \begin{pmatrix} \begin{pmatrix} 1 & 0 & 0 \\ 0 & 1 & 0 \\ 0 & 0 & 1 \end{pmatrix} & \begin{pmatrix} 1 & 0 & 0 \\ 0 & 1 & 0 \\ 0 & 0 & 1 \end{pmatrix} & \cdots & \begin{pmatrix} 1 & 0 & 0 \\ 0 & 1 & 0 \\ 0 & 0 & 1 \end{pmatrix} \\ (\vec{F}_1^1)^T & (\vec{F}_1^2)^T & \cdots & (\vec{F}_1^n)^T \\ (\vec{F}_2^1)^T & (\vec{F}_2^2)^T & \cdots & (\vec{F}_2^n)^T \\ \vdots & & & \\ (\vec{F}_m^1)^T & (\vec{F}_m^2)^T & \cdots & (\vec{F}_m^n)^T \end{pmatrix}$$

where

$$\vec{F}_j^i = \frac{E_j \cdot \vec{\beta}^i - \vec{p}_j}{m({\rm theory})_j}$$

where E_j,$\vec{p}_j$,m_j is the energy/momentum/mass of the j^{th} resonances, and $\vec{\beta}^i$ is the velocity of the i^{th} track/PED.

We calculate the covariance matrix, in the constraint basis,

$$\mathcal{G}_{\mathcal{B}} = (\mathcal{B}\mathcal{G}_{\eta}^{-1}\mathcal{B}^T)^{-1}$$

and then the improvements to the measured values,

$$\delta\eta = \mathcal{G}_{\eta}^{-1}\mathcal{B}^T\mathcal{G}_{\mathcal{B}}\mathbf{f}$$

where are iteratively subtracted from the measured values

$$\eta := \eta - \delta\eta$$

The fit desires to make $\mathbf{f} = \mathbf{0}$, so on each calculation,

$$d^2 = \mathbf{f}^T\mathcal{G}_{\mathcal{B}}\mathbf{f}$$

is calculated, and the iterations stop if any of the following conditions is met:

1. The value of d^2 is sufficiently close to zero, which is a successful fit.
2. The value of d^2 is higher than an allowed maximum, and the fit fails.
3. The number of iterations is too high, so the fit fails.
4. An internal error happens, such as inversion of a singular matrix, where the fit of course fails.

At the end of the fit, the χ^2 of the change in the measurements ($\epsilon = \eta - \eta_0$) is calculated,

$$\chi^2 = (\mathcal{B}\epsilon)^T\mathcal{G}_{\mathcal{B}}(\mathcal{B}\epsilon)$$

where the degrees of freedom of the fit are simply the number of constraints, since there are no free parameters,

$$N_{\text{dof}} = 3 + m$$

The reduced χ^2 value is required to be

$$\frac{\chi^2}{N_{\text{dof}}} < 5.0$$

or else the permutation is deleted from the hypothesis.

10.1.4 Final Errors and pulls

In this notation, η = estimates of best values, $\mathbf{y}$ = original data values, $\mathbf{x}$ = parameters of fit. The normal kinematic fit has no free parameters, so $\mathbf{x}$ is not used.

The final errors are calculated using this formula

$$\mathcal{G}_{\eta}^{-1} = \mathcal{G}_{\mathbf{y}}^{-1} - \mathcal{G}_{\mathbf{y}}^{-1}B^T\mathcal{G}_B B\mathcal{G}_{\mathbf{y}}^{-1} + \mathcal{G}_{\mathbf{y}}^{-1}B^T\mathcal{G}_B A(A^T\mathcal{G}_B A)^{-1}A^T\mathcal{G}_B B\mathcal{G}_{\mathbf{y}}^{-1}$$

Note again, that if there are no free parameters, then $A = 0$ as well as $\mathbf{x} = 0$. If a special fit is added, for example the neutral decay position of the $K_S \rightarrow \pi^0\pi^0$ then this will need to be used.

A pull is a measure of the displacement of the measured values to the fitted values. They are constructed so that a valid distribution of pulls will form a normal distribution with width 1 and mean 0. A pull of the observable λ is defined as

$$P = \frac{\lambda_f - \lambda_i}{\sqrt{\sigma(\lambda_i)^2 - \sigma(\lambda_f)^2}},$$

where i denotes value before fitting and f denotes value after fitting. The $\sigma(\lambda_f)$ comes from $\mathcal{G}_{\eta}^{-1}$, while the $\sigma(\lambda_i)$ are estimates supplied to the software. Note that the denominator really contains a subtraction and not an addition as might naively be thought. This also implies that the fitted errors are always smaller than the original errors.

The pulls are a very sensitive measure of the goodness of the fit. If the mean of the pull distribution is not zero, then the data is biased for some reason. This bias could be background, or it could be a detector bias. For example the z-position of the neutral vertex shifts the distribution of the pull of θ_{PED}. If the width is not one, then usually the initial errors are not as good as they could have been. It is usual practice to globally scale the measured initial errors by a factor of order unity in order to force the pull distributions to have a width of one.

10.1.5 Conversion of Rectangular to Helix Parameters

omitted due to lack of time.

See HelixParam.cc

10.1.6 PED parameters to Rectangular

Because the internal calculations are done in rectangular coordinate, the measured parameters of the PEDs must be converted from spherical coordinates. The conversion of the error matrices is a little more work. To calculate the pulls in the original basis, the internal values need to be converted back too.

$$
\begin{aligned}
P_x &= (\sqrt{E})^2 \cos\phi \sin\theta && (10.3)\\
P_y &= (\sqrt{E})^2 \sin\phi \sin\theta && (10.4)\\
P_z &= (\sqrt{E})^2 \cos\theta && (10.5)\\
P &= \sqrt{P_x^2 | P_y^2 + P_z^2} && (10.6)\\
& && (10.7)
\end{aligned}
$$

$$
\begin{aligned}
\phi &= \texttt{ATAN2}(P_y, P_x) && (10.8)\\
\theta &= \arccos(P_z/P) && (10.9)\\
\sqrt{E} &= \sqrt{P} && (10.10)
\end{aligned}
$$

$$
\begin{aligned}
\frac{\partial P_x}{\partial \phi} &= (\sqrt{E})^2(-\sin\phi)\sin\theta && (10.11)\\
\frac{\partial P_y}{\partial \phi} &= (\sqrt{E})^2(\cos\phi)\sin\theta && (10.12)\\
\frac{\partial P_z}{\partial \phi} &= 0 && (10.13)\\
\frac{\partial P_x}{\partial \theta} &= (\sqrt{E})^2(\cos\phi)\cos\theta && (10.14)\\
\frac{\partial P_y}{\partial \theta} &= (\sqrt{E})^2(\sin\phi)\cos\theta && (10.15)\\
\frac{\partial P_z}{\partial \theta} &= (\sqrt{E})^2(-\sin\theta) && (10.16)\\
\frac{\partial P_x}{\partial \sqrt{e}} &= 2(\sqrt{E})(\cos\phi)\sin\theta && (10.17)\\
\frac{\partial P_y}{\partial \sqrt{e}} &= 2(\sqrt{E})(\sin\phi)\sin\theta && (10.18)\\
\frac{\partial P_z}{\partial \sqrt{e}} &= 2(\sqrt{E})\cos\theta && (10.19)
\end{aligned}
$$

$$
\begin{aligned}
\frac{\partial \phi}{\partial P_x} &= -P_y/P_T^2 && (10.20)\\
\frac{\partial \phi}{\partial P_y} &= P_x/P_T^2 && (10.21)\\
\frac{\partial \phi}{\partial P_z} &= 0 && (10.22)
\end{aligned}
$$

$$\frac{\partial\theta}{\partial P_x} = \frac{P_x P_z}{P_T P^2} \tag{10.23}$$

$$\frac{\partial\theta}{\partial P_y} = \frac{P_y P_z}{P_T P^2} \tag{10.24}$$

$$\frac{\partial\theta}{\partial P_z} = \frac{-P_T}{P^2} \tag{10.25}$$

$$\frac{\partial\sqrt{E}}{\partial P_x} = \frac{P_x}{2P^{3/2}} \tag{10.26}$$

$$\frac{\partial\sqrt{E}}{\partial P_y} = \frac{P_y}{2P^{3/2}} \tag{10.27}$$

$$\frac{\partial\sqrt{E}}{\partial P_z} = \frac{P_z}{2P^{3/2}} \tag{10.28}$$

10.2 Polarized Decay

In general, a polarized spin particle will not decay isotropically. For spin-1 particles decaying into spin-0 particles, the following radiation patterns are observed:

$$|1 \pm 1\rangle = \tfrac{1}{2}(1 + \cos^2\theta) \tag{10.29}$$

$$|10\rangle = \sin^2\theta \tag{10.30}$$

Annihilations of $p\overline{p}$ occur primarily in low angular momentum states, written in $^{2s+1}L_J^{(PC)}$ format:

$$^1S_0^{(-+)}, ^3S_1^{(--)}, ^1P_1^{(+-)}, ^3P_0^{(++)}, ^3P_1^{(++)}, ^3P_2^{(++)}$$

When decaying into vector + pseudoscalar, i.e. $p\overline{p}\to\omega\eta$ or $p\overline{p}\to\omega\pi^0$, only $^3S_1$ and $^1P_1$ states are allowed by C-parity.

In the frame of the vector particle, the orbital angular momentum quantized along the motion axis of the vector particle always has $m_L = 0$, because $\vec{L}\cdot\vec{P} = (\vec{R}\times\vec{P})\cdot\vec{P} = 0$.

Annihilation	Vector+Pseudoscalar System		
	J^{PC}	Orbital Ang. Mom. $\|Lm\rangle$	Spin Ang. Mom. (S)
$^1P_1$	1^{+-}	$\|00\rangle$	1
$^3S_1$	1^{--}	$\|10\rangle$	1
$^1P_1$	1^{+-}	$\|20\rangle$	1

We now examine the Clebsch-Gordan coefficients to couple $L + S = J$, where $J = 1$ in all cases.

$\langle LSm_Lm_s\|Jm_J\rangle$	value
$\langle 01\ 0\ 0\|1\ 0\rangle$	1
$\langle 11\ 0\ +1\|1\ +1\rangle$	$-\sqrt{1/2}$
$\langle 11\ 0\ 0\|1\ 0\rangle$	0
$\langle 11\ 0\ -1\|1\ -1\rangle$	$\sqrt{1/2}$
$\langle 21\ 0\ +1\|1\ +1\rangle$	$\sqrt{1/10}$
$\langle 21\ 0\ 0\|1\ 0\rangle$	$-\sqrt{2/5}$
$\langle 21\ 0\ -1\|1\ -1\rangle$	$\sqrt{1/10}$

Finally, the radiation distributions are as follows, obtained by multiplying the pure polarization distributions by the C-G coefficients squared and summing, then renormalizing to the form $1 + b\cos^2\theta$.

$p\overline{p}$	V+P System	Radiation Distribution
$^1P_1$	$L = 0$	1 (isotropic)
$^3S_1$	$L = 1$	$1 + \cos^2\theta$
$^1P_1$	$L = 2$	$1 - 3/5\cos^2\theta$

For antiproton annihilations in liquid hydrogen, the ratio of P to S wave annihilation has been measured in other experiments with values ranging from 0 to 10%, while in gaseous hydrogen annihilation it is closer to 50%. In this measurement of $\omega\to\pi^0\gamma$ decays, the decay angle distribution is consistent with mostly S-wave annihilation.

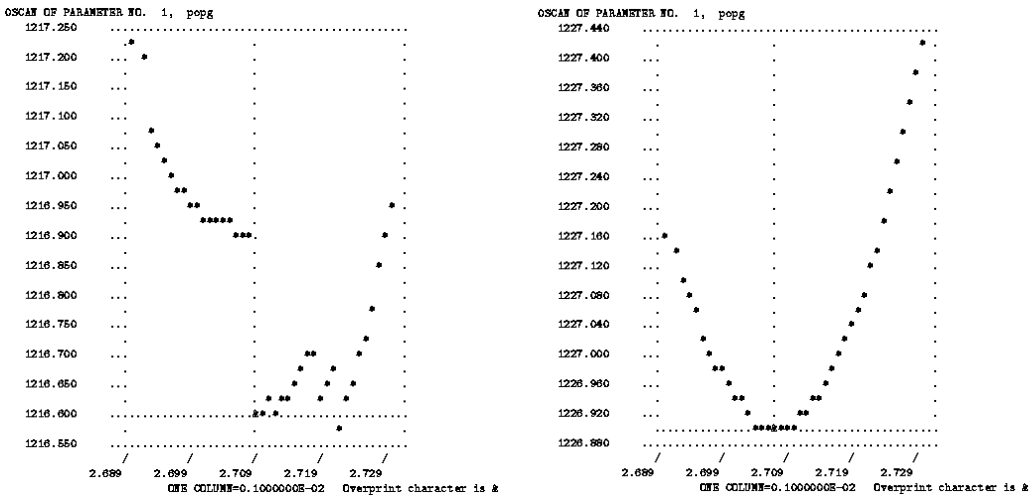

(A) (B)

Figure 10.1: The dependence of the negative log-likelihood ($\sim \chi^2$) on a fit parameter around the fit minimum for different convergence thresholds. (A) $\epsilon = 0.1$. Note the severe discontinuities which fool the minimization routine into local minima. (B) $\epsilon = 0.002$

10.3 Fitting Algorithm

The problem of fitting many Monte Carlo distributions (with limited statistics) to the data (again with limited statistics) is difficult to solve. The standard log-likelihood method for Poisson data is to minimize the function

$$\chi^2 = \sum_i \left[2(N_i^{th} - N_i^{\text{observed}}) + 2N_i^{\text{observed}} \ln(N_i^{\text{observed}}/N_i^{\text{theory}}) \right]$$

If N_i^{observed}=0, then the second term is dropped. (PDG 1996,p. 1276).

However, this method breaks down when N_i^{theory} is zero and $N_i^{\text{observed}} \neq 0$. This can happen if there are statistical errors in the theory, such as is the case for Monte Carlo simulations of the theory. The obvious solution is to generate enough Monte Carlo so that every bin has at least a few events. However, this is nearly impossible for weak feed through channels.

Simply ignoring problem bins is not valid. Consider a two bin problem, with the true $N_i^{\text{theory}} = 0.5$, but with $N_i^{\text{theory}}{}_1 = 0$ and $N_i^{\text{theory}}{}_2 = 1$ as calculated by Monte Carlo. If we ignore the first bin, the average of remaining bins is now 1.0, rather than 0.5, which is clearly wrong and the result of a fit will be biased. The old fits of the ω decay problem were biased in this way, where the 2-D fit (with low statistics in the bins) differed from the 1-D fit (with high statistics) by 50%.

The key to the problem is that the true theoretical value is unknown, and this value should be another parameter in the fit, constrained by the data and the Monte Carlo.

The problem has been addressed by Eberhard *et al.* [28]. In their algorithm, they attempt to maximize the log-likelihood,

$$L = \sum_j \left[n_j \ln \lambda_j - \lambda_j + \sum_i (m_{ij} \ln f_{ij} - f_{ij}) \right],$$

where the j's run over bins, the i's run over the MC data sets, n is the number of data events, m is the number of MC events, f is the *expected* number of MC events, and λ is the expected number of data events, defined as

$$\lambda_j = \sum_i a_i f_{ij}$$

where a_i is the strength of the i'th MC channel.

Because all of the α_i and f_{ij} are unknowns, this problem becomes intractable as a direct minimization of too many free parameters. However, the next best thing to do solve for the f_{ij} first, and then maximize

with respect to α. The method for solving for the f_{ij} is detailed in reference [28]. The algorithm was strictly followed, with the value of $\epsilon = 0.0002$ used as the convergence criterion when iteratively solving for the f, which is roughly the precision to which the f's are solved. It was found that the value of $\epsilon = 0.1$ is too coarse, and causes aliasing in the total likelihood function, which subsequently causes severe problems in MINUIT because the aliasing causes micro-sized local minima. Values of $\epsilon = 0.01, 0.002$ greatly improve the simple gradient descent fit, but still cause problems with the MINOS calculation of the errors. The chosen value allows a sufficiently smooth likelihood function such that MINOS does not fail.

In some special cases with low statistics, Minuit would sometimes move into unphysical regions of the fit space. In this case, all parameters were then forced to be positive and the fit was repeated. Bounded fits in situations that did not require them show that the systematic problems normally associated with bounded fits were minimal.

Another improvement for the fitting was to introduce variable sized bins, which were smaller near the ω peak and larger in the background region. This increases the events per bin, and also cuts down on CPU time because there are fewer bins.

10.4 DLT

The DLT 0-prong summary tapes were copied from the raw data. Each tape contains nearly one hundred files, where each file is the contents of one IBM tape cartridge (named GHxxxx).

A full list of the contents is available from the author.

```
Listed by LB tape number

label  files Mbyte runs(nfiles:firstGH-lastGH)
-------------------------------------------------------------------------
LB0010  135  19293 may91(39:2998-3042) jun91(47:3408-3606) aug91(49:3906-3956)
LB0011  108  17093 aug91( 9:3957-3996) oct93(45:7021-7607) sep90(54:1730-1916)
LB0012  106  16322 sep90(53:1917-2190) jun94(24:7738-7806) dec89(29:0786-0846)
LB0013  106  16155 jun90(51:1101-1160) nov90(55:2201-2605)
LB0014   83  16112 nov90(83:2606-2774)
LB0015  103  15595 nov90(33:2775-2816) jul90(70:1371-1491)
LB0017  106  15115 jul90(99:1492-1613) dec89( 7:0848-0858)


Listed by Run

run   Mevts  files tape(firstfile:lastfile) ...
-----------------------------------------
dec89  1.0    36   LB0012(77:105) LB0017(99:105)
jun90  1.5    51   LB0013(0:50)
jul90  5.0   169   LB0015(33:102) LB0017(0:98)
sep90  1.3   107   LB0011(54:107) LB0012(0:52)
nov90  5.0   171   LB0013(51:105) LB0014(0:82) LB0015(0:32)
may91  1.6    39   LB0010(0:38)
jun91  1.6    47   LB0010(39:85)
aug91  1.8    58   LB0010(86:134) LB0011(0:8)
oct93  1.9    45   LB0011(9:53)
jun94  1.1    24   LB0012(53:76)
---------------------------------
total 21.8   747   7 DLT's
```

10.5 Normalization for BW applied to Dalitz plot

The normalized Breit-Wigner,

$$BW(m) = \frac{1}{2\pi}\frac{\Gamma}{(m-m_\omega)^2+\Gamma^2/4}$$

satisfies the normalization condition

$$\int_{-\infty}^{\infty} BW(m)dm = 1.$$

Branching ratio measurements are defined for "ideal" mass mesons, meaning that it only holds true for mesons with mass equal to the tabulated mean mass. Using this definition, the width of the ideal meson can be taken to be 0 and the BW resonance curve can be replaced by a delta function.

$$BW(m) \rightarrow \delta(m-m_\omega)$$

However, the delta function is only normalized when integrated in one dimension. We demand that our resonance function be normalized to unity on the Dalitz plot, so that each flat generated Monte Carlo event can be weighted properly. The normalization of the dalitz plot depends on the resonance mass and the mass of the recoiling particle. For example, because there is more phase space in the $\pi^0\rho^0$ dalitz plot than in the $\eta\rho^0$, the bare delta function would not have the same integral over the Dalitz space.

We shall find X such that

$$\frac{1}{X}\int\int_{\text{dalitz}} dm_{12}^2 dm_{13}^2 BW(\sqrt{m_{12}^2}) = 1$$

The value of X will have units of MeV^3. Let

$$BW(\sqrt{m_{12}^2}) \rightarrow \delta(\sqrt{(}m_{12}^2) - m_\omega)$$

then

$$\begin{aligned}
X &= \int\int_{\text{dalitz}} dm_{12}^2 dm_{13}^2 BW(\sqrt{m_{12}^2}) && (10.31)\\
&= \int dm_{12}^2 \delta(\sqrt{(}m_{12}^2) - m_\omega) \int_{min}^{max} dm_{13}^2 && (10.32)\\
&= \int dm_{12}^2 \delta(\sqrt{(}m_{12}^2) - m_\omega) 4\sqrt{(E_1^2-m_1^2)(E_3^2-m_3^2)} && (10.33)\\
&= \int dm_{12}^2 \delta(\sqrt{(}m_{12}^2) - m_\omega) 4\sqrt{(E_1^2-m_1^2)(E_3^2-m_3^2)} && (10.34)\\
X &= (2m_\omega) 4\sqrt{(E_1^2-m_1^2)(E_3^2-m_3^2)} && (10.35)\\
E_1 &= (m_\omega^2 - m_2^2 + m_1^2)/2m_\omega && (10.36)\\
E_3 &= (M^2 - m_\omega^2 + m_2^2)/2m_\omega && (10.37)
\end{aligned}$$

To do a statistical integration that equals the analytic integration, you need to multiply each sample by a weight α, which is the differential area divided by the X normalization

$$\alpha = \frac{dA}{X} = \frac{DalitzArea}{XN}$$

That's it. The numerical values of α (which have units on MeV) for each dalitz plot are given in table 5.1.

Bibliography

[1] P.J. O'Donnel, "Radiative decays of mesons," *Rev. Mod. Phys* **53** (1981) 673.

[2] Crystal Barrel Collaboration, E. Aker, *et al.*, "The Crystal Barrel: Meson Spectroscopy at LEAR with a 4π Neutral and Charged Detector," *Nucl. Instr. & Meth.* **A321** (1992) 69.

[3] Crystal Barrel Collaboration, C. Amsler, *et al.*, "Coupled channel analysis of $p\overline{p}$ annihilation into $\pi^0\pi^0\pi^0$, $\pi^0\eta\eta$, and $\pi^0\pi^0\eta$." *Physics Letters* **B355** (1995) 425.

[4] *Physics Letters* **B311** (1993) 371.

[5] Crystal Barrel Collaboration, C. Amsler, *et al.*, "Antiproton-proton annihilation at rest into $\omega\pi^0\pi^0$," *Physics Letters* **B311** (1993) 362.

[6] R. Brun, *et al.*, Internal Report CERN DD/EE/84-1, CERN, 1987.

[7] F. James, *N-Body Monte-Carlo Event Generator*, Program Library W515, CERN, 1975.

[8] Crystal Barrel Collaboration, C. Amsler, *et al.*, "Antiproton-proton annihilation at rest into two-body final states," *Z.Phys* **C58** (1993) 175.

[9] *Zeit.Phys.* **A351** (1995) 325.

[10] Crystal Barrel Collaboration, C. Amsler, *et al.*, "Study of $p\overline{p}$ annihilation at rest into $\omega\eta\pi^0$," *Physics Letters* **B327** (1994) 425.

[11] R. Bizzari *et al.*, *Nucl. Phys.* **B14** (1969) 169.

[12] C. Amsler and F. Myhrer, "Low Energy Antiproton Physics," *Annu. Rev. Nucl. Part. Sci.* **41** (1991) 235.

[13] Crystal Barrel Collaboration, C. Amsler, *et al.*, "Study of $f_0(1500)$ decays into 4 π^0's in $p\overline{p}$ annihilations into five π^0's at rest" *Physics Letters* **B380** (1996) 453.

[14] Particle Data Group, *Phys. Rev.* **D50** (1994) 1196.

[15] Y.S. Zhong, T.S. Cheng, A.W. Thomas, "The M1 radiative decay of low-lying mesons in the cloudy bag model with centre-of-mass correction," *Nucl. Phys.* **A559** (1993) 579.

[16] M. Benayoun, Ph. Leruste, L. Montanet, J.-L. Narjoux, "Meson Radiative Decays and Anomaly Physics, a Test of QCD," LPC-94-31, June 30 ,1994.

[17] N. Barik, P.C. Dash, "Radiative decay of light and heavy mesons," *Phys. Rev.* **D49** (1994) 299.

[18] P. Singer, G.A. Miller, *Phys. Rev.* **D39** (1989) 825.

[19] A. Bramon, A. Grau, G. Pancheri, "Radiative vector-meson decays in SU(3) broken effective chiral Lagrangians," *Phys. Lett.* **B344** (1995) 240.

[20] S. Dolinsky, *et al.*, "Radiative decays of ρ^0 and ω mesons," *Z.Phys* **C42** (1989) 511.

[21] IHEP-PPLA-LANL-INRU Collaboration D. Alde, *et al.*, *Phys. At. Nucl.* **56** (9), September 1993, 1229. *Z. Phys.* **C61** (1994) 35.

[22] H.B. O Connell, B.C. Pearce, A.W. Thomas, A.G. Williams, *Physics Letters* **B354** (1995) 14-19.

[23] H.B. O Connell, B.C. Pearce, A.W. Thomas, A.G. Williams, hep-ph/9501251.

[24] The Crystal Barrel Collaboration (A. Abele et al.), ρ^0-ω Interference in Antiproton Proton Annihilation at rest into $\pi^+\pi^-\eta$, *Phys. Lett.* **B411** (1997) 354.

[25] F. James and M. Roos, CERN-DD Long write-up D506, CERN, 1987.

[26] *Physics Letters* **B322** (1994) 431.

[27] Claudio Pietra, "Rare radiative ω decays", Crystal Barrel Technical Report, August 1996, and The Crystal Barrel Collaboration (A. Abele et al.), Measurement of the $\omega \to \eta\gamma$ decay..., *Phys. Lett.* **B411** (1997) 36.

[28] P. Eberhard, G. Lynch, D. Lambert, "Fits of Monte Carlo distributions to data", Nucl. Inst. Meth. **A326** (1993) 574-580.

[29] P. Weidenauer et al., Z. Phys **C59** (1993) 387.

[30] N.N. Achasov and G.N. Shestakov, Sov. J. Part. Nucl **9** (1978) 19.

[31] R. Bizzari, *et al*, Phys. Rev. Lett **25** (1970) 1385.

[32] M. Lakata, Crystal Barrel Internal note CB321